MASTER

Measurement and statistical modelling of indoor radio channels in the mm-wave frequency band

Wagemans, A.G.

Award date:
1992

FACULTY OF ELECTRICAL ENGINEERING
EINDHOVEN UNIVERSITY OF TECHNOLOGY
Telecommunications Division

Measurement and Statistical Modelling of Indoor Radio Channels in the mm-Wave Frequency Band

PART 1

By: A.G. Wagemans

Graduation Thesis

Period	:	May 1991 - February 1992
Mentors	:	Ir. P.F.M. Smulders
		Dr. Ir. M.H.A.J. Herben
Supervisor	:	Prof. Dr. Ir. G. Brussaard

Preface

My graduation period at the Telecommunication Division has been an enjoyable period.
I would like to thank Peter Smulders and Matt Herben for their support and guidance during my graduation period. I would especially like to thank Peter for his assistance in the rather strenuous task of gathering the experimental data.
A special word of thanks to the people of the Theoretical Division for making time available for our antenna measurements in their compact antenna test range. I would like to thank Tjeu Knoben in particular, for his assistance in performing the antenna radiation pattern measurements.

This work could not have been done without the financial support of the STW (Stichting Techniek en Wetenschappen) which made it possible for the Telecommunications Division to purchase the expensive measurement equipment. STW has made it possible for us to work with state-of-the-art measurement equipment, which has been a very instructive experience.

Summary

Research into indoor radio communications has intensified greatly over the last few years. Indoor radio communication systems in future office environments will offer users a larger mobility than cable-based systems. Spectral space necessary for future Broadband-ISDN systems is only available at mm-wave frequencies. An additional advantage of these frequencies is that they are strongly attenuated by building materials and the atmosphere, which makes frequency reuse possible over very short distances. A disadvantage of indoor radio channels is that their multipath nature limits the achievable bitrate of a digital communication system. Indoor radio channels at mm-wave frequencies are characterized in this thesis. The objective of this thesis is to find a statistical description of the ray arrival process. The statistical model can be used for feasibility studies on high speed digital indoor radio communication systems.

Eight different rooms at the Eindhoven University of Technology were subjected to propagation experiments. Frequency domain measurements were performed in a 2 Ghz bandwidth, using a vector network analyzer. An unprecedented 1 ns measurement resolution was achieved. Different setups and frequencies were evaluated. A total of some 300 measurements were performed in 14 measurement series. Two types of antennas were used: omnidirectional biconical horns and a directional circular horn. Average channel behaviour is very different in the rooms, due to differences in room-size and reflection properties of walls. Channel behaviour is very similar at 41-43 GHz and 57-59 GHz. A very uniform spatial channel behaviour, and least LOS dependency, in a single room is achieved with an omnidirectional remote at table-height and a central omnidirectional base station near the ceiling of the room. This is caused by antenna gain compensation of the free-space losses at larger separation distances. Time delay spread values ranged from 15 to 100 ns. Evaluation of the measured time delay spread values shows that symbolrates up to 2 Ms/s would require no channel equalization. For larger symbol rates some form of Decision Feedback Equalization will have to be used.

Path statistics are very similar in all rooms. The indoor multipath channels are modelled as discrete uncorrelated rays. Ray amplitudes are found to be Rayleigh distributed, and decay exponentially with time. The ray arrival process is modelled as a single rate Poisson process. Because the mean of the interarrival times are comparable to the measurement resolution it seems that the model converges towards a continuous Rayleigh model.

Comparison of measurements to simulations which use Geometrical Optics shows that this deterministic model could describe the channels very well. The software limits the number of reflections to 4. This is insufficient for small rooms with highly reflective walls. Rays which reflect up to 10 times may have to be incorporated in the model. The Geometrical Optics model can only be used for accurate prediction of channel behaviour if more data on scattering parameters of walls and objects at mm-wave frequencies becomes available. Extensive measurements of these parameters would therefore be recommendable.

Contents

PART 1

PART 2

1 Introduction

At the Telecommunications Division of the Eindhoven University of Technology (EUT), research is being conducted in the field of indoor radio communications. The work is carried out in cooperation with different institutes brought together by the Euro-COST 231 project group. This group studies the evolution of land mobile radio (including personal) communications. Euro-COST is an abbreviation for European Co-operation in the field Of Scientific and Technical research.

Research on indoor radio communication has intensified greatly over the last few years. A lot of research effort is spent studying frequencies of 1-2.5 GHz, because these bands are allocated to portable radio systems. In Eindhoven a feasibility study on broadband indoor radio networks is being carried out. The broadband nature is emphasized because it is expected that by 1995 the Broadband ISDN (Broadband Integrated Services Digital Network) will be introduced. The objective of broadband ISDN is to offer a maximum user capacity of approximately 150 Mb/s, with a total network capacity of over 600 MB/s. If an indoor radio network is to be incorporated in B-ISDN, it must also offer the information capacity mentioned above. Conventional frequency bands cannot be used, simply because there is not enough spectral space available for such high data rates. The necessary spectral space is, however, available at frequencies above 30 GHz. This makes mm-wave frequencies a very interesting subject of study. Measurements of indoor radio channels at these frequencies have only been reported sporadically. The mm-wave frequencies are strongly attenuated by building materials. Absorbtion due to water vapour and oxygen is considerable for mm-wave frequencies. Reliable communication is therefore limited to one room only. This makes frequency reuse possible over relatively short distances, even within one building.

The indoor radio sytem proposed is a wireless LAN in which all remotes, which all communicate with one base station, do not move during operation.
Using a radio network for indoor communications in, for example, offices, hospitals and factories, has several advantages above conventional cable-based systems. First of all, users are not tied to particular locations in a room, equipment can be relocated at will, thus greater mobility is offered. Secondly, expenses to re-wire a building (after renovations for instance) are avoided.

In order to attain insight in the behaviour of an indoor radio channels at mm-wave frequencies, extensive wide band frequency domain measurements of the propagation characteristics in several rooms in 3 different buildings on the EUT campus were undertaken. The main objective of the indoor radiowave propagation measurements is to determine the radio coverage and data rate limitations in various rooms. The radio coverage is related to the power-distance relation in a room and the data rate is limited by the frequency selective fading (multipath) characteristics of the channel. In the time domain the data rate limitations are studied by examining the statistics of the time delay spread.

In chapter 2 the parameters which characterize an indoor radio channel will be presented. A computer simulation program has been written by a graduate student of the EUT [1]. A description of this software is given in chapter 3. Chapter 4 describes the equipment used for conducting frequency domain measurements at mm-wave frequencies. The transmitting and receiving antennas used have a considerable influence on the radio propagation in indoor environments. The geometry of the antennas is described in chapter 5. A detailed description of the layout of the 8 measured environments is given in chapter 6. In chapter 7 the measured propagation characteristics of the different rooms are presented. The influence that system setup and measurement frequency has on the radio channels is studied in this chapter. Difference in room behaviour is also studied here. A statistical propagation model will be derived from measurement results in chapter 8. This model can be used for evaluating the performance (outage probability) of an indoor radio system which uses equalization techniques. In chapter 9 measurements will be compared with simulations.

This report is split in two separate books. This part, part 1, contains the thesis text. In part 2 the figures which are described in this text are presented. This should make the reading of the report less cumbersome.

2 Characterisation of the Indoor Radio Channel

A project group of COST 231 has defined a number of room configurations which should be subject of further studies. The dimensions of these rooms are 60 m* 40 m*4 m (large office), 75 m*4 m*3 m (corridor) and 10 m*10 m*3 m (small office).
Within a room, remote stations communicate via a base station. The antennas of the remotes are located at table-height. The base station antenna is located at the centre of the room, a few decimeters below the ceiling. The antennas which we will use for conducting measurements exhibit omnidirectional radiation patterns in the horizontal plane.

If both transmitting and receiving antennas are located in the same room, electromagnetic power will not only travel via a direct path from transmitter to receiver, but also via indirect paths due to reflections of the EM waves against walls and objects within the room. The indoor radio channel is therefore a multipath channel. Multipath propagation causes a single transmitted pulse to be received as a train of successive pulses in the time domain. This time domain spreading of the impulse response can degrade the performance of the channel seriously, because it increases the Inter Symbol Interference (ISI). In the next few sections the parameters which describe the multipath propagation are defined.

2.1 The Channel Impulse Response

The indoor radio channel is actually a bandpass filter around a central frequency f_c (in our case 40 or 60 GHz), with a frequency response *V(f)*. The channel is defined by its equivalent complex lowpass frequency response *H(f)* according to

$$V(f) = H(f-f_c)+H^*(-f-f_c)\ , \tag{1}$$

where

$$H(f-f_c) = \begin{cases} V(f) & f>0 \\ 0 & f<0 \end{cases}, \tag{2}$$

and

$$H^*(-f-f_c) = \begin{cases} 0 & f>0 \\ V(f) & f<0 \end{cases}. \tag{3}$$

Inverse Fourier Transform of (1) yields

$$v(t)=2Re(\ h(t)e^{j\omega_c t}\ )\ , \tag{4}$$

in which *h(t)* denotes the Inverse Fourier Transform of *H(f)* and is called the

equivalent complex lowpass impulse response. This definition will be used throughout this report.

Suppose that a carrier of frequency f_c is transmitted. Because of the multipath nature of the channel the transmitted wave is received as a number of attenuated and delayed waves. The transmitted wave *s(t)* can be formulated as

$$s(t) = Re\ (u(t)e^{j\omega_c t})\ . \tag{5}$$

In (5) *u(t)* is a lowpass signal. The received waveform will be

$$x(t) = \sum_n \alpha_n(t)s(t-\tau_n)\ , \tag{6}$$

where α_n and τ_n are the attenuation factor and propagation delay of path n, respectively. The attenuation factor α_n not only contains the free space loss of path n, but also a number of complex reflection coefficients. Both these parameters will be time-variant, due to motions of people and/or objects in the room. However, since motion speed is low, the channel response will not noticeably change over many bitperiods. The channel is therefore assumed to be quasi-stationary. Naturally α_n and τ_n will also depend on the positioning of transmitter and receiver in the room. Substitution of (5) into (6) yields

$$x(t) = Re\left(\sum_n \alpha_n e^{-j\omega_c\tau_n}u(t-\tau_n)e^{j\omega_c t}\right)\ . \tag{7}$$

If (7) is compared with (5), it is clear that the received lowpass signal must be

$$r(t) = \sum_n \alpha_n e^{-j\omega_c\tau_n}u(t-\tau_n)\ . \tag{8}$$

From (8) it is evident that the equivalent complex lowpass impulse response *h(t)* is

$$h(t) = \sum_n \alpha_n e^{-j\omega_c\tau_n}\delta(t-\tau_n)\ . \tag{9}$$

This is proved by convoluting *h(t)* and *u(t)*.

$$\begin{aligned} r(t) &= \int_{-\infty}^{\infty} h(t-\xi)u(\xi)d\xi \\ &= \sum_n \left[\int_{-\infty}^{\infty} \alpha_n e^{-j\omega_c\tau_n}\delta(t-\tau_n-\xi)u(\xi)d\xi\right] \\ &= \sum_n \alpha_n e^{-j\omega_c\tau_n}u(t-\tau_n)\ . \end{aligned} \tag{10}$$

Suppose an unmodulated wave is transmitted, i.e. $u(t) = 1$ for all t. In this case *r(t)* is the sum of a number of phasors with phase $\theta_n = -\omega_c\tau_n$ and amplitude α_n. The θ_n's are uniformly distributed over $[0,2\pi]$, because even a small change in the length of path n can cause a great change of the corresponding phase, while the amplitude is hardly affected. Multipath fading is a result of constructive and destructive

addition of two or more waves.

2.2 *The Power Delay Profile*

It has been shown in the previous section that in a multipath channel a single transmitted pulse is received as a train of pulses due to echoes. The total power received at a particular time t, originates from all delayed pulses with τ_n approximately equal to t. The total received power as a function of time is called the power delay profile. It is defined as [14]

$$p(t) \triangleq |h(t)|^2 . \tag{11}$$

The power profile is often measured [2,3] by sending an RF pulse with a width of say 10 ns and a cosine shaped amplitude. Envelope detection is carried out at the receiving end. If pulses do not overlap at the receiver, the received power is

$$p(t) = \sum_n \alpha_n^2 u^2(t-\tau_n) . \tag{12}$$

In equation (12) $u(t)$ is the baseband pulse shape and α_n^2 is called the power gain of path n. In case of overlapping pulses the mathematical expectation of the power delay profile yields the same result [5], because the phases θ_n are assumed to be uniformly distributed over $[0,2\pi]$. A disadvantage of using RF pulses is that the resolution of the measurements is limited by the pulse width. Narrow pulses are difficult to generate, especially at mm-wave frequencies. In our case however, both phase and amplitude of the frequency domain channel response will be measured.

Using Inverse Fast Fourier Transform (IFFT), the actual $h(t)$ can be calculated and with it the power delay profile. A disadvantage is that the measured impulse response is sampled at regular intervals. In frequency domain measurements, the time domain resolution is determined by the bandwidth of the measurements (more bandwidth gives a better resolution). This will be discussed further in chapter 4. Further drawbacks of frequency domain measurements are that a stationary channel is required during measurements and subsequently no doppler effects due to channel movements can be investigated.

2.3 *Average Time Delay and Time Delay Spread*

From the power delay profile as defined in paragraph 2.2, two important propagation parameters which characterize the indoor radio channel can be derived. The first parameter is the average time delay $\bar{\tau}$. It is a measure of the excess delay between transmitted pulse and the mean of multipath arrival times. This parameter is called the first moment of the received power delay profile and is defined as

$$\bar{\tau} \triangleq \frac{\sum_n \alpha_n^2 \tau_n}{\sum_n \alpha_n^2} \,. \tag{13}$$

The denominator of equation (13) is called the total power gain G, so

$$G \triangleq \sum_n \alpha_n^2 \,. \tag{14}$$

The total power gain G can be used for estimating the signal-to-noise ratio in an indoor radio communication system. It is also important for determining the radio coverage, that is signal level, throughout a particular room.
The second parameter is the average time delay spread which is defined as

$$\sigma \triangleq \sqrt{(\bar{\tau}^2) - (\bar{\tau})^2} \,, \tag{15}$$

where

$$\overline{\tau^p} = \frac{\sum_n \alpha_n^2 \tau_n^p}{\sum_n \alpha_n^2} \,. \tag{16}$$

For continuous profiles the summations over n change into integral expressions. The time delay spread is also known as the second normalized moment of the delay profile.

Why are these parameters so important?

It is well known that there is an irreducible error floor for large signal to noise ratios due to delay spread. When the delay spread is small compared to the symbol period this error floor is almost independent of the delay profile shape and depends only on the delay spread, which determines the Inter Symbol Interference.
It has been shown [16] that the time delay spread is of no importance if $\sigma/T_s < 0.2$, where $1/T_s$ is the symbol rate, but it has a significant influence for $\sigma/T_s > 0.3$. The upper limit of the symbol rate becomes

$$1/T_{s,\max} = 0.2/\sigma \,. \tag{17}$$

If higher bitrates with acceptable bit-error rates are desired, some form of channel equalization, like decision feedback equalization, must be applied. The average time delay does not impose an upper limit on the bitrate, because in practice a receiver will adjust its timing instant to the average time delay. The average time delay is only used for calculating the delay spread. Knowledge of the delay spread statistics is important for designing (number of taps) a decision feedback equalizer.

2.4 Error Considerations on Propagation Parameters

The propagation parameters defined in the previous section are derived from the power delay profile. The power gains of individual paths will decay, according to Valenzuela [5], exponentially with time, for paths with longer delays will have suffered, generally, a larger number of reflections. Time and distance are coupled through the velocity of light: 1 ns delay corresponds to 30 cm travelled distance. On average a ray suffers an attenuation which in decibels is proportional with time, so an exponential decay is expected if only losses due to reflections are considered. The path gains also decrease with time due to free-space loss and losses induced by the propagation medium.

Delay parameters are calculated using the total power gain G. In practice, however, G cannot be measured exactly, because exact measurement would imply measuring over an infinite time span. In addition to this, received power which does not exceed the noise floor of the receiver is masked, so the tail of the profile cannot be measured. Let us assume that we have a continuous profile $p(t) = A\exp(-\lambda t \ln(a))$ (exponential decay) and that signal power for $t > \nu$ is masked by noise. This is depicted in figure 1. Since $p(t)$ is a deterministic function, formulas for the absolute and relative errors in G, $\bar{\tau}$ and σ are easily calculated.

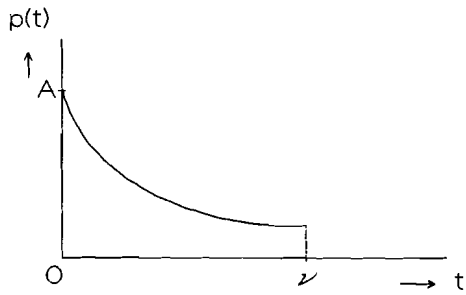

Figure 1: Modelling the Power Profile

The error made is the part of the profile for $t > \nu$ which is discarded in practical calculations. The absolute error between theoretical and practical calculation of G for example, is the integral of $p(t)$ from $t = \nu$ to infinity. Absolute errors for the average time delay and time delay spread can be defined in exactly the same manner. This results in the following relative errors:
Relative error in G:

$$\frac{\Delta G}{G} = a^{-\lambda\nu}.100\% \ . \tag{18}$$

Relative error in $\bar{\tau}$:

$$\frac{\Delta \bar{\tau}}{\bar{\tau}} = a^{-\lambda\nu}.(2+\lambda\nu\ln(a)).100\% \ . \tag{19}$$

Relative error in σ:

$$\frac{\Delta\sigma}{\sigma} = a^{-\lambda\nu}.\left(4 + 2\lambda\nu\ln(a) + \frac{1}{2}(\lambda\nu\ln(a))^2 \right).100\% \ . \qquad (20)$$

Suppose the profile can be measured with a 40 dB dynamic range and that $p(0)$ = 1 and $p(t=250\ ns)$ = 10^{-4} ($\lambda ln(a)$ = 4.10^6, realistic value for a large room). Equations (18)-(20) yield 0.01%, 0.11% and 0.64% respectively for $a = e$. These errors are small. They suggest that the tail of the power profile can simply be discarded in this case. Formulas (18)-(20) are useful for checking errors in case the profiles decay with a larger or smaller λ.

2.5 The Power Decay Rate

The total received multipath power gain P_r is inversely proportional to d^m, where d denotes the distance between transmitter and receiver and m denotes the power-distance law exponent. In a free space situation m will be equal to 2 [9]:

$$P_r = P_t \cdot G_t \cdot G_r \cdot \left[\frac{\lambda}{4\pi d} \right]^2 \qquad (21)$$

In equation (21) P_r and P_t are the received and transmitted power respectively, G_r and G_t denote the receive and transmit antenna gain. In equation (21) the antenna gains have fixed values because only one propagation path is considered. This is not true for indoor environments, were m is not only determined by the separation distance d, but also by the antenna elevation gains. This will be discussed in section 7.2. It should be noted that (21) is actually only valid for the narrowband case. For indoor radio channels the decay of the total multipath power gain G with increasing separation distance is also defined through a decay exponent m. The parameter m can be used to calculate the transmitted power level needed for a good signal coverage in the whole room.

For an indoor radio channel m is expected to be less than 2 [2], because many reflected EM waves add to the total power at the receiver. Each EM wave (path) however must obey the inverse square power-distance law if no reflections are considered. Larger values of m than 2, however, have also been reported [3,4,5]. The measurement frequencies were much lower in these references (around 1 GHz) and decay exponents were sometimes measured over several rooms.

In chapter 2 a brief summary of the propagation parameters of a multipath channel has been given. In the next chapter the simulation programme [1] for the indoor radio channel is discussed.

3 Simulation of the Indoor Radio Channel

The software [1] which will be used for simulations is based on the theory of Geometrical Optics (GO), i.e. it assumes that EM waves in the frequency band under consideration (mm-waves) behave in the same way as light does after reflection against a surface. The programme traces rays leaving the transmitter and calculates the direction of reflected rays off walls and objects according to Snell's laws of reflection. All reflecting surfaces are modeled to be electromagnetically smooth, this means that rays **only** leave in the direction indicated by Snell and scattering due to surface irregularities is not incorporated in the model. Furthermore only rectangular rooms and objects are considered. Also, the transmittivity of surfaces is not considered, so the program can only be used if the transmitting and receiving antennas are positioned in the same room.

EM fields of reflected waves can be calculated by using the polarization dependent Fresnel reflection coefficients for infinite surfaces. Polarization dependent means that field components parallel and perpendicular to the plane of incidence are reflected differently. If polarization is not under consideration, then the field strength of a reflected ray is weighed by a single real reflection coefficient. The Fresnel reflection coefficients are defined by [9]

$$R_{\perp} = \frac{E_{\perp}^{r}}{E_{\perp}^{i}} = \frac{\cos\theta_i - \sqrt{n^2 - \sin^2\theta_i}}{\cos\theta_i + \sqrt{n^2 - \sin^2\theta_i}} , \tag{22}$$

$$R_{\parallel} = \frac{E_{\parallel}^{r}}{E_{\parallel}^{i}} = \frac{n^2\cos\theta_i - \sqrt{n^2 - \sin^2\theta_i}}{n^2\cos\theta_i + \sqrt{n^2 - \sin^2\theta_i}} \tag{23}$$

with a refractive index which equals

$$n^2 = \epsilon_r - j\sigma/(\omega\epsilon_0) , \tag{24}$$

in which ϵ_r and σ (not to be confused with time delay spread) denote the relative permittivity and conductivity of a medium and ϵ_0 denotes the permittivity of vacuum. Formulas (22) and (23) are valid for non-magnetic media which bound on vacuum. The Fresnel reflection coefficients can be applied for finite surfaces if half of the first Fresnel zone on the reflecting surface is small compared to dimensions of objects within the room, since only this area effectively contributes to the reflection of the wave [9]. The model used is only an approximation of reality, because it is found that the minimal surface size of objects and walls for correct calculation of reflections, should be approximately 2 m*2 m at 60 GHz. This is the size of half of the first Fresnel zone for large incident angles. A small error is made, using (22) and (23) for incident angles larger than 85°, with a lower limit of 2 m*2 m on wall and object surface size. This also means that rays which reflect

close to a corner will not be calculated correctly. The simulation program does not calculate diffracted rays, because calculation of diffraction points is very complex and time consuming. However it is shown [1], that diffracted rays could contribute significantly to the power at the receiver at mm-wave frequencies. Further investigation of this phenomenon may be necessary.

The calculation of a power delay profile is a two-step process.
First of all, the paths of all rays from transmitter to receiver are calculated. Rays which reflect up to four times are included in the simulations. Rays are weighted with the radiation patterns of both receiving and transmitting antennas. Each field component is calculated separately.
The second step towards generating a power delay profile is that a cosine shaped pulse, with a certain width τ_p, is sent along each path. The pulse width τ_p must be entered as a program parameter. The time of arrival of each delayed pulse is calculated from the corresponding path length. If pulses overlap and polarization dependency is being considered, they are added as vectors. A time-shift is performed on the calculated profile so that the time delay of the direct ray is zero.

Results presented in [1] are summarized as follows:

Simulations are compared with measurements [24] conducted at 1.7 GHz on a large laboratory floor. The results show that the simulation, at this frequency, gives a good impression of the overall behaviour of an indoor radio channel, even with the limitations mentioned above. Absence of discontinuities in the measured profiles are attributed to diffracted rays and reflections against objects (which were not modelled) in the room.

The influence of antenna radiation patterns on the power delay profile has also been studied. To this end three types of antennas are defined: isotropically, horizontally and vertically radiating sources. The last two patterns are drawn in figures 2 and 3. A Horizontal and vertical radiation pattern does **not** imply a certain polarization state, but merely indicates the direction in which maximal radiation occurs, relative to the floor of a room. Somewhat confusing is that two different coordinate systems are used for defining directions of rays and radiation patterns. The angle θ in figures 2 and 3 does not correspond to a commonly defined θ in a spherical coordinate system which, incidently, is used for calculating the directions of rays.

Comparison of simulations of a large office, using different antennas and no polarization dependent reflection coefficients, show that a vertical source yields a lowest value for the time delay spread σ and a maximum value for the power decay rate m. Horizontal and isotropic results do not differ much in σ, although m is slightly smaller for horizontal sources. So highest bitrates are achieved with vertical sources and horizontal sources give the best coverage in a room.
The delay spread is affected dramatically if larger values of reflection coefficients are used. If the reflection coefficients R of the walls are varied from 0.01 to 0.4, σ_{max} changes from 1.5 to 57 ns! This is to be expected because reflected rays will

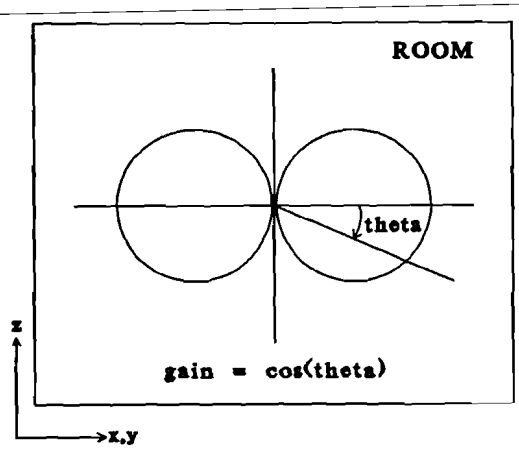

Figure 2: Horizontal Source

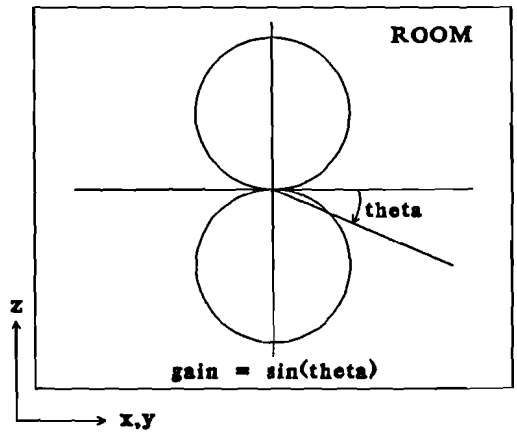

Figure 3: Vertical Source

carry more power if R increases. The power decay rate m is hardly affected by a change of R. A problem may arise if polarization is being considered and metal walls and/or objects are used. With polarization the program expects an ϵ_r for each surface while formulas (22) and (23) are approximated by $\pm$ 1 for metal surfaces. Simulations which include objects in the room configuration show that objects generally cause the delay spread to increase, especially if objects with R = 1 (metal) are used.

Simulations of the same room using polarization dependent reflection coefficients have also been performed. The average co-polarization power delay profile is very similar to the average non-polarization profile. Cross-polarization profiles do not decay very fast. This is because cross-polarization increases with every reflection. The loss of power due to greater distances is partially compensated by this increase. The total power carried by cross-polarization is small compared to co-polarization. For a horizontal source the ratio between co- and cross-polarization power is 20 dB for linear polarization and 12.5 dB for circular polarization.

Validity of the deterministic model described in this chapter must be verified by actual measurements in the mm-wave band. Reflectivity values of walls and objects have a profound influence on the behaviour of the channel. Values used in simulations must be considered carefully. Data on reflectivity values of common building materials in the mm-wave band is unfortunately very scarce, this makes comparison of measurements with simulations difficult.

4 Description of the Measurement Setup

4.1 Measurement Setups Reported in Literature

In the literature several methods of measuring the impulse response of indoor radio channels are reported. These research activities concentrate mainly on frequencies of 1-2.5 GHz, because this band is allocated to portable radio systems. Measurements of indoor radio channels in the mm-wave band have only been reported sporadically [12,13].

The first method, described in [5], uses RF pulse sounding. An RF oscillator was used to generate a 1.5 GHz continuous wave signal, which was then amplitude modulated with a train of 10 ns pulses with a 600 ns repetition period. At the receiving end the transmitted radar-like pulses and their echo's were detected by a square-law envelope detector. A disadvantage of this method is that the phase response of the indoor radio channel cannot be obtained. Also, generating narrow RF pulses becomes increasingly difficult at higher frequencies.

The second method uses correlation properties of pseudo-random noise sequences [6]. A continuous wave signal of 59.9 GHz is bi-phase modulated by a pseudo-random binary sequence and transmitted. The received signal is down-converted and then passed through a quadrature correlator, which provides the lowpass complex impulse response of the channel. An advantage of this system is that phase response is available, but the resolution is limited by the bitrate of the pseudo-random bit sequence. For the measurements reported in [6] the achieved resolution is 10 ns.

The third method uses frequency domain measurements. Methods one and two both directly yield time domain results. If both phase and amplitude of the channel can be measured in the frequency domain, then the time domain response, i.e. impulse response, can be calculated via Inverse Fourier Transform of the frequency data. Measurements conducted in this manner, in a frequency band of 200 MHz around 1 GHz are reported in [7]. This setup uses a network analyzer. An advantage of measuring in the frequency domain is that a signal with a constant envelope is transmitted, as opposed to RF pulse sounding where the ratio of peak to average transmitted power is required to be large. Frequency domain measurements therefore reduce the effects of non-linearities in the receiver. Another important advantage of this method is that the achievable resolution does **not** depend on the width of a pulse or properties of a pseudo-random noise sequence, but **only** on the measurement bandwidth, the type of frequency domain window and the linearity of the sweep. This will be discussed in section 4.4. Drawbacks of this method are that a stationary channel is required during a complete measurement sweep, so no doppler effects can be measured, and that the measured impulse response is sampled at discrete intervals.
In Eindhoven method three was used for mm-wave propagation experiments.

4.2 Measurement setup used in Eindhoven

The system used in Eindhoven for conducting wideband indoor radio propagation measurements is built up around a HP 8510C vector network analyzer. Frequency domain measurements were performed as described in the previous section. A vector network analyzer is capable of measuring complex values, i.e both phase and amplitude, of two-port S parameters. A schematic diagram of the setup is drawn in figure 4.

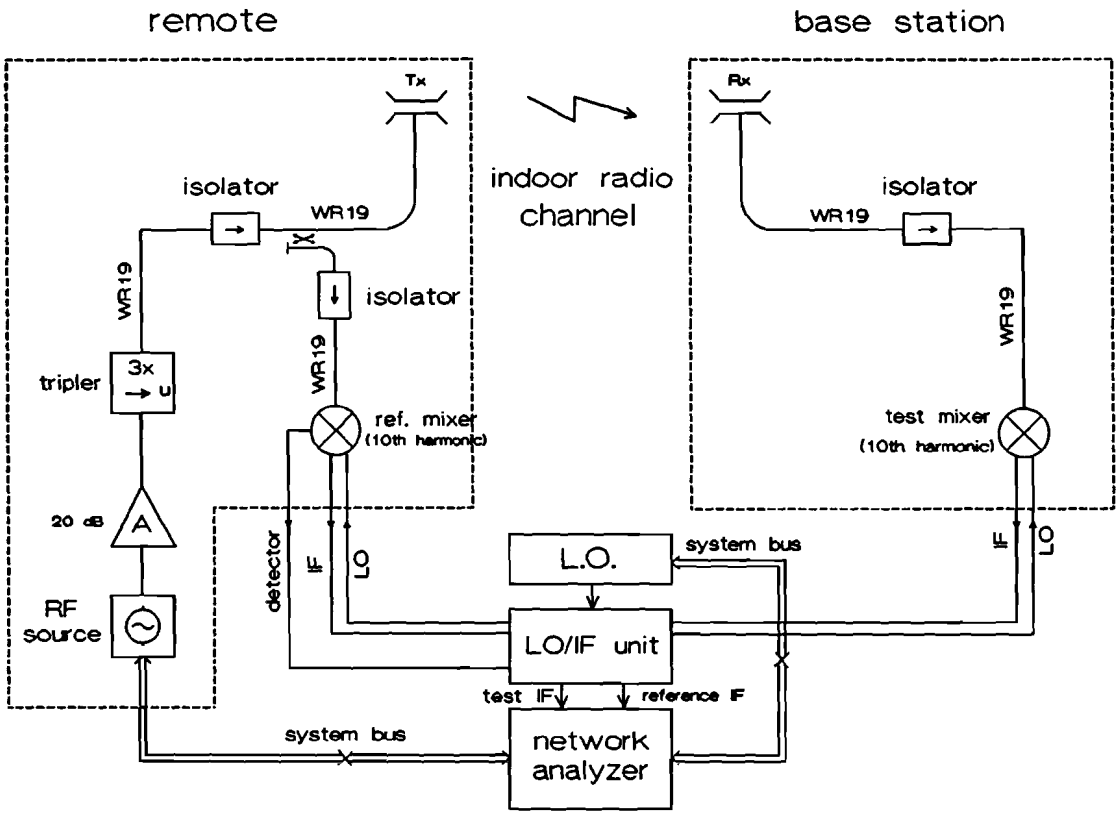

Figure 4: Measurement Equipment

The system is essentially the same as an antenna measuring system. In fact, it was also used for determining the radiation patterns of our antennas. The RF source in figure 4 is only capable of generating sine waves up to a frequency of 50 GHz. To increase the frequency range of the setup the output frequency of the RF source is tripled. This tripled RF signal is then amplified by 20 dB. So for the investigation of the frequency band of 40 to 60 GHz the RF source is used at 13.33 to 20 GHz. The output of the mm-wave amplifier is then applied to a -10 dB directional coupler. The directional coupler separates the incident wave into a test channel wave and a reference channel wave. A reference channel is required for the analyzer to phase lock to the incident wave and thus creating a phase reference. The reference channel output of the directional coupler is connected to a 10th harmonic mixer via a rectangular WR19 waveguide. The test channel output is connected to the transmitting antenna T_x, this is either an omnidirectional biconical

horn or a circular horn antenna. A description of these antennas will be given in chapter 5. The receiving antenna R_x (biconical or circular horn) is also connected to a 10th harmonic mixer. Two different types of antennas were used in order to compare different setup situations in a room, for example a circular horn base station in a corner instead of a central omni, or a circular horn on the remote.

The LO/IF (Local Oscillator/Intermediate Frequency) unit uses one local oscillator signal of 4 to 6 GHz for both 10th harmonic mixers. The mixers are connected to the LO/IF unit by flexible coax cables, this allows the remote and the base station to be moved around in a room. The network analyzer system is extended by the lengths of the cables, i.e. the separation distance between the test ports (mixers) is increased. A small trolley was used as a remote and a camera tripod was used as the base station. The receiving antenna was placed on top of a 1.5 m plastic pipe which was screwed on top of the tripod. The unit controls the LO power which is applied to each mixer by means of a feedback circuit. The harmonic mixers multiply the 10th harmonic of the LO signal with the RF frequency. The LO frequency is offset by 20 MHz, so a 20 MHz IF signal is obtained from both reference and test channel. Both IF signals are fed back to the network analyzer, where the complex ratio of the signals is calculated and displayed as a S_{21} two-port transmission parameter. A photograph of the setup is given in figure 4a.

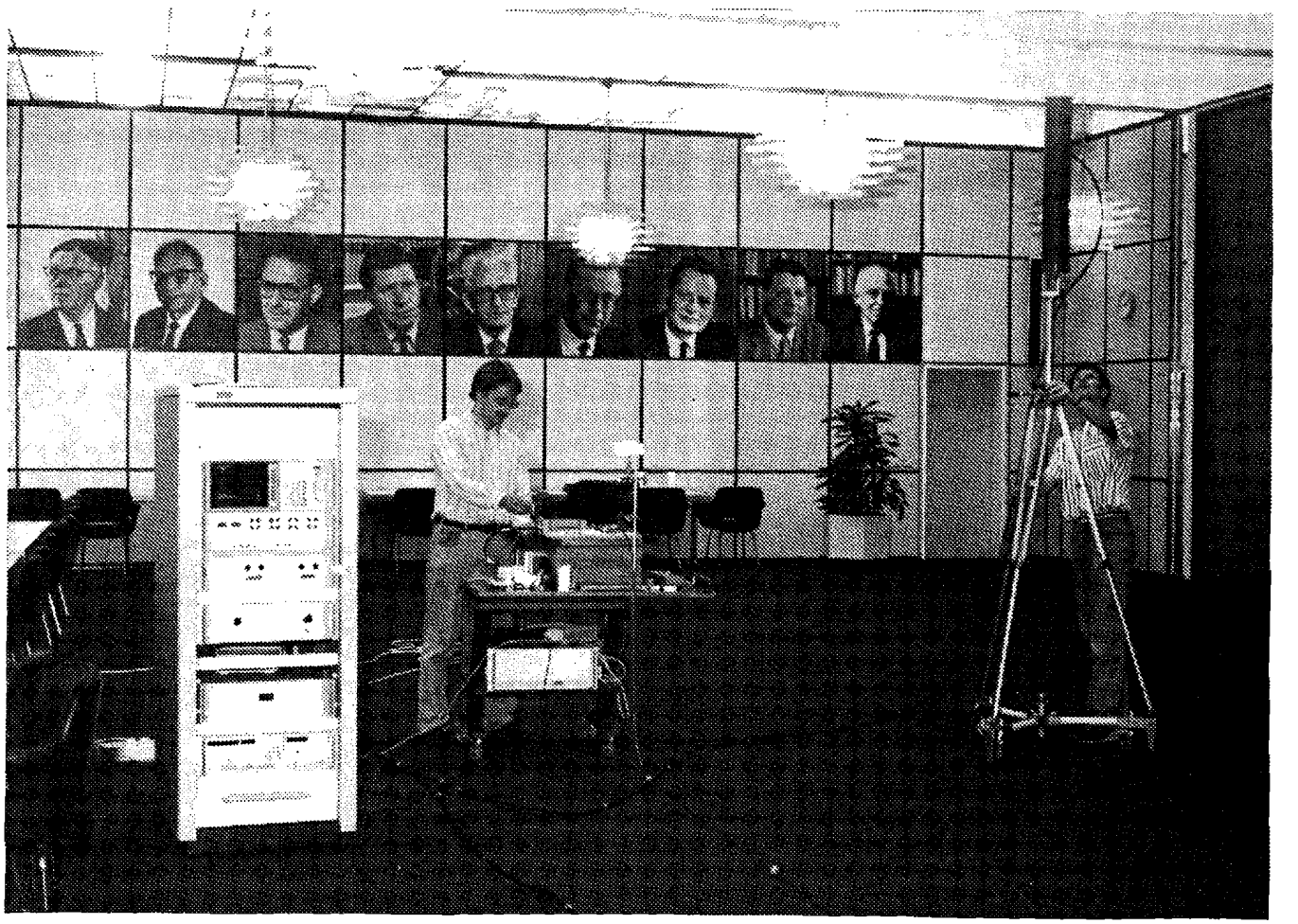

Figure 4a: Photograph of the Measurement Setup

The receiver bandwidth is 10 kHz, which results in a noise floor of approximately -100 dBm. At every measurement frequency the receiver noise floor was reduced even further by averaging the response 128 times. This resulted in a noise floor of -120 dBm, thus increasing the dynamic range by 20 dB. The test channel RF power level at the output of the directional coupler was 0 dBm. The average received power level in the frequency domain was approximately -80 dBm for all measurements, so a 40 dB signal-to-noise ratio was attained.

To protect the sources from being damaged by reflected energy, isolators are added to the system. The isolator at the receiving end ensures that no reflected waves can be retransmitted into the radio channel. The network analyzer controls the RF source by an IEEE bus. Because of this the system had to operate in a stepped instead of a ramped mode. The analyzer waits until the RF source settles, phase locks at a single frequency in the band under consideration and then calculates the response.
In the setup of figure 4 only two separate channels could be connected to the analyzer, so no S_{11} or S_{22} measurements could be performed with this configuration. Reflection measurements require an incident wave and a reflected wave to be combined in one port. This is not possible with the setup drawn in figure 4.
For these two-port measurements the LO/IF unit is superfluous. A HP 85104A mm-wave test set is used instead. The mixers are contained and controlled in the test set ports. An S_{21} measurement can also be performed with this test set. The power available in the HP 85104A test set ports is, however, too small for large separation distances. That is why a LO/IF unit is necessary for indoor radio experiments.

4.3 Calibrating the Network Analyzer

Before any measurement can be done, calibration of the measuring equipment is necessary. A calibration removes systematic errors in the setup by a reference measurement. There is, however, an essential difference in calibrating the system for measuring antenna radiation patterns as compared to indoor propagation experiments. In the first case both antennas are connected and placed in an anechoic chamber. The S_{21} response is measured as a reference and all deviations from an ideal 0 dB and 0 phase frequency response are used for mathematically correcting subsequent measurements of S_{21}. This is done by multiplying the new S_{21} response with the inverse of the complex reference S_{21} at each measurement frequency. The deviations could be caused by residual reflections against walls and objects in the room or by delays and reflections in cables and waveguides.

This method of calibration is not suited for indoor propagation measurements, because **all** relevant information on wall and object reflection will be lost. Instead of this, the calibration is performed by removing both antennas and connecting a piece of waveguide between the two 'test ports', i.e. coupler output and test channel mixer. A 'through' response measurement is then used as a reference. In doing so, systematic errors caused by equipment are mathematically removed. The mis-

matches caused by the antennas are not removed. In time domain this 'through' response shows as a unity pulse at 0 seconds. All power delay profiles are measured relative to this time axis. The significance of this is that measured profiles did not have the line-of-sight (LOS) ray displayed at $t = 0$ seconds, so profiles had to be manually shifted in time on the analyzer display before they could be stored to disk. If the LOS ray could not be clearly discerned in a measured profile, its position was checked by placing a piece of absorber in the LOS path and noting the response change.

4.4 Time Domain Resolution of Measured Delay Profiles

The HP 8510C network analyzer is capable of taking a maximum of 801 frequency samples. This number and the measurement bandwidth determines the aliasing-free range in the time domain, according to

$$Range = \frac{(N-1)}{B}, \tag{25}$$

where N is the number of frequency samples and $B = f_{max} - f_{min}$ is the measurement bandwidth.

Simulations show that an aliasing-free range of 400 ns should be sufficient for measuring profiles in rooms with dimensions up to 40 m* 60 m* 4 m.
A 400 ns excess delay time is equivalent to $400.10^{-9} * 3.10^{8} = 120$ m propagation distance. The free space power loss at this distance (inverse square law) is $20 * \log(120*4*\pi/5.10^{-3}) = 110$ dB. According to formula (25) the maximal bandwidth necessary for a 400 ns aliasing free range with full accuracy is therefore 2 GHz. Discrete Fourier Transform of the equally spaced frequency samples yields 801 complex time domain data points which are also equally spaced at $1/B = 0.5$ ns intervals.

Frequency data can be shaped (multiplied with a function) in order to improve the dynamic range in the time domain. This is called windowing. Because the measurements are bandlimited, no shaping is in fact a rectangular window. It is well known that multiplying frequency data with a window function is a convolution with the Inverse Fourier Transform of the window function in the time domain. For example: if no windowing is used, each time domain pulse is in fact a sinc function $B(\sin(\pi Bt))/(\pi Bt)$. Because the maximum side-lobe level of a sinc is 13 dB below the main lobe level, the time domain dynamic range will be limited to 13 dB in this case. A rectangular window offers, however, highest resolution. The resolution is limited by the width of the main lobe of the inverse window function. Time domain resolution can be defined as the minimal time distance at which two pulses of equal amplitude are still discernable. With a rectangular window this distance is actually slightly more than the time data spacing, that is 0.6 ns in our case.

Generally, dynamic range and resolution are two contradictory parameters. Using a window therefore means finding a compromise between required resolution and dynamic range. Our network analyzer uses a Kaiser window [10] for shaping frequency samples. Its formula and transform are given by

$$W(t) = \frac{1}{\pi I_0(\omega_a \tau)} \cdot \frac{\sin(\omega_a \sqrt{t^2 - \tau^2})}{\sqrt{t^2 - \tau^2}} \quad \leftrightarrow \quad \frac{I_0(\tau \sqrt{\omega_a^2 - \omega^2})}{I_0(\omega_a \tau)}, \tag{26}$$

where $\omega_a \tau = 0, 6, 13$ for a 'minimal', 'normal' and 'maximal' window and $abs(\omega) < \omega_a$. I_0 is the modified Bessel function of the first kind and order zero. A 'minimal' window is simply a rectangular window. In our measurements we used the 'normal' window. This window has a highest side-lobe level of -44 dB and its main lobe is slightly broader than that of a rectangular window. The 'normal' window has all but 0.012 % of its energy in the main lobe. The 'maximum' window has side-lobes smaller than -90 dB. However, because the signal-to-noise ratio in our system is limited to 40 dB, a 'maximum' window would not increase the dynamic range. With a 'normal' window and a bandwidth of 2 GHz a resolution of 1 ns is achieved. In chapter 2 the parameters for power gain and time delay spread are defined with delta pulses. In the real situation individual pulses have non-zero widths. How does this effect the calculations? In Appendix 1 it is shown the real parameter values are only slightly influenced by this non-zero width, so this effect can be disregarded.

The measurements reported in literature to date show, as is mentioned in section 4.1, a relatively poor resolution, say 5 ns at best. As a result it is assumed that one ray is the sum of a number of smaller rays arriving at approximately the same instant. Our measurement resolution was sufficient to detect individual rays, which was checked manually by blocking them with a small piece of absorber. In Eindhoven measurements were conducted in a frequency band of 57 to 59 GHz in 8 different rooms in three different buildings: the Auditorium, the Computing Centre building and the Electrical Engineering faculty building. In two of these rooms measurements were also conducted at 41 to 43 GHz. This is done to compare the two frequency bands, because atmospheric absorbtion due to oxygen is very different for these frequencies. In chapter 5 a description of the two types of antennas used will be given.

5 Antennas for Indoor Radio Communications

The impulse response of an indoor radio channel is greatly influenced by the type of transmitting and receiving antennas used. In fact the antennas should generally be regarded as a part of the indoor channel. With the mobility of users in mind, size places a mayor constraint on antenna design. Furthermore the positioning of transmitting and receiving antennas in a room and the type of antennas is very important. Two types of antennas were considered, biconical and cylindrical horns. With these two antennas the influence of antenna type and positioning on channel behaviour was studied.

5.1 The Biconical Horn Antennas

The design of the biconical horns used in Eindhoven was first proposed by Uekanada et al [15]. This paper describes the design of a horizontally polarized biconical horn, fed by a circular wave guide, for broadcasting purposes at 12 GHz. This antenna exhibits an omnidirectional radiation pattern in the horizontal (azimuth) plane and a narrow beam in the vertical (elevation) plane.
Why use omnidirectional antennas for indoor radio? First of all a base station antenna located in the centre of an office near the ceiling should give the same coverage in every direction in the room, which gives fair access to every user in a room. An omnidirectional antenna on the remote offers the advantage of avoiding cumbersome pointing of the remote antenna towards the base station antenna. However, delay spread values are smaller if a directional remote is used, because with an omnidirectional antenna more walls will be illuminated. This effect will be verified with actual measurement results. A cross-section of the biconical horn antenna is given in figure 5.

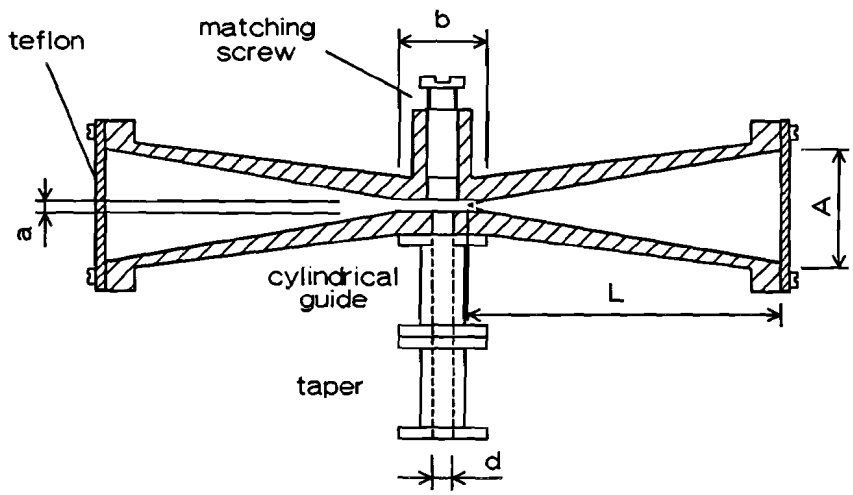

Figure 5: Cross-section of a Biconical Horn Antenna

The antenna consists of a cylindrical waveguide with inner diameter d, a radial line section with spacing a and a biconical horn section with horn length L and aperture height A. The antenna is rotationally symmetric to the z-direction (the vertical). A teflon sheet is screwed to the end of the horn section. The matching screw is used for optimizing the standing wave ratio of the antenna. Four biconical horns were designed, two for investigation of the 57-59 GHz band and two for 41-43 GHz. The 42 GHz horns are scaled versions of the 58 GHz horns, because for comparison of the two bands identical radiation patterns are required. In table 1 the antenna dimensions are summarized.

Table 1: Dimensions of Biconical Horn Antennas

	42 GHz	58 GHz
a	3.0 mm	2.0 mm
A	39.8 mm	28.8 mm
d	4.8 mm	3.5 mm
b	26.4 mm	19.1 mm
L	97.9 mm	70.9 mm

All our equipment uses standard WR 19 waveguides. The dominant mode in this guide is the TE_{01} mode, which has an electric field given by [11]

$$E_x = A.\sin(\frac{\pi y}{p}).e^{-j\beta z}.e^{j\omega t} \quad . \tag{27}$$

This rectangular guide is tapered to a cylindrical waveguide with inner diameter d. As a result of this the TE_{01} mode is transformed into the dominant cylindrical TE_{11} mode.

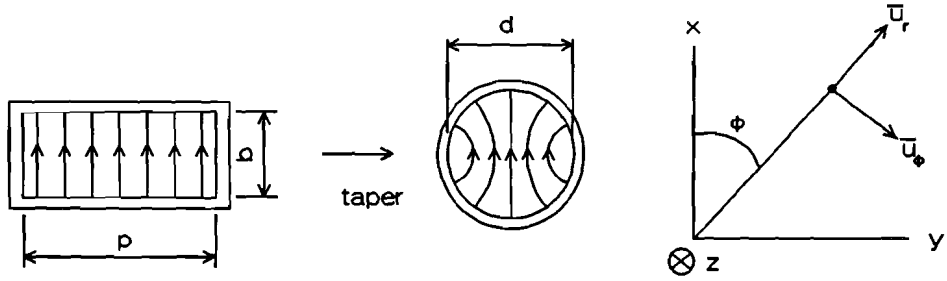

Figure 6: Mode Changing due to Tapering

The electric field formula for the TE_{11} mode is [11]

$$\vec{E} = \left[\frac{1}{r} . J_1(1.84 \frac{2r}{d}) . \vec{u}_r . \cos(\phi) - \frac{1.84 J_1'(1.84 \frac{2r}{d})}{d/2} . \vec{u}_\phi . \sin(\phi) \right] . e^{-j\beta z} . e^{j\omega t} . \quad (28)$$

J_1 is the first order Bessel function. The first derative of this function to r is J_1'. The TE_{11} mode is fed into the radial line section and launched by the biconical horn. A rotationally symmetrical antenna fed with a TE_{11} field pattern could never exhibit omnidirectional radiation characteristics in the azimuth plane. To achieve this the wave pattern has to be circularly polarized. This means that two identical orthogonal field patterns have to propagate in the guide. The two patterns must have equal amplitudes but must be 90 degrees apart in phase. This is done by inserting a quarter wave plate in the cylindrical guide, rotated at a 45° angle relative to the x-axis. The quarter wave plate is a dielectric slab, in our case made of 0.5 mm thick teflon with $\varepsilon_r = 2$ as drawn in figure 7. The ends are tapered to reduce reflections to a minimum. The incoming TE_{11} mode will be decomposed into two orthogonal TE_{11} modes polarized parallel and perpendicular to the polarizer. The parallel mode has a larger propagation constant β than the perpendicular mode.

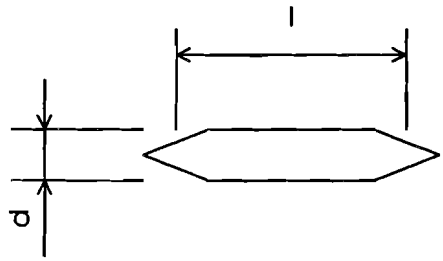

Figure 7: Teflon Polarizer

So the length of the polarizer has to be chosen in such a way that the differential phase equals 90°, therefore

$$(\beta_1 - \beta_2) . l = \frac{\pi}{2} , \quad (29)$$

where l is the effective slab length and $\beta_{1,2}$ are respectively the propagation constants of the parallel and perpendicular mode. The length l will not be equal to the point to point length, due to slab tapering. If $\cos(\phi)$ and $\sin(\phi)$ in (28) are replaced by

$$\cos(\phi - \frac{\pi}{4} + \frac{\pi}{4}) = \frac{\sqrt{2}}{2} (\cos(\phi - \frac{\pi}{4}) - \sin(\phi - \frac{\pi}{4})) \quad (30)$$

and

$$\sin(\phi - \frac{\pi}{4} + \frac{\pi}{4}) = \frac{\sqrt{2}}{2} (\cos(\phi - \frac{\pi}{4}) + \sin(\phi - \frac{\pi}{4})) , \quad (31)$$

then the total incident field in the cylindrical guide can be written as

$$\overline{E} = \overline{E_1} + \overline{E_2}\,, \tag{32}$$

where

$$\overline{E_1} = \left(\frac{1}{r}.J_1\left(1.84\frac{2r}{d}\right).\overline{u_r}.\cos\left(\phi-\frac{\pi}{4}\right) - \frac{1.84J_1'\left(1.84\frac{2r}{d}\right)}{d/2}.\overline{u_\phi}.\sin\left(\phi-\frac{\pi}{4}\right)\right). \tag{33}$$
$$.\frac{\sqrt{2}}{2}.e^{-j\beta z}.e^{j\omega t}$$

and

$$\overline{E_2} = -\left(\frac{1}{r}.J_1\left(1.84\frac{2r}{d}\right).\overline{u_r}.\sin\left(\phi-\frac{\pi}{4}\right) + \frac{1.84J_1'\left(1.84\frac{2r}{d}\right)}{d/2}.\overline{u_\phi}.\cos\left(\phi-\frac{\pi}{4}\right)\right). \tag{34}$$
$$.\frac{\sqrt{2}}{2}.e^{-j\beta z}.e^{j\omega t}\,.$$

The $\overline{E_1}$ field is polarized parallel to the slab and $\overline{E_2}$ is polarized perpendicular to the slab. Behind the slab these fields become

$$\overline{E_1'} = \overline{E_1}.e^{-j\beta_1 l}\,, \tag{35}$$

$$\overline{E_2'} = \overline{E_2}.e^{-j\beta_2 l} = \overline{E_2}.e^{-j\beta_1 l}.e^{-j(\beta_2-\beta_1)l} = j\overline{E_2}.e^{-j\beta_1 l}\,. \tag{36}$$

This is circular polarization.

The length l of the polarizer is determined experimentally with the network analyzer's 85105A mm-wave test set. Both tapers were connected to the WR19 test port flanges as shown in figure 8.

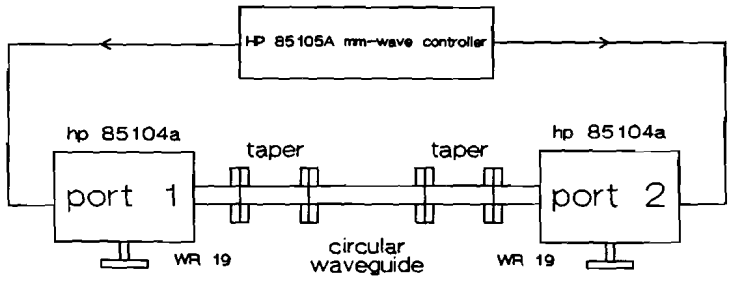

Figure 8: Measurement Setup for Polarizer Phase

The differential phase delay between the two modes is measured as follows: Two 'through' (S_{21}) responses were used as calibration reference measurements at 41-43 GHz and 57-59 GHz. The polarization of the incoming wave is vertical, i.e the field pattern of figure 6 is directed towards the ceiling of the room. Next, the dielectric slab was placed horizontally in the round wave guide. The phase response $\beta_2 l$ was measured and stored to memory. After this the slab was rotated through 90 degrees and the measured $\beta_1 l$ was compared to $\beta_2 l$ by calculating the quotient of the two responses. The slab length was adjusted until the differential phase equalled 90° ± 1°. The differential amplitude was less than 0.01 dB. The measured phase response of the two polarizers are drawn in figures A.1 and A.2.

Does the circular polarization in the wave guide generate a circularly polarized radiation field? No! The polarization state of the radiation field is determined by the spacing distance a of the radial line section. If a in figure 5 is smaller than $\lambda/2$ then the only mode which can propagate through the radial line is the TM_{10} to z mode, which has a z-directed (direction is defined in fig.6) electric field [15]. This results in a vertically polarized radiation field. For larger a multiple modes, TM_{11}, TM_{10} and TE_{11}, can propagate through the radial line, resulting in elliptical polarization [15]. Uekanada [15] needed horizontal polarization for broadcasting purposes. He therefore chose $\lambda/2 < a < \lambda$ and suppressed the TM modes in the radial line with metal posts. Because these posts are difficult to manufacture a is chosen to be 2 mm (0.4 λ) at 58 GHz and 3 mm (0.4 λ) at 42 GHz. This results in a 25 dB ratio between vertical and horizontal polarization in the azimuth plane, so good polarization purity is obtained. A smaller spacing of the radial line causes an increase of reflected power in the antenna. Adjusting the radial line spacing means finding a compromise between the standing wave ratio and polarization purity of the biconical horn antenna.

5.1.1 Standing Wave Ratios of the Biconical Horns

A very important characteristic of an antenna is the standing wave ratio (SWR) in the antenna feed. The SWR is a measure for the wave impedance mismatch between feed and antenna. A poor match, i.e high SWR, indicates that a considerable portion of the incident power will be reflected back into the feed. The standing wave ratio is related to the reflection coefficient ρ according to

$$SWR = \frac{1 + |\rho|}{1 - |\rho|} . \qquad (37)$$

An antenna with a SWR smaller than 2 is generally considered to be well matched. In figures B.1-B.4 the measured ratios of all four biconicals are given. The measurements were performed with the mm-wave S-parameter test set. A shorted WR19 guide was used for reference calibration. The SWRs could be minimized with the matching screw on each antenna. All four antennas have SWRs less than 1.8 in a 2 GHz bandwidth, so the reflection coefficient for all antennas is smaller than -11 dB, indicating than more than 90 % of the incident power is actually transmitted

at each frequency. These are conservative figures; on average the SWRs are smaller than 1.8. The reflected power causes a decrease in link budget. Because the reflected power is the same for all measurements, conclusions regarding power decay rates will still be valid.

5.1.2 Elevation Radiation Patterns of the Biconical Horn Antennas

The radiation pattern in the elevation plane of the biconical horn is determined by the horn dimensions L and A. The path length l from the apex to the aperture increases toward the horn mouth edges. Therefore the aperture plane is not an equi-phase plane. This complies with the aperture distribution of an E-plane sectorial horn antenna with length L and aperture width A in the E-plane. The radiation pattern in the elevation plane of the biconical can be calculated by the methods described for sectorial horns exited with a TE_{01} mode. The elevation electric field pattern, defined as $|F(\theta,s)| = |E(\theta,s)| / |E(0,s)|$ can be expressed as [19]

$$|F(\theta,s)| = \frac{1+\cos(\theta)}{2}\left[\frac{(C(r_2)-C(r_1))^2+(S(r_2)-S(r_1))^2}{4(C^2(2\sqrt{s})+S^2(2\sqrt{s}))}\right]^{\frac{1}{2}}, \tag{38}$$

where $C(x)$ and $S(x)$ are the Fresnel integrals and

$$r_1 = 2\sqrt{s}\,(-1-\frac{1}{4s}(\frac{A}{\lambda}\sin(\theta))) \quad , \quad r_2 = 2\sqrt{s}\,(1-\frac{1}{4s}(\frac{A}{\lambda}\sin(\theta))) \, , \tag{39}$$

with

$$s = \frac{1}{8}(\frac{A}{\lambda})^2\frac{\lambda}{L} \, . \tag{40}$$

The parameter s is also known as the phase error parameter.

5.1.3 Measured Biconical Horn Antenna Radiation Patterns

The radiation characteristics of the antennas were measured in an anechoic chamber, using the setup and calibration procedure as described in chapter 4. The antenna under test (AUT) was placed on a rotating platform. An open-ended WR19 guide was used as a transmitting antenna on the remote at the same height as the AUT. For the calibration measurement some arbitrary direction φ was chosen in the plane of maximum radiation $\theta = \pi/2$. The vertical polarization is defined as co-polarization because the AUT is expected to radiate this polarization. Cross-polarization was measured by rotating the WR19 guide on the remote through 90°. In figures C.1-C.4 the co-polar radiation patterns, in the azimuth plane, of all four antennas are drawn. These figures represent the time domain response measured

in a 2 GHz bandwidth. This representation is chosen because the antennas are not frequency independent, and analysis of measured responses is performed in the time domain. By representation in the time domain the frequency dependency is 'averaged' by the Inverse Fourier Transform. Because of the calibration procedure the position (i.e. time) is known to be 0 metres (0 s).

In all antennas a small dip in the pattern is observed for $\varphi = 270°$. This is caused by a maintenance hole in the teflon support. Because EM waves have a different phase delay in teflon than in air, destructive interference is responsible for a dip in the direction of the maintenance hole. The horns are not completely omni-directional in the azimuth plane. The 42-Ghz antennas have a variability of less than 3 dB. The 58-GHz horns are slightly worse: 7 dB. This could be caused by skewness of the radial line or misalignments of the polarizers. Although figures C.1-C.4 indicate that the antennas are not perfectly omnidirectional in the azimuth plane it should be noted that if a number of measurements are made in a single room, overall path statistics should not be influenced by specific directional antenna behaviour. The influence of a polarizer on the radiation pattern is clearly demonstrated by comparing figures C.4 and C.5. Without the polarizer definite zeros in the radiation pattern can be observed. Clearly the polarizers 'fill' these zeros, giving a great improvement in omnidirectionality.

In figures C.6-C.9 the measured co-polar elevation radiation patterns are given. From these diagrams a 3 dB beamwidth of 9° can be derived for all biconical horns. These beamwidths are small, but as will be seen in the indoor radio propagation experiments, this gives a near uniform coverage in a room if transmitting and receiving antennas are placed at different heights.

The rapid fluctuations in the elevation patterns around $\theta = 0°$ and 180° are rather remarkable. They caused by a diffraction effect, this is modelled as radiation from the aperture edge (line sources). This effect is described in [20] for sectorial horns. This antenna property does not have to be unfavourable! It means that if a remote is located directly beneath the base station antenna it could still receive a significant amount of signal power via the direct LOS path. The difference in behaviour for $\theta = 0°$ and 180° is caused by the antenna measurement setup. A supporting post caused partial shadowing for $\theta = 180°$. In figure 9 the theoretical radiation pattern of a E-plane sectorial horn with dimensions A and L of table 1 at 58 GHz is compared to a measured biconical horn antenna at the same frequency. Good overall agreement between theory and practice is observed.

The co- to cross-polar ratio in the azimuth plane is for all four antennas better than 25 dB. As an example figure C.10 shows this ratio for a 58 GHz horn. The cross-polar radiation level in the elevation plane is more or less constant at 25 dB below maximal radiation and peaking to -10 dB at $\theta = 0°$, see figure C.11. The antenna radiation patterns are frequency dependent, as can be seen in figures C.12-C.15. In figure C.16 the azimuth radiation pattern of a 58 GHz horn without polarizer is drawn. This figure clearly demonstrates that the dependency can not be completely

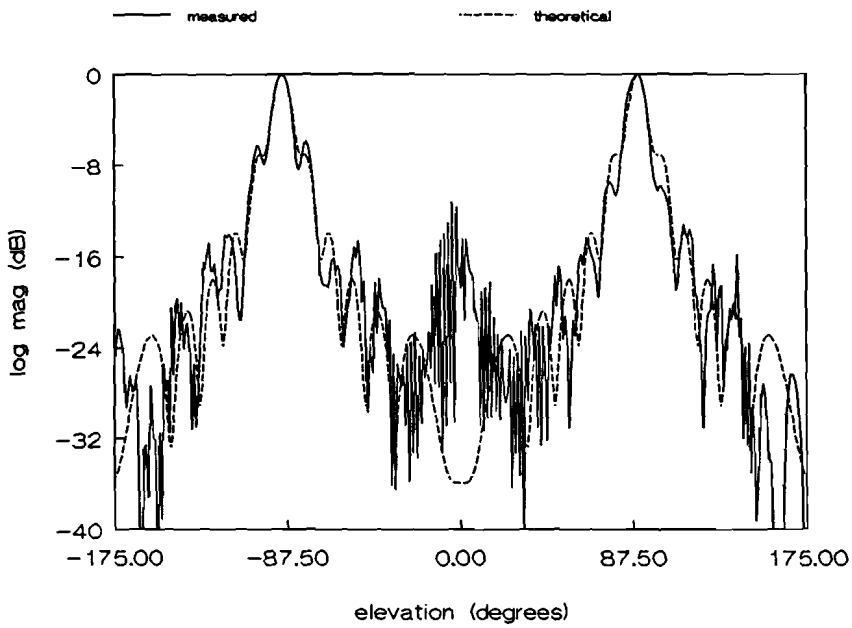

Figure 9: Comparison of Practical and Theoretical Biconical Horn Elevation Pattern

attributed to the use of a polarizer, although the polarizer is a frequency dependent device by definition. Overall frequency dependency is probably caused by a combination of polarizer and frequency dependent standing wave ratio. In addition to this the radiation pattern according to (38)-(40) are also frequency dependent.

5.1.4 Directivity of Biconical Horn Antennas

Because of the calibration procedure used in measuring antenna radiation pattern the actual power gain of the biconicals could not be determined directly. Also a standard gain horn for the mm-wave band was not available. The directivity however, could be estimated by pattern integration of the measured characteristics. The directivity D of an antenna is defined as [19]

$$D = \frac{4\pi . |E(\theta=\pi/2,\phi)|^2}{\int_0^{\pi}\int_0^{2\pi} |E(\theta,\phi)|^2 \sin\theta d\theta d\phi} . \tag{41}$$

The directivity is estimated from measured radiation patterns as follows:
The power for $\theta=\pi/2$ normalized to zero by the calibration procedure. The denominator of (41) is proportional to the total radiated power. The total power is estimated by independent integration of the measured co-polar azimuth and elevation patterns, i.e. two directivities are calculated. One directivity is calculated with the measured elevation pattern and zero dB directivity in the azimuth plane, and visa versa for the measured azimuth radiation pattern. The overall directivity

of (41) is then estimated by averaging the two calculated directivities. Results for two antennas are drawn in figures D.1 and D.2. Average directivity is 9.0 dBi for both 42 and 58 GHz horns. The actual power gain G of the antenna is smaller than D. For G the directivity should be multiplied with the antenna losses, i.e. dissipation in the antenna and reflection coefficients due to mismatches.

The biconical horn antennas designed for indoor radio channels as described in the sections above have a high directivity with corresponding small beamwidth and are well matched to a rectangular waveguide in a 2 GHz frequency band. Although the horns are not frequency independent and not completely omnidirectional in the horizontal plane it is expected that this variability will not have a significant influence on multipath statistics in a single room.

5.2 The 58 GHz Circular Horn

In this section the behaviour of the circular horn is briefly discussed.
A cross-section is drawn in figure 10.

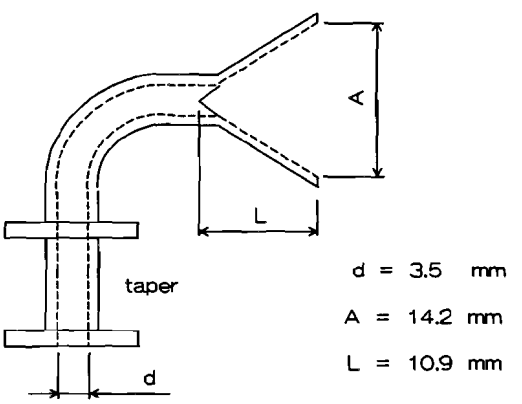

Figure 10: Cross-section of Circular Horn

This horn was used to investigate the improvement in delay spread due to directional antennas. It was used as a base station in the corner of a room and as a remote. The measured co-polar azimuth and elevation radiation patterns of this antenna are depicted in figures E.1 and E.2. From these figures a 3 dB beamwidth of 27° in both planes is derived. Theoretical expectation of the beamwidths in these two planes are approximately 24° [19]. Average directivity of this antenna (fig. E.4) is 15.2 dBi (theoretically 17 dBi) and the SWR ratio is less than 1.8 (fig. E.3). The circular horn is therefore also well matched to a rectangular WR19 guide.

In this chapter an overview of the antennas used has been given. In chapter 6 a description of the measured indoor environments will be presented.

6 The Indoor Measurement Environments

In order to study the indoor radio characteristics of single rooms, eight different rooms in three different buildings at the EUT were the subject of propagation experiments. The rooms were chosen because of their size according to the COST 231 definitions in chapter two. Also three smaller rooms of approximately equal dimensions were studied because they had distinctly different types of walls. Difference in radio behaviour in these rooms could therefore be attributed to the difference in reflection properties of the walls. In each room at least 20 measurements were conducted at randomly chosen positions throughout the whole room at 57-59 GHz. Moreover 6 additional measurement series were conducted in two rooms with different base station and remote setups and at 41-43 Ghz for comparison purposes.

A total of some 300 measurements were performed. In the rectangular rooms the coordinates of T_x and R_x at each measurement position were noted for eventual comparison with simulation and measurement repeatabilitity. Also some rudimentary reflection coefficient measurements were done in these rooms for simulation purposes. In the other rooms only the horizontal distance between transmitting and receiving antennas was administrated at every position. With this horizontal distance, and the height difference between T_x and R_x, the LOS distance can be calculated for determination of the radio coverage.

During all measurements the channels were stationary, i.e. nothing moved while a measurement sweep was in progress. One sweep took 2 minutes to complete. At every position the antennas were levelled horizontally with a water-level. The operators took up the same position in all measurements of a series, that is standing at the same position or sitting in the same chair. No objects were moved during a whole measurement series.

Research was mainly concentrated on frequencies around 60 GHz because these frequencies suffer a strong attenuation of 15 dB/km due to spectral absorbtion by oxygen, so signals which leak through windows of an office building decay rather fast outside the building. This is desirable from a security point of view. However, atmospheric absorbtion inside a room is expected to be negligible compared to free-space losses, because indoor propagation distances are, in practice, limited to a few hundred metres. For example: At 60 GHz the free-space loss over a propagation distance of 100 metres is -108 dB, the atmospheric absorbtion will only be -1.5 dB. Another reason for researching these frequencies is that these frequencies will actually be allocated to indoor radio communications [23].

In F.1-F.8 the measurement positions in every room are documented. A summary of the type of walls, floor and ceiling per room is also presented in this section of part 2. In the next sections of this chapter a detailed description of each room will be given. This should give other researchers an impression of the environments.

6.1 Corridor in the Computer Centre Building

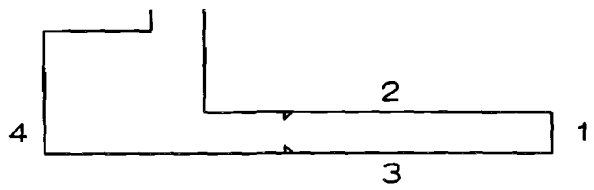

Figure 11: Layout Corridor

Dimensions h*w*l: 3.12 m*2.43 m*44.68 m. Walls 1 and 4, in figure 11, are glass doors encased in a steel frame. Walls 2 and 3 are made of painted metal walls to a height of 2.50 m and glass windows above. Metal doors leading off to class-rooms are a part of these walls. Swivelling glass doors framed with wood are located half way down the corridor . These doors were open during measurements. The floor is covered with thin carpeting and the ceiling is made of aluminium profiles with TL lighting armatures. One measurement series of 21 positions at 57-59 GHz was performed with a centrally placed biconical horn antenna base station at 2.75 m height and a biconical remote at 1.38 m. The corridor was completely empty except for the remote trolley and base station tripod.

6.2 Computer Room in the Computer Centre Building

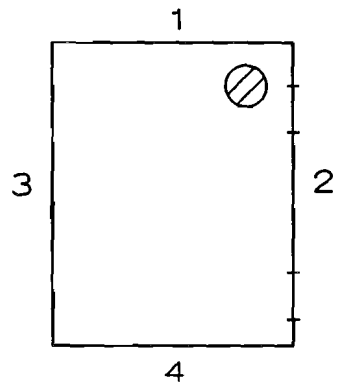

Figure 12: Layout Computer Room

Dimensions h*w*l:3.12 m*8.65 m*9.86 m. This room is a rectangular room leading off from the corridor described in 6.1. It is a class-room with 20 PCs lined up against walls 2,3 and 4. Wall 1,2 and 4, in figure 12, are the same as the metal walls in 6.1. Wall 3 is made of large floor to ceiling thermopane glass windows encased in a steel frame. Floor and ceiling are the same as the corridor. A round concrete pillar with a diameter of 1.9 m is located in a corner. Wooden chairs and tables with metal legs are lined up through the room. A blackboard and overhead

projector screen are situated in front of wall 1.
Four measurement series were conducted in this room at 25 random positions. In series 1 an omnidirectional antenna at 2.75 m was used as a base station and the same type of antenna as a remote at 1.38 m height. The setup is the same for series 2 except for the base station height which now is 1.60 m. Series 3 setup is also the same as 1 except the frequency is 41-43 GHz. The same positions were used in all series. In series 4 a directional circular horn at 2.75 m in a corner was used as a base station and an omnidirectional biconical horn as a remote at 1.38 m height. The circular horn was levelled horizontally and aimed diagonally into the room, toward the concrete pillar.

The Computer Room and the Corridor can be characterized as worst case rooms for reflectivity values of walls, for metal has a reflection coefficient of 1, independent of the incident angle and polarization.

6.3 Vax Room in the Computer Centre Building

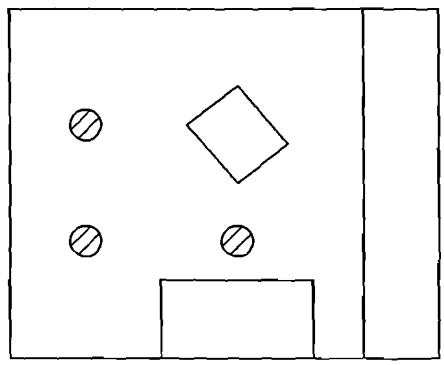

Figure 13: Layout Vax Room

Dimensions h*w*l: 3.12 m*32.20 m*33.50 m. In this room the EUT's computing power is concentrated. The room has a very complex shape, with bare concrete walls, one metal wall (same as corridor) and two glass walls. The structure drawn in the centre of figure 13 is also made of concrete. The ceiling is the same as the Corridor and Computer Room. The floor is linoleum glued on concrete. A lot of large metal cupboards, filing cabinets and mainframe computer equipment are dominant objects in the room. Several supporting pillars with the same dimensions as the one in the Computer Room are present. 20 Measurements at 57-59 GHz were performed with an cental omni base station at 2.75 m and an omni remote at 1.38 m height. The metal objects had a profound influence on channel behaviour, causing random and very strong peaks even at large time delays.

6.4 Reception Room in the Auditorium Building

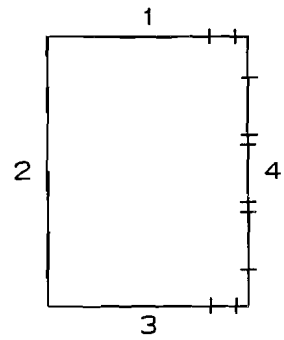

Figure 14: Layout Reception Room

Dimensions h*w*l: 4.50 m*11.15 m*24.30 m. The Reception Room in the auditorium building is a perfectly rectangular room. Walls 1 and 3 in figure 14 are covered with smooth wooden panels. Wall 2 is completely windowed from floor to ceiling, double thermopane glass in a steel framework. Very thin see-through curtains cover the whole of this wall. The ceiling is somewhat irregular, plastic grids cover air-conditioning piping and lighting armatures. A number of ball shaped glass chandeliers are suspended at 1.50 m below the ceiling. Wall number 4 consists of large wooden doors and wood panelling. Lush wall-to-wall carpeting covers the floor.

During measurements the room was all but empty, except for some chairs and tables along walls 1,2 and 3. Four series were done here at 25 positions. In two series, one at 57-59 GHz and the other at 41-43 GHz, a centrally placed biconical horn antenna at 3.00 m was used as a base station and a biconical remote at 1.38 m height was moved around the room. In the third series a circular horn was situated in a corner at 3.00 m height as a base station and the same remote as in series 1 and 2 was used. The frequency was 57-59 GHz for this series. The circular horn was aimed diagonally into the room and levelled horizontally. The fourth and last series the same base station as in 1 and 2 was used, but the circular horn was used on the remote instead. The frequency for series 4 is 57-59 GHz. The circular horn was used at 1.50 m height and aimed horizontally at the central base station at every position. For all four series the same positions were used.

6.5 Hall in the Auditorium Building

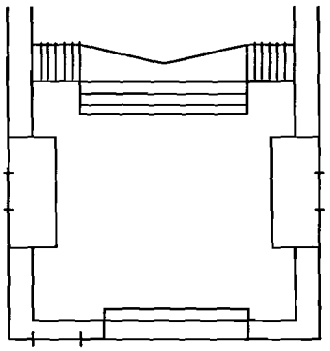

Figure 15: Layout Auditorium Hall

Dimensions h*w*l: 8.5 m*41 m *43 m. This room is the largest room measured. It is a very complex shaped hall, two storeys high. Dominant objects are four staircases which lead to the balustrade of the second floor and a large organ on the second floor. The walls are mainly bare concrete with windows on the ground floor. The floor is linoleum glued on concrete. Some tables and chairs are scattered throughout the hall. One measurement series at 57-59 GHz, 22 positions, with a central omnidirectional base station at 3.00 m height and omni remote at 1.38 m, was performed. Horizontal separation distances between transmitting and receiving antennas of up to 31 metres were achieved.

6.6 Amphitheatre in the Auditorium Building

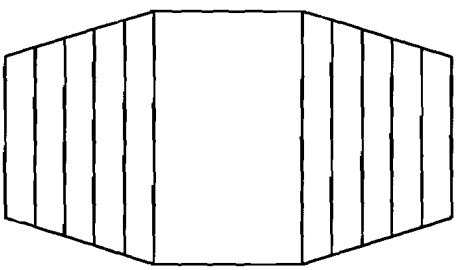

Figure 16: Layout Auditorium Amphitheatre

Dimensions h*w*l: 7.2 m*21.0 m*30.0 m. The concrete walls of this room are covered with acoustic absorbent materials. The floor in the middle of the room, on which remote and base station were located, is made of wood. One measurement series at 21 positions, with the same configuration as in the Hall, was conducted. Cushioned chairs are placed in a amphitheatre-like manner on two sides of the central floor. A number of chairs are also lined up on the central floor. The remote

was moved randomly among them. The ceiling is covered with plastic panelling with TL lighting armatures and some spotlights.

6.7 Lecture Room in the Auditorium Building

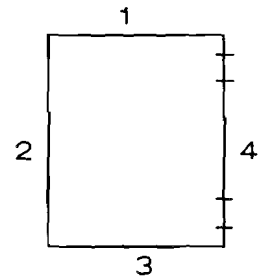

Figure 17: Layout Lecture Room

Dimensions h*w*l: 4.00 m*8.85 m*12.85 m. This rectangular room is a typical classroom configuration. Large glass windows in a steel framework from 1 m to ceiling and concrete beneath make up wall 2 of figure 17. A dominant feature of this room is that the other walls are completely covered with wooden lathing. Linoleum covers the concrete floor. The ceiling is covered with TL lighting armatures. Tables and chairs are lined up throughout the room. A blackboard and small overhead projector screen cover wall 1. One series at 18 positions was conducted at 57-59 GHz with the same system configuration as the Corridor. The room was empty except for tables, chairs and our network analyzer. There were no metal cupboards in the room.

6.8 Room 11.21 in the Electrical Faculty Building

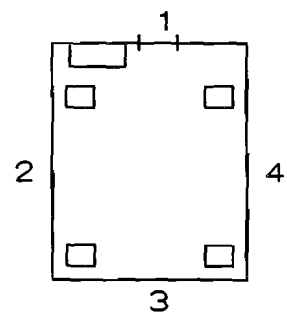

Figure 18: Layout Room 11.21

Dimensions h*w*l: 3.07 m*7.30 m*11.30 m. One measurement series at 20 positions, frequency 57-59 GHz with the same setup as the Lecture Room was conducted. Walls 1,2 and 4 in figure 18 are smoothly plastered concrete. Wall 3 consists of glass windows from 1 metre to ceiling in a steel frame and a metal

heating radiator case below. The floor is linoleum on concrete. Four square (0.5*0.5 m^2) concrete supporting pillars and a metal cupboard in a corner are dominant objects in this room. A number of large wooden benches with wooden shelves on top are located in the room. The shelves are 1.5 metres high. The ceiling consists of aluminium plates and TL tubes.

The rooms can basically be split into 3 categories:

1) very large complex structures namely the Vax Room in the computing centre building and the Hall and Amphitheatre of the Auditorium building;
2) the long narrow structure of the Corridor in the computing centre building,
3) the rectangular rooms: Reception Room, Computer Room, Lecture Room and Room 11.21.

7 Presentation of Measurement Results

In this chapter the characteristic indoor radio channel parameters: total multipath power gain G, time delay spread σ and power decay rate m as defined in chapter two are presented for all 14 measurement series in the eight rooms. Average power delay profiles will also be defined and discussed. All analysis is performed on time domain data only. Frequency domain data is, however, also available. For the calculation of G and σ all data points are used, because appendix 1 indicates that, especially for σ, non-zero pulse width only has a small influence on parameter calculation. The power decay rate will be derived from measured total multipath power gains versus line-of-sight distances.

A comparison of parameters in different rooms will be given and the influence of channel setup on channel behaviour is discussed. All calculations are performed in exactly the same manner for all rooms. The same calibration procedure was used and equipment warm-up time was also the same everywhere. So all conclusions regarding differences between rooms and setups are justifiable.

Practically all our measurements concerned line-of-sight (LOS) channels. To evaluate the change in channel behaviour if something or somebody should block the LOS path the data points of this path were mathematically removed from the time domain impulse responses. This is confirmed by experiments, the LOS ray disappeared completely if it was blocked by a piece of absorber. The profiles with obstructed LOS path will be designated as OBS channels. Results will show that obstruction of the LOS path can change the channel parameters significantly for some environments, while in other rooms the parameters are hardly changed at all.

7.1 Average Power Delay Profiles

The power delay profile $p(t)$ as defined in formula (11) of chapter 2 is calculated from the complex time domain impulse response data according to

$$p(t) = (Im(h(t)))^2 + (Re(h(t)))^2 \ . \tag{42}$$

The power delay profile p(t) is not only a function of time but also of the positioning of transmitting and receiving antennas, so

$$p(t) = p(t,k) \ , \tag{43}$$

where k represents the channel position in a room, i.e. positions of T_x and R_x. The overall radio channel behaviour of a single room can best be described by some form of average power delay profile per series. In calculating the average profile each individual profile is weighed by its own total multipath power gain $G = G(k)$, because a single profile should not dominate the average profile.

Therefore the average power delay profile is defined as

$$p_{av}(t) \triangleq \frac{1}{N}\sum_{k=1}^{N} \frac{p(t,k)}{G(k)} \,. \tag{44}$$

In formula (44) N denotes the number of measurements per series. The time axes of the individual profiles are aligned in such a way that all line-of-sight rays are located at zero seconds delay. Averaging is performed over actual power values, **not** dB values. All 14 measured average power delay profiles are drawn in figures G.1-G.14. For large t (> 350 ns) nearly all profiles converge to the system noise floor except for the Corridor and the Hall (fig. G.5 and G.6). The Corridor has metal walls, causing slower decay of ray power with time. The Hall is very large, so reflected rays will be received at very long delays. Rather remarkable is that a linear slope can be defined for all rooms. This is consistent with the exponential decay of individual rays first suggested by Saleh and Valenzuela [5], since the power in dB decays linearly. For small t (< 100 ns) the power in most average profiles does not follow the same linear decay, but remains more or less constant. This is caused by the high elevation directivity of the antennas used (antenna gain compensation of the free-space losses, this will be explained in section 7.2), so ceiling and floor are not illuminated very strongly. Rays which arrive just after the LOS ray must be reflections against floor and ceiling, because the height is the smallest dimension of a room. The linear slope therefore mainly describes reflection properties of walls only.

The antenna radiation pattern influence on average channel behaviour is illustrated by figure 19 and 20 where a comparison of simulations of the Reception Room with isotropic (i.e. omnidirectional in both elevation and azimuth planes) and biconical horn antenna radiation patterns is made. For the radiation field in the elevation plane of the biconical horns a look-up table of a measured pattern is used. The elevation directivity of the biconical horns causes a shift in absolute power level of reflected rays. The slope is however the same for both simulations.

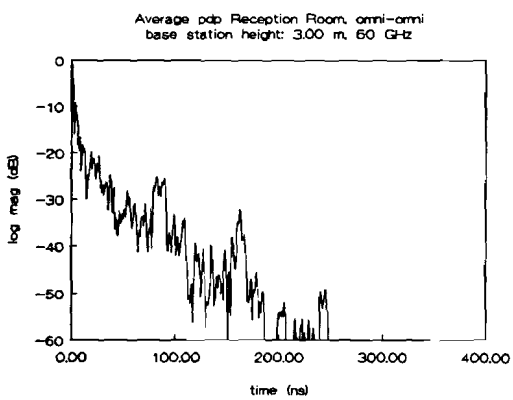

Figure 19: Simulation with Isotropic Antennas

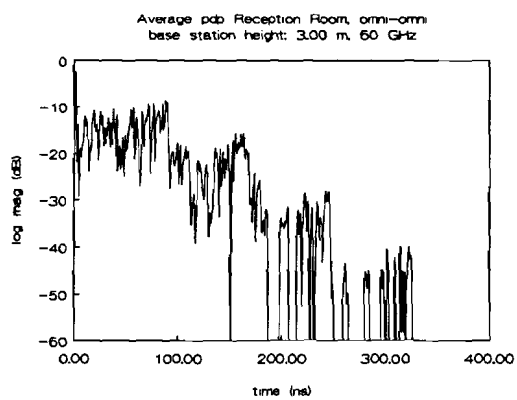

Figure 20: Simulation with Biconical Antennas

Note that isotropic antennas would yield much smaller time delay spread values, because the 'width' of the profile is smaller. Time delay spread values are approximately 50 % smaller with isotropic antennas in stead of biconical horn antennas in this room.
A key result is the slope of the three small rooms: Computer Room, Lecture Room and Room 11.21. Antenna heights are the same in these rooms. Very different average channel behaviour is observed (fig. G.1-G.3). Because the rooms are approximately equal in size the slope diversity can be completely attributed to the change in reflectivity values of metal, wooden and concrete walls respectively.

The slopes of the average power delay profiles are determined by fitting a straight line through the central section of the profiles. The start and stop times of the central section are determined visually from the average power delay profiles. The noise for large t and the first part of the average profiles are not include in the fit, so the logarithm of $p(t)$ is modelled as

$$10.\log(p(t)) = A + B.t \ . \tag{45}$$

A measure for goodness-of-fit is the correlation coefficient R of the fitted line and data, R equals 1 for a perfect fit. In appendix 2 the fitted slopes and corresponding correlation coefficients are given for all measurement series. Values between 0.058 and 0.28 dB/ns are observed. The slopes will be used for statistical modelling of the channels. The validity of the slope values was checked by sub-dividing the profiles of one series into two classes. The first class contains profiles whose total multipath power gain exceeds the average gain for that series. The second class contains profiles with gains less than average. The line fitting procedure was repeated for both classes. The slope values in both classes were the same as the ones found for all profiles, only the correlation coefficients were smaller.

Comparison of figures G.1 and G.9 show that a difference in base station height in the Computer Room does not affect the average profile very much, only the LOS paths are stronger for a low base station, due to the overlap of main beam elevation radiation patterns of transmitting and receiving antennas. The profile of the corner base station (fig. G.10) setup in the Computer Room is not very different to an omni-omni setup. In the Reception Room, however, large differences due to setup changes are observed (fig. G.11-G.12). The circular horn beamwidth, apparently, is not large enough for a uniform coverage in the Reception Room. Positions in corners which are not illuminated by the circular horn will have a poor power gain. Average channel behaviour for these setups is less uniform than a omni-omni setup, this shows as large deviations from the linear slope and lower values for the correlation coefficients. The Vax Room (fig. G.7) has an even lower power decay slope than the Computer Room (fig. G.1). This a result of large metal objects situated throughout this room which cause very strong single reflection paths, even for large time delays. An example of strong reflections is position 16 in the Vax Room, drawn in figure 21. The Corridor (fig G.5) has the lowest power slope, due to highly reflective side walls and its long narrow structure. Because of this structure

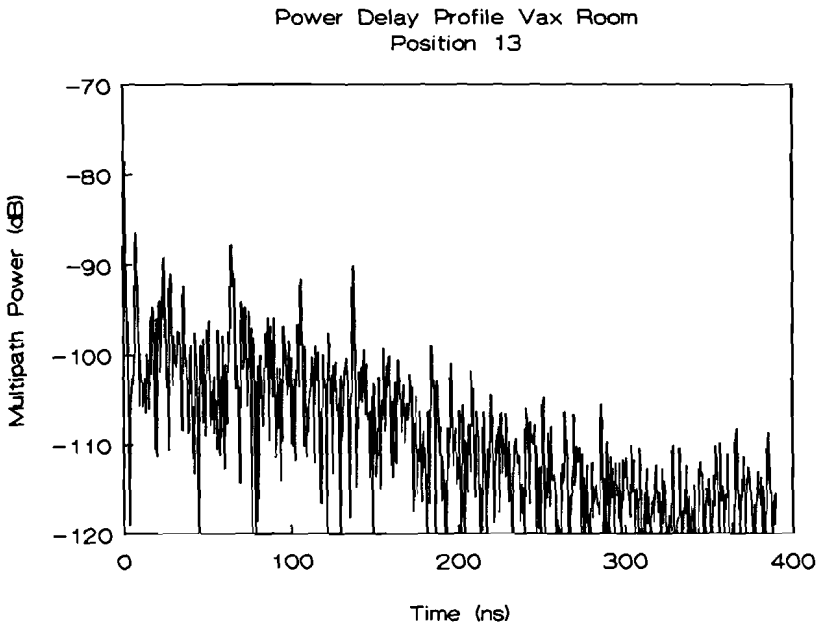

Figure 21: Typical PDP in Vax Room

rays will reflect at grazing incident angles ($\theta_i \approx 90°$) on floor, ceiling and side walls. The parallel and perpendicular polarization reflection coefficients in formulas (22) and (23) approach unity at grazing incident angles. Reflections against the long ends of the Corridor show up as clear peaks in the average profile (fig. G.5).

Comparison of figure G.13 with figure G.1 and figure G.14 with figure G.4 shows that a change in measurement frequency hardly influences average channel behaviour at all. This could imply that reflection coefficients of building materials do not change significantly in the mm-wave band, or that atmospheric absorbtion does not play an important role in indoor channel behaviour, because at 40 GHz oxygen absorbtion is less than 0.1 dB/km compared to 15 dB/km at 60 GHz. Allen en Hammoudeh [13] do report differences in performance at 40 and 60 GHz, using vertically polarized, omnidirectional antennas. However, the antennas were not scaled, so a comparison of radio propagation in the two frequency bands is not really justified in their case.

In chapter 2 formulas were presented for relative errors in G en σ for exponentially decaying power delay profiles. What is the largest error made in G and σ by chopping profiles at t = 400 ns? All average profiles, except for the Corridor and the Hall (fig. G.6) have reached the system noise floor at 400 ns. Using the fitted slope for calculation of the dynamic ranges in these two rooms yield relative errors of 0.5% and 13.9% for G and σ in the Corridor. For the Hall these errors become 0.14% and 5.2% respectively for G and σ. These are worst case errors; all other slopes are larger and will therefore result in smaller errors. These calculations indicate that only for σ of the Corridor a substantial error is made. This will also show, incidentally, in the time delay spread versus maximum time. A definition of

sigma versus maximum time will be given in section 7.5.

7.2 Total Multipath Power Gain G and Power Decay Rate m

In chapter 2.5 a relation is defined between the total multipath power gain G and radio coverage through the power distance decay exponent m. In (21) d denotes the LOS distance. The importance of a good signal coverage in a room was already mentioned, for it determines the signal power needed for a good signal-to-noise ratio in the whole room. Equal signal power or uniform radio coverage in an office suite pico-cell for example, would therefore be a desirable feature of an indoor wireless communication system for it would give each user fair access to the system. Formula (21) indicates that received power decreases with separation distance due to inverse square free-space loss. However, the inverse square law could be compensated for if the line-of-sight antenna gains are distant dependent. This would mean that $G_t = G_t(d)$ and $G_r = G_r(d)$ would have to increase with the LOS distance d. This is the case if two antennas with high elevation directivities, with a maximal radiation in the horizontal plane, are used at different heights for base station and remote. The antenna compensation of the inverse square law is illustrated in figure 22.

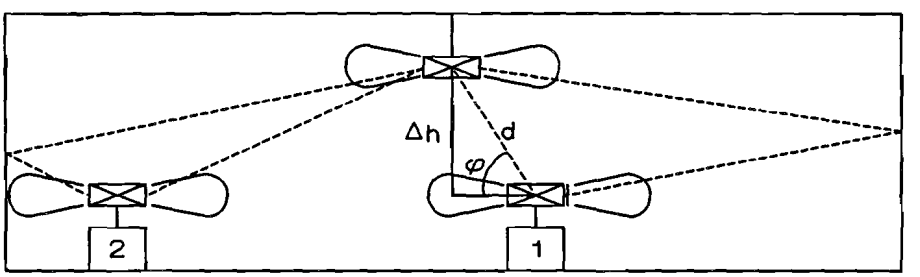

Figure 22: Compensation of Free-Space Power Loss by Antenna Gains

Remote 1 experiences a smaller LOS antenna gain than remote 2, but has smaller free-space loss and visa versa for remote 2. Each reflected ray also adds to the total received power and must also at least obey an inverse square power distance law of formula (21) for perfectly reflecting walls. Individual rays will decay faster if the reflection coefficients of the walls are less than unity. Compensation of individual reflected rays could also occur. For large d, φ approaches zero and the LOS power versus distance decay rate must obey the free-space law again, i.e. $m = 2$. It can be shown that, using the theoretical elevation gain formula (38) of the biconical horn antennas and a height displacement Δh of 1.5 metres, antenna gains could compensate the free-space losses for LOS distances between 6 and 48 metres to within $\pm$ 3 dB, resulting in nearly uniform coverage for a pico-cell. For smaller d the received power will drop rapidly. In figures H.1-H.14 the measured total power gains G versus LOS distances d are drawn for all measurement series. Both OBS

and LOS situations are considered. The power-distance decay exponent was defined as

$$G \propto d^{-m} . \tag{46}$$

In figures H.1-H.14 the following relationship is depicted

$$10\log(G) = A + B\log(d) . \tag{47}$$

For determination of m a line is fitted in these charts and m equals $-B/10$. Note that the value of m is not only determined by the separation distance d, but also by the antenna elevation gain compensation. The fitting procedure minimizes the mean square error (MMSE). For the large rooms, including the Reception Room and the Corridor, only the position with $d > 6$ metres are included for the fit. For the smaller rooms all positions are included. For these rooms the total multipath power G even increases with d (negative m). Negative values of m only occur in the small rooms with small separation distances. The variability of azimuth radiation patterns of the biconical horns could be responsible for a greater spread in the LOS paths power. Fitted values for the LOS power decay rates should therefore be evaluated as expectation values of the real decay rates. A table with measured power decay rates is given in appendix 3. Values between -1.65 and 0.49 for m are observed for LOS situations with two biconical horns. Values are larger for obstructed channels. For the large rooms m only varies between 0.1 and 0.49 for LOS. For OBS in these rooms the range is -0.05 to 0.75.

Each room will be discussed in more detail.
In the Computer Room (fig. H.1) the LOS ray is not dominant at all for a Δh of 1.4 metres. This shows as nearly equal power for the LOS and OBS case. The equality between LOS and OBS implies that all power is received via reflections. Only a slight drop in power for small d is observed. In figure H.9 the biconical horn antennas are nearly at the same height. Not only do the LOS rays fall well into the main lobes of the antennas, but also a larger number of reflected rays via the metal walls. This causes an average increase in total power of 10 dB, i.e. -60 dB in stead of -70 dB. The contribution of the LOS rays to the channel response is much larger in this setup. Difference in power between LOS en OBS channels is greater than 3 dB for this setup at almost all positions, this indicates that more than half of the signal power is received via the direct line-of-sight path. Because the Computer Room is a small room with highly reflective walls (small reflection loss in reflected rays) the power does not drop for larger d, but remains constant. This cannot be accredited to antenna compensation, because the height displacement is only 20 cm. The free-space loss remains small because propagation distances are small.

If the Lecture Room and Room 11.21 (fig. H.2 and H.3) are compared to the Computer Room (fig. H.1) a number of things are apparent: For the LOS channels a definite increase in power with distance is observed, caused by antenna gain compensation. This is especially true for the Lecture Room which has an m of -1.65.

The decay rate for Room 11.21 is -0.59. The power decay rate is positive for the OBS channels, so for larger d's a significant part of the total power is received via the LOS path. Furthermore the overall power per measurement position increases with the reflectivity of the wooden, concrete and metal walls from -80 through -75 to -70 dB. If we look at the difference between LOS and OBS for increasing distances then we can conclude that these differences increase with a decrease of wall-reflectivity. Highly reflective walls are favourable for radio coverage.

In the Reception Room (fig. H.4) the separation distances are greater than in the small rooms. An increase in power up to 6 metres LOS distance is observed, after that the power remains constant so almost uniform coverage is achieved in this room with an m of 0.17. In the Corridor (fig. H.5) the power does not drop for small d, because once again almost all power is received via reflections against the metal side walls. Here m is only 0.49 for LOS and 0.75 for OBS.

Perhaps the best example of compensation of the inverse square free-space loss by antenna gain is the Hall of the Auditorium building (fig. H.6). For LOS the coverage is nearly uniform with m = 0.1, but for OBS channels the power falls rapidly, especially for distances greater than 10 metres (m is 0.73). In the Vax Room (fig. H.7) a large spread in power samples is observed. Also the increase in difference between LOS and OBS with increasing d is not consistent. This can be completely accredited to random strong reflection against metal objects. This randomness was also observed in the corresponding average power delay of this room (fig. G.7), i.e lower correlation between fitted slope and measured average profile. The constant difference between LOS and OBS in the Amphitheatre (fig H.8) show that free-space loss of reflected rays can also be compensated for by antenna gains. Figure 22 also illustrates this.

A comparison of frequency differences (fig. H.1,H.13 and H.4,H.14) in the Reception Room and the Computer Room show that the power gains are 3 dB higher for the 41-43 GHz measurements, but power decay rates are the same for both frequency bands. This complies with formula (21) which predicts an average increase in power gain of 20*log(58 GHz/42 GHz) = 2.8 dB at 41-43 GHz. The observed difference corroborates the integrity of the measured data. Slight differences in behaviour for a particular measurement positions for LOS channels can be attributed to non-ideal omnidirectionality of the biconical horn antennas. The different setups with circular horns in the Reception Room and Computer Room remain to be discussed (fig. H.11-H.13).

The setup with a corner circular horn base station in the Reception Room (fig. H.11) has a large spread in power versus distance. The LOS path is very dominant for this setup. The corner setup is therefore not to be preferred over a central omni-omni setup from a coverage point of view, although an average increase of 5 dB in power is observed for LOS channels, due to the larger beamwidth of the circular horn. The setup with a circular horn on the remote (fig. H.12) has a much smaller spread in samples due to remote 'pointing' at every position. The channels

with a directional remote are extremely dependent on a line-of-sight connection. For the corner setup in the Computer Room (fig. H.10) the same can be said as for the Reception Room, except that the highly reflective walls reduce LOS dominance and increase average received power.
The LOS dominance increases with room dimensions. This implies that for radio coverage the system performance will strongly depend on a good LOS path for large offices. The same conclusion can be drawn for small rooms with low reflective walls.

Comparison of the different setups in the two rooms lead to the following conclusions regarding radio coverage:

It appears that for both rooms the central omnidirectional biconical horn base station high position, in combination with an omnidirectional remote, yields the most uniform coverage and least line-of-sight dependency. The setup with a low central omnidirectional base station in the Computer Room would appear favourable for increased total power gain, but the setup has a larger LOS dependency than the central high base station.

Tharek and McGeehan [12] report higher signal power levels with a high central omni base station as opposed to a low base station. Better signal coverage, even with no LOS at certain positions, was reported with a high central base station. Their antennas had a 7 dB gain, 20° beamwidth and were circularly polarized. These researchers also advise a high central omnidirectional base station and an omnidirectional remote. Radio coverage is, however, not the only parameter which determines system performance. Time delay spread statistics in combination with radio coverage should give a better impression about which setup gives best performance. The measured power decay rates m are much smaller than anything reported in literature.

7.3 Transmission Measurements

In the Corridor a transmission propagation experiment was performed by closing the swivelling glass doors between remote and base station at position number 4 (the coordinates are given in F.1). The total power dropped only by 4.8 dB and the shape of the impulse response hardly changed at all. The only changes are that the LOS ray, and reflections at t = 100 ns from one end wall, are suppressed. Time delay spread just increased by 3.6 ns from 64.2 to 67.8 ns. The two profiles are drawn in figures 23 and 24. The propagation experiment shows that mm-wave energy could leak through windows very well. Leakage through concrete walls is, however, very small. To check this assumption a transmission experiment was performed at the Lecture Room. Two profiles, one with the remote inside the Lecture Room at position 3 (see F.7 for coordinates) and the other with the remote outside the room are drawn in fig. 25 and 26. These figures show actual measured power levels, i.e. no normalization. The remote trolley was driven outside the room and the door was closed as far as possible. The received signal power barely

superseded the receiver noise floor. The total multipath power G was -116 dB for this measurement, while inside the Lecture Room received power exceeded -80 dB. In [3] a transmission attenuation of 3-7 dB at 60 GHz through doubly-glazed windows is reported. Transmission experiments described in [12] report a 7 dB loss through wooden doors and a 27 dB loss through a concrete wall at 60 GHz. These figures corroborate our measurement results. Figure 26, incidently, clearly demonstrates that the system noise floor does not exceed -120 dB.

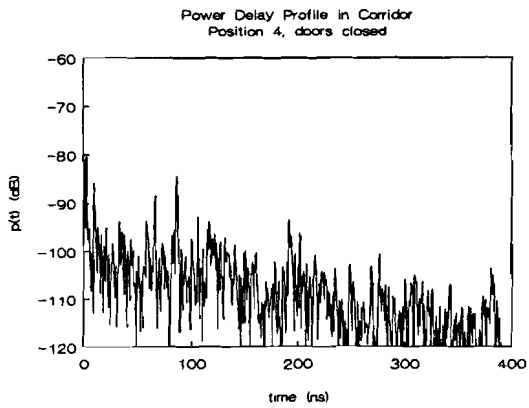

Figure 23: PDP Corridor pos. 4, Doors Closed

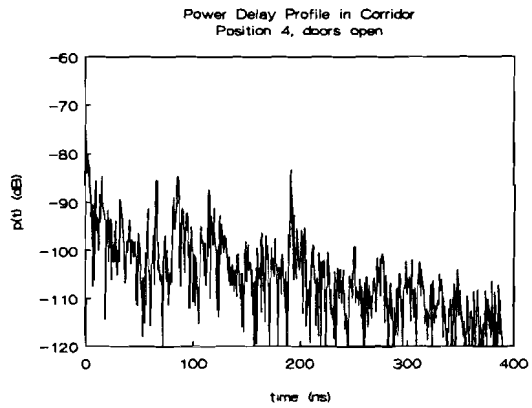

Figure 24: PDP Corridor pos. 4, Doors Open

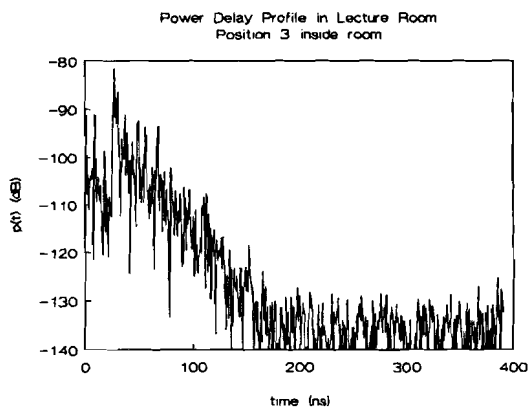

Figure 25: PDP Lecture Room position 3

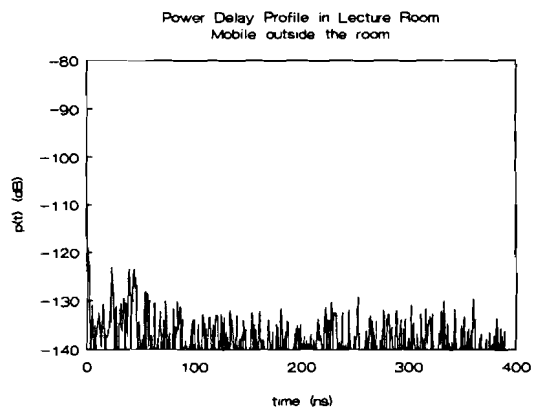

Figure 26: PDP Lecture Room Mobile Outside Room

7.4 Time Delay Spread σ Statistics

So far the power delay profiles and radio coverage in the indoor environments measured at the EUT have been discussed. It has been shown that with high gain omnidirectional antennas a uniform spatial channel behaviour can be achieved. A crucial parameter of wideband multipath fading channels is the time delay spread as defined in chapter 2. It was already mentioned that the delay spread causes error

rates in digital communications because of Inter Symbol Interference. The errors are irreducible because they cannot simply be reduced by an increase of signal power. Before measured statistics are presented let us look at the delay spreads reported in the literature. A lot of research effort is concentrated up to 2.5 GHz because these frequencies are used for portable cellular telephones. In [5] values between 20 and 50 ns are reported using a measurement frequency band around 1.5 GHz. Omnidirectional discone antennas were used at 2 m above the floor. The measurement area however was much larger, a whole building floor was covered. In [3] spreads of 20-150 ns are presented, using dipole antennas at 1.5 m height on large manufacturing and laboratory floors. The central measurement frequency was 910 MHz. In [7] values of 10 to 40 ns are reported for an office floor, also using dipole antennas. These measurements were conducted in a 200 MHz band around 1 GHz. For open plan factory floors values of 25 to 150 ns are reported in [4] with a measurement frequency band around 1.3 GHz. In [6] values of 10-40 ns are reported at 60 GHz in medium sized offices and a narrow corridor, using bi-reflector omnidirectional antennas at 1.5 m height. Values of σ were very site dependent.

An indication of the achievable symbolrates without equalization is given by formula (17). A 50 ns delay spread limits the maximal symbolrate to 4 Ms/s, at σ = 150 ns r_{max} is only 1.33 Ms/s. Remarkable is that spread values in the mm-wave band are comparable to those measured at 1 GHz even though indoor environments considered in the mm-wave band are much smaller than those at 1 GHz (one room only at mm-wave frequencies). This is caused by higher signal power over shorter propagation distances in one office. If a whole building floor is considered the propagation delays will be much longer, but power levels in the reflected rays will be much less, even though the free-space loss decreases with frequency. For the calculation of the time delay spread each reflected ray is weighted by its time delay. Therefore strong rays at shorter time delays could yield the same time delay spreads as weak rays which have long time delays.

Our results agree with values reported in the literature, although a great diversity is measured in the eight rooms. Values between 13 ns and 98 ns have been found. In chapter 4 it was shown that with 801 data samples in a 2 GHz bandwidth a aliasing-free range of exactly 400 ns is achieved. Because of the convolution with a window function the line-of-sight pulse (other pulses also) consists of more than one data point. Because the maximum of this pulse is located at t = 0 ns a few data points of this first ray will have negative time values. Due to aliasing these values fold back to values at 400 ns. Although these data points do contribute to the total signal power they should not be used for calculation of the delay spread, because for this parameter each ray is weighed with its delay time. Aliasing therefore yields a virtual ray at 400 ns. To ensure that σ is not calculated incorrectly only time values up to 390 ns are considered. In the previous section it was shown that obstruction of the direct path could change the radio coverage considerably in some rooms while in other rooms the changes were insignificant. The change in σ due to obstruction is therefore also evaluated. The power gain, naturally, decreases for the

OBS channels. The time delay spread does not necessarily have to deteriorate for OBS channels, because formula (15) in chapter 2 predicts an increase in average time delay. The average time delay can increase at OBS because the LOS ray is weighed with a zero time value in the numerator of (15). In figure 27 and 28 the survival functions for sigmas in the eight rooms are drawn. These two figures represent the 60 GHz LOS measurement series with two omnidirectional antennas and a high central base station. For characterisation of time delay spreads in a room with a single time delay spread value an average time delay spread is defined. This average spread is calculated using the average power delay profile, defined in section 7.1, in accordance with the definitions of average parameters suggested by the COST 231 group. This average time delay spread is not equal to, but very similar to the average of the individual time delay spread values.

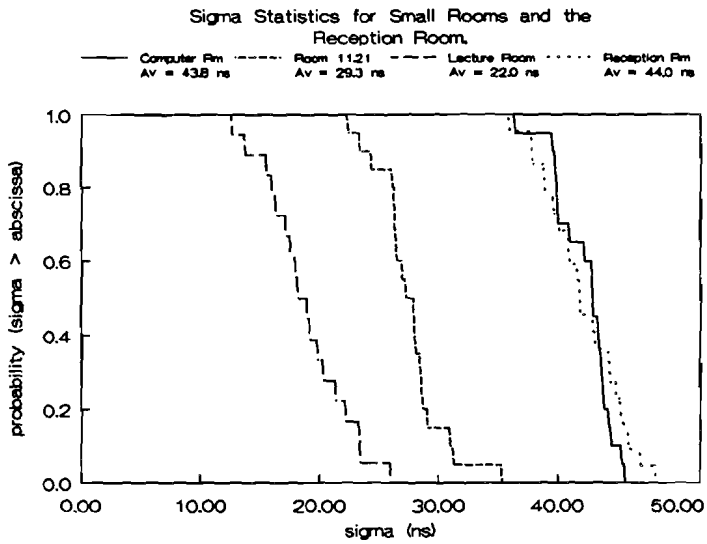

Figure 27: Sigma Statistics in Rectangular Rooms

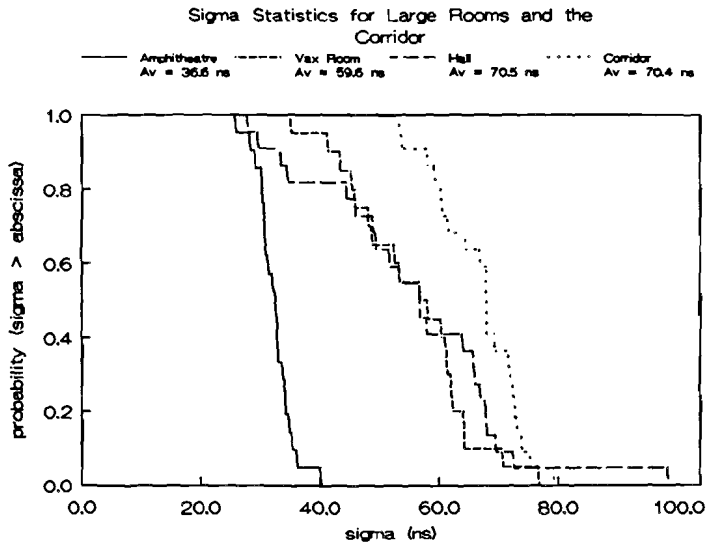

Figure 28: Sigma Statistics in Large Rooms

Looking at figure 27 it is clear that the time delay spread increases with the reflectivity of the walls. This incidently, is also true for obstructed channels. Time delay spread values in the Computer Room are even larger than in the Amphitheatre. So an increase in room size does not automatically imply an increase of σ. The spread in time delay is very large in the Vax Room and the Hall compared to the Amphitheatre. The metal objects in the Vax Room do not only cause a large spread in power gains and power delay profiles, but also in time delay spread values. For the smaller rooms the standard deviation of the sigma values is less than 3.5 ns. For the Vax Room this is 10.4 ns and for the Hall 16.5 ns.

In evaluating the radio coverage the power versus distance was looked at. It would be interesting to see how the delay spread values behave at increasing LOS distances. To this end the 14 measured σ versus distance charts are drawn in figures I.1-I.14. From these figures it is clear that the time delay spreads remain constant for increasing distances. This is a very favourable channel characteristic, for it implies that the same bitrates can be achieved everywhere in a particular room (fair access!). An exception is formed by the Hall (fig. I.6) where LOS delay spreads decrease as distances increase. The importance of the direct path becomes apparent if the difference between LOS and OBS is looked at. LOS blockage causes the time delay spread values to increase drastically for large separation distances, although they stay below 70 ns. At small distances blockage causes the σ's to decrease and for large distances an increase of σ is observed. Random differences between OBS and LOS occur in the Vax Room (fig. I.7).

Note the small difference between LOS and OBS (fig. I.1) in the Computer Room and compare this to figure H.1. Time delay spread in this room does not depend on the direct path, nor does the radio coverage. So metal walls give a very uniform indoor radio channel behaviour! In the Reception Room (fig. I.4) a small decrease in σ for OBS channels is observed for all positions, while in figure I.9 an increase in σ is observed for these channels. This indicates that a channel deterioration, or improvement, due to blockage of the LOS ray is difficult to predict.
In figures 29 and 30 the time delay spreads of the different setups in the Computer Room and the Reception Room are depicted for LOS situations.

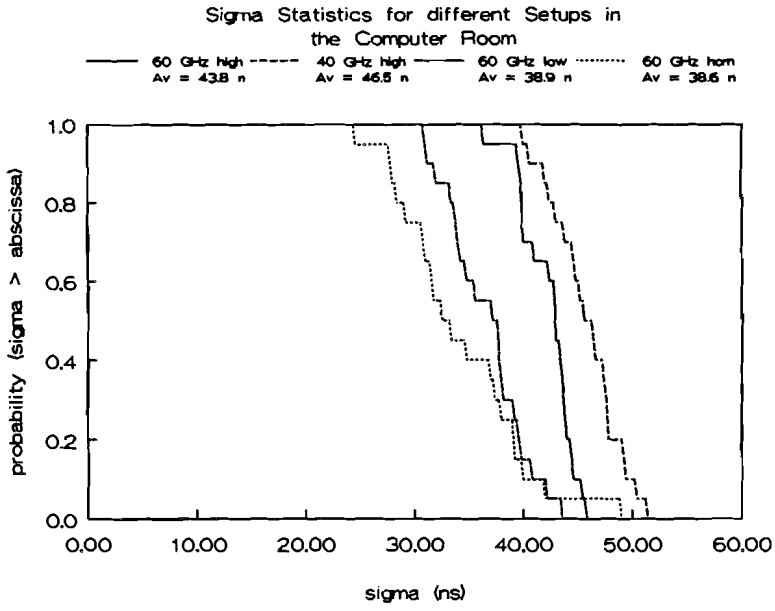

Figure 29: Sigma Statistics in the Computer Room

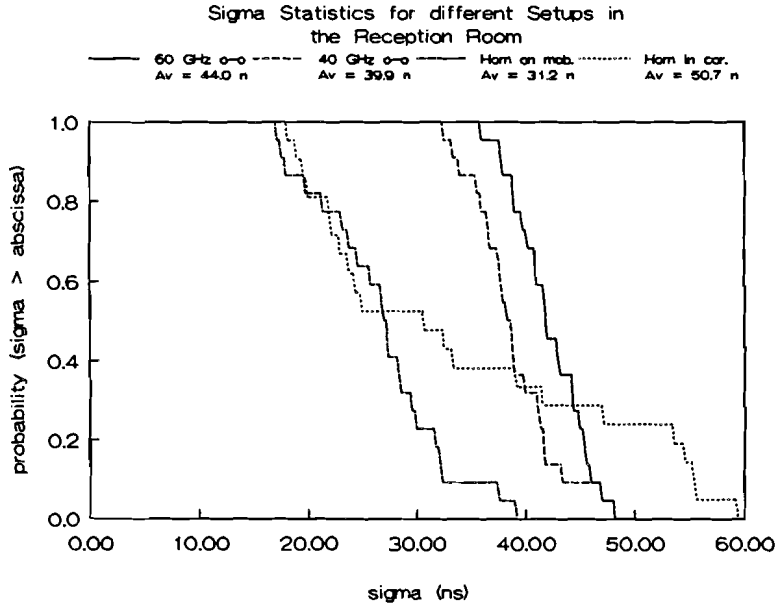

Figure 30: Sigma Statistics in the Reception Room

Slight differences occur at 41-43 GHz and 57-59 GHz in the Computer Room. Time delay spreads are larger at lower frequencies, but the standard deviation is nearly the same: 2.4 and 3.2 ns. The increase in sigmas at 41-43 GHz could be caused by a decrease in atmospheric attenuation and free-space loss (reflected rays will be slightly stronger), however the measurement results of the Reception Room contradict this. Here lower spreads are measured at 41-43 GHz. Reflection measurements of glass- and wooden walls in the Reception Room show that the reflectivity of glass

increases with decreasing frequency and that of wood decreases. If the assumption is made that the reflection coefficient of metal does not change in the mm-wave frequency band then the increase at 41-43 GHz for the Computer Room is plausible and so is the decrease for the Reception Room. The measured reflection coefficients will be presented in chapter 9. The corresponding graphs of sigma versus distance are drawn in figures I.1,I.4,I.13 and I.14.

Comparison of different setups in the Computer Room:
The setup with a low central base station (fig. I.9) gives a 5 ns improvement in average σ, for line-of-sight, compared to a high central base station. For OBS this advantage is reduced to only 3 ns. All sigmas increase for OBS channels in this environment. As far as time delay spread is concerned the low base station setup does not improve channel behaviour much. The only improvement for this setup is therefore the higher power gain due to the elevation gain of the biconical horns. The setup with a circular horn in a corner (fig. I.10) also has a 5 ns improvement in average σ for LOS channels. However, the standard deviation of the time delay spread samples is much larger: 5.9 ns in stead of 2.4 ns. The deviation is the same for OBS channels in this setup, no significant deterioration of sigma is observed for OBS. The 5 ns advantage does not weigh up to the uniform time delay spread achieved with an omni-omni setup.

Comparison of the three 57-59 GHz series in the Reception Room:
The setup with a circular horn in a corner (fig. I.11) shows very diverse spatial channel behaviour in time delay spread with a corresponding large standard deviation of 14.5 ns and 10.4 ns for LOS and OBS respectively. For the omni-omni setup these values are only 3.3 and 3.2 ns. For certain positions a significant improvement in σ is achieved, values fall to 20 ns, while in other locations values up to 60 ns occur. The setup with a circular horn on the remote (fig. I.12) gives an improvement of 13 ns in average time delay spread with a standard deviation of only 5.9 ns. However, figure I.12 clearly demonstrates that this advantage is lost if obstruction of the line-of-sight path occurs.

7.5 Influence of Noise and Profile Chopping on Time Delay Spread

The time delay statistics presented in the previous section is calculated using all data points from 0 to 390 ns. The influence of noise and profile chopping at 400 ns excess delay on time delay spread calculation can be evaluated by reducing the maximum time up to which data points are included in the calculation of (15). In figures 31 and 32 the average time delay spread as a function of maximal time span is drawn for the 8 series at 57-59 GHz with a high central omnidirectional base station and an omnidirectional remote. These two figures clearly demonstrate that the average time delay spread does not increase very much once the average power delay profile has dropped by 40 dB. This is also true for the other measurement series. If noise did play an important role in the time delay spread values the calculated σ should drop sharply if the maximal time is reduced in all series. The

corresponding average power delay profiles are drawn in figures G.1-G.8. In section 7.1 it was mentioned that for the Corridor the average power delay profile has not yet reached the noise floor at t = 400 ns, and that this chopping causes a considerable error in σ. This is also shown by figure 32, the average time delay spread drops immediately if the time span is reduced.

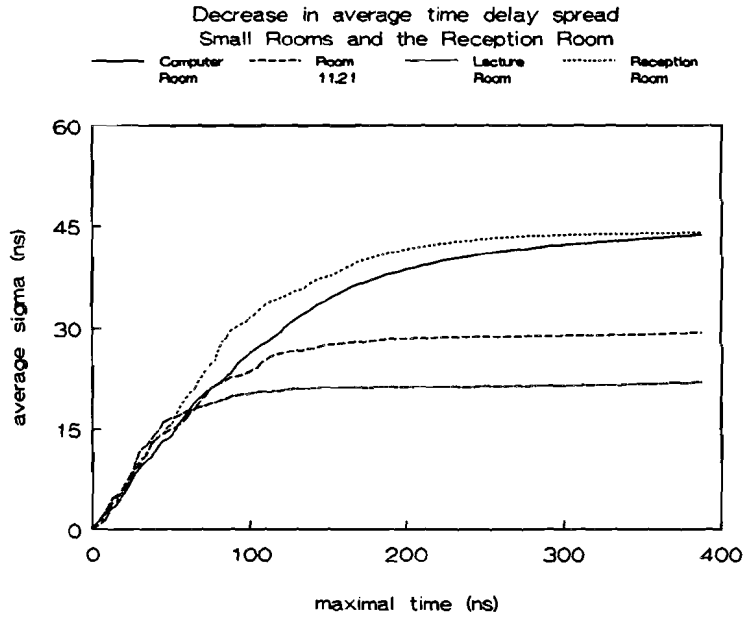

Figure 31: σ versus Maximal Time for Rectangular Rooms

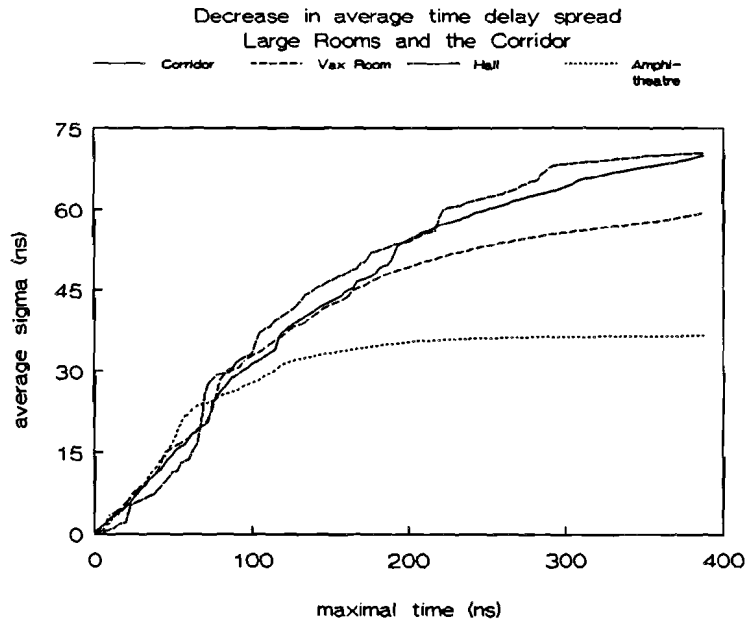

Figure 32: σ versus Maximal Time for Large Rooms

7.6 Conclusions regarding Setups and Frequency

Measurements performed at the EUT show that for indoor radio communications at mm-wave frequencies a setup with an omnidirectional remote at table height and an omnidirectional base station near the ceiling of an office is most favourable for not only uniform signal coverage, but also for uniform time delay spread behaviour. Large spread in spatial channel behaviour occurs with a directional base station in a corner. This spread can be reduced if a circular horn with a larger beamwidth than 27° is used. A larger beamwidth would give a more uniform illumination of the room. An 'aimed' directional remote and a central omnidirectional base station give a more uniform channel performance. A reduction of time delay spread and higher power gain can be achieved with this setup, but these advantages are lost if the line-of-sight path is blocked. A disadvantage is also that the remote has to be manually pointed towards the base station, this is not very practical in an office where, for example, lap-top computers are used.

Channel behaviour is very similar in the two frequency bands considered, even though atmospheric attenuation and reflection coefficients, glass in particular, change considerably. The low standard deviation of σ indicates that a particular room can be characterized by a single average time delay spread. These values are added in figures 29 and 30. Measurements indicate that the delay spread is 20-40 ns for small rooms and 40-70 ns for large rooms. Substantial deviations from the averages could occur, especially if there are many metal scattering objects in the room. The Vax Room is probably the best example of a typical office environment. Worst case time delay spread in this room is 80 ns. According to (17) a symbolrate of 2.5 Ms/s can be achieved without equalization for this room at mm-wave frequencies. For a B-ISDN network at mm-wave frequencies channel equalization is unavoidable, although many low speed applications like telephones and facsimiles will not require equalization for acceptable biterror rates.

On a number of occasions the remote was displaced a few centimetres. The profiles did **not** change significantly, which suggests that individual rays consist of one propagation path only. This assumption is further justified because single paths could be blocked with a small piece of absorber. Ray individuality will be used in the statistical modelling of rays in chapter eight.

8 Statistical Modelling of Indoor Radio Channels

In chapter 7 the parameters which characterize the indoor multipath channel have been presented. The measured propagation characteristics were very similar for different positions in one room, but differed considerably from room to room. Up to this point the statistics of individual paths have not yet been considered. The parameters considered in chapter 7 should give a good estimate of the possible indoor radio system performance; yet the objective of the study in this chapter is to find a statistical model for the indoor radio channels.

What is a statistical model of a multipath channel?

A statistical model predicts the amplitude, phase and time of arrival of the reflected rays via probability distributions. With these distributions a multipath profile can be completely characterized. The distribution functions are derived from empirical data.

Why should we concern ourselves with statistics if the channels can be described with a deterministic model like the one described in chapter 3?

First of all the number of possible reflecting surfaces within one room can be very large; just think of the number of objects which are present in, for example, a common office or stock exchange floor. It is difficult to incorporate a large number of objects in a deterministic model, for calculations will become very time-consuming, especially if diffracted rays are included in the model. In addition to this the positions (relative to the transmitting and receiving antennas) of the reflecting objects like walls, chairs, tables, etc., change as the remote is moved around in a room. So the channel parameters, like the time delay spread for instance, will change with remote position, simply because the set of path strengths α_n and corresponding arrival times τ_n also changes with remote displacement. For a good characterisation of a room with many objects a large number of simulations will have to be performed.

The second reason why a statistical model is desirable is that it is more practical to use than a deterministic model. This is especially true if system performance is to be evaluated through outage probabilities. The calculation of an outage probability requires the generation of numerous individual channel responses. A major drawback of a deterministic ray tracing model is however, that it requires accurate scattering parameters of wall, floor, ceiling and other common objects of a particular indoor environment. It is not hard to imagine that these parameters could differ considerably from environment to environment; just look at the diversity of measurement results reported in chapter 7. Extensive measurements of scattering parameters at mm-wave frequencies have not yet been reported in literature.

In chapter 9 some comparisons of measurements with simulations will be presented. They will show that for some rooms a good impression of the radio propagation characteristics can be obtained using Geometrical Optics. In other rooms however the resemblance goes askew. This is probably caused by the limited number and accuracy of the reflection coefficient measurements performed. Discrepancies between theory and practice could also be caused by the limited number of reflections (4 times) considered in the model.

Several widely known statistical models for multipath radio channels have been reported in the literature:

1) A continuous model: The Gaussian Wide-Sense Stationary Uncorrelated Scattering (GWSSUS) model [17];
2) Discrete models which are divided into two different classifications:
   a) The Correlated Scattering Discrete Model [18],
   b) The Uncorrelated Scattering Discrete Model [5].

The continuous model corresponds to a situation were any element of the power delay profile actually consists of a number of individual rays which add up within the measurement time resolution. The Gaussian process is justified by using the central limit theory for a large number of ray-components. This justification holds if there is no dominant component. The distribution of the envelopes of the rays is Rayleigh, so the model is also sometimes referred to as a continuous Rayleigh model. In the correlated scattering model the probability of an event, i.e. arrival of a ray at delay time t, depends on whether or not another ray has arrived in the interval t-Δt. This is modelled as a two-rate Poisson process. Ray amplitudes are found to be log-normally distributed. Model 2b assumes independent rays. Observations during measurements at the EUT support the last model. Individual rays could be detected while other rays were not noticeably influenced.

For the calculation of the time delay spread and power gain all data points were used. For a discrete statistical model some form of data reduction has to be done, in order to extract the time of arrival and amplitude of single rays in a profile. The statistical modelling will show that even though the average power delay profiles change considerably, path statistics are very similar in all rooms.

8.1 Path Definition for Statistical Modelling

The first step towards statistical modelling is a filtering process of the 801 data points per power delay profile, so the time of arrival and amplitudes of the discrete reflected rays can be detected. Not all data samples can be considered as being actual paths, for the profiles also contain noise and side-lobes of the window function (26). Also a ray will span more than one data sample, while in a statistical model a path is to be modelled as a delta pulse according to (9). The search for individual propagation paths is therefore a search for local maxima in the power

delay profiles. These local maxima are determined as follows:
The first data point of each profile is per definition a path, because all measured profiles were time-aligned so that the maximum of the line-of-sight ray is located at zero seconds delay. From the second point onwards the data is looked at through a three-point 'window', i.e. at a particular delay time t only three consecutive data points are looked at. If, and only if, the central point is greater than both its neighbours the point is declared a possible path. Next the 'window' is shifted by 1 position and the process is repeated. To ensure that noise and pulse side-lobes (maximum pulse side-lobe level is -44 dB, see section 4.4) are excluded from being modelled as genuine propagation paths, only data values which exceed a certain threshold are candidate for a propagation path. This threshold value is chosen to be equal to the dynamic range of the measurement system (40 dB signal-to-noise ratio). So data values which are more than 40 dB below the maximum of a profile are excluded from path modelling. Figure 25 suggests that a 40 dB threshold might be pessimistic but with this threshold path integrity is ensured.

Three data points are sufficient to detect a path. A measurement resolution of 1 ns implies that two equal paths which are 1 ns apart can be distinguished. A 1 ns time interval is spanned by three data points (data spacing is 0.5 ns). If the 'window' used for finding local maxima spans more than three points, too much data is lost, and less rays will be detected. The measurement resolution is not used completely in this case. Using three data points automatically implies that the minimal discernable interarrival time (this is the time between two consecutive paths) is 1 ns.

Of course this method of finding individual rays in a power delay profile has its limitations. Weak rays which are dominated by a strong neighbouring rays will not be detected. Consecutive paths which have interarrival times smaller than 0.5 ns will be detected as one ray, because one path will span at least 1 ns. The loss of weak rays will especially influence the interarrival distributions. The problem of not detecting weak rays near strong ones is, however, a common problem. It is encountered no matter what search algorithm or measurement resolution is used.

Statistics presented in this chapter concern statistics per measurement series. Only excess delays up to 390 ns are considered in the statistical model. The reason for this was already described in section 7.4. By looking for individual rays the ray arrivals are modelled as a discrete process.

8.2 Distribution of Propagation Path Amplitudes

Using the search algorithm described in the previous section the spatial amplitude distribution at an excess delay time t is determined empirically. A major assumption in generating these distributions is that path amplitude statistics are considered to be time-independent, as is the case in a stationary process. This implies that all rays have to be independent. The randomly chosen measurement positions within a single room justify this independency. Separation distances between measurement

positions are also typically much larger than the measurement wavelength (> 200 λ at 41 GHz). The statistics for path amplitudes concern **spatial** statistics in a particular room, i.e. with the distribution function the probability of receiving a ray with a certain strength at an excess delay can be calculated for randomly chosen positions in a room. The path amplitude distribution represents the cross-section at a time t of the ensemble of delay profiles in a single measurement series. Because rays are assumed to be independent, they are pooled into one data base.
The fast decay of the autocorrelation of single power delay profiles also shows that rays are independent. The power delay profile-length is limited to 400 ns, so the autocorrelation of a profile will automatically decrease for $\tau \neq 0$. The profiles however, have very small values for large t, so the rapid decay of the auto-correlation is not caused by the bounded profile. In addition to this correlated rays should give a high autocorrelation for very small τ. The theoretical autocorrelation function of a power delay profile is defined as:

$$q(\tau) = \int_{-\infty}^{\infty} p(t).p(t+\tau)dt \ . \tag{48}$$

The integral in (48) is calculated by summation of the discrete data points. Actual integral limits are of course ± 400 ns. In figure 33 a typical autocorrelation function is drawn for positive τ. The autocorrelation is normalized to 1 for τ = 0 seconds. The autocorrelation $q(t)$ is an even function by definition.

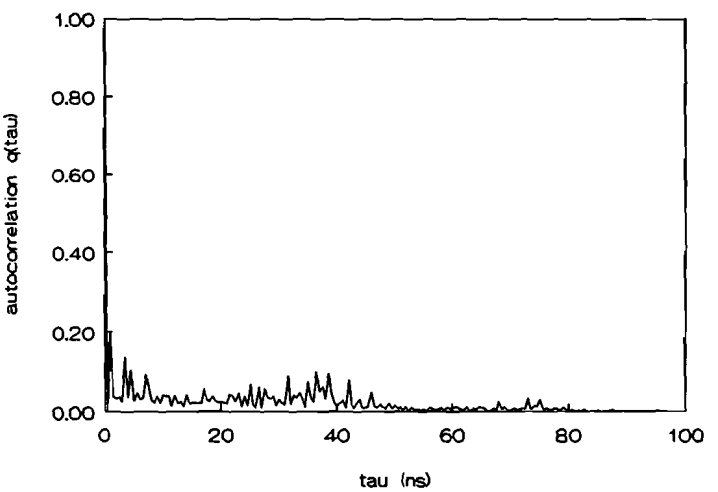

Figure 33: Typical Autocorrelation Function

How are the empirical distributions generated?
The profiles are scanned for individual propagation paths with the algorithm described in section 8.1. Non-path data values are zeroed, so detected rays are modelled as a single data value (delta-pulse). At every delay $t = i.0.5$ ns, where i = 0,1,2,3,... the average ray power for a series is determined. The third step is that every detected ray is normalized by the appropriate power average. All normalized

ray powers are pooled into a data base. From this data base a frequency histogram can be determined. The Rayleigh distribution, as will be shown, fits our data very well. This should not be confused with Rayleigh fading. Rayleigh fading occurs if a continuous wave is transmitted by a moving remote. Interference of dominant multipath components causes fading. The time statistics of this narrow band process is a Rayleigh distribution. Our remote and channel are stationary during a measurement sweep.
For ease of notation the path powers α_n^2 (12) are modelled as time dependent functions, i.e

$$\alpha_n^2 = \alpha^2(t) , \tag{49}$$

with t = 0,0.5,1,... nanoseconds.
The survival function (= 1- cum. pdf) determined from the data base fits a unity mean exponential cumulative distribution very well (this will be shown in figures (34) and (35)) for nearly all series, i.e

$$P(\alpha^2(t)/\overline{\alpha^2(t)} > X) = e^{-X} . \tag{50}$$

The path powers are therefore exponentially distributed, i.e.

$$f(\alpha^2(t)) = \frac{1}{\overline{\alpha^2(t)}} e^{-\frac{\alpha^2(t)}{\overline{\alpha^2(t)}}} . \tag{51}$$

This is equivalent to a Rayleigh distribution of the ray amplitudes.
The Rayleigh probability density distribution is defined as

$$f(\alpha(t)) = \frac{2}{\beta}.\alpha(t).e^{-\frac{\alpha^2(t)}{\beta}} , \tag{52}$$

The normalization parameter β equals

$$\beta = \overline{\alpha^2(t)} . \tag{53}$$

The parameter β is therefore equal to the average ray power of a measurement series at a time t. This is equal to the average power delay profile as defined in section 7.1. The average power delay profile was modelled to decay exponentially, so the power slopes, which were presented in appendix 2, can therefore be used to calculate the parameter β. Remember that the deviations from the linear slopes, for small t, of the average profiles, drawn in figures G.1-G.14, are not included in the model because it was caused by antenna elevation directivities.

The assumption that a Rayleigh distribution describes the measured path statistics very well must be verified with some form of goodness-of-fit test. A common test used for testing the validity of a hypothetical distribution is the chi-squared test. For this test the empirical data is divided into a number of randomly chosen classes. A

measure of the discrepancy between the empirical and theoretical distributions is defined as

$$\chi_0^2 = \sum_{j=1}^{l} \frac{(f_j - F_j)^2}{F_j} , \tag{54}$$

where l denotes the number of classes. In (54) f_j and F_j denote the observed and expected frequency in class j. For large samples, i.e. large numbers of data values, χ_0^2 tends to a chi-squared distribution, regardless of the hypothetical distribution. This chi-squared distribution has $k = l\text{-}r\text{-}1$ degrees of freedom, where r is the number of parameters of the hypothetical distribution (1 for Rayleigh).

From the chi-square distribution the probability

$$\xi_0 = P(\chi^2 < \chi_0^2) \tag{55}$$

is calculated. If the significance level ξ_0 is smaller than some value, 95 % or 99 % is common practice, then the hypothesis that the empirical distribution is the same as the theoretical distribution is rejected.

For only 2 of the 14 measurement series the hypothetical Rayleigh distribution is rejected if a significance level of 95 % is used as a selection criterium. The two series are the 41-43 GHz and 57-59 GHz omni-omni series with a high central base station in the Computer Room. The significance level is 89 % for both these series. In figures 34 en 35 two empirical survival functions are drawn, representing the best and worst fits to the unity mean exponential function. The dotted lines are the empirical distributions, the solid lines represent exp(-X).

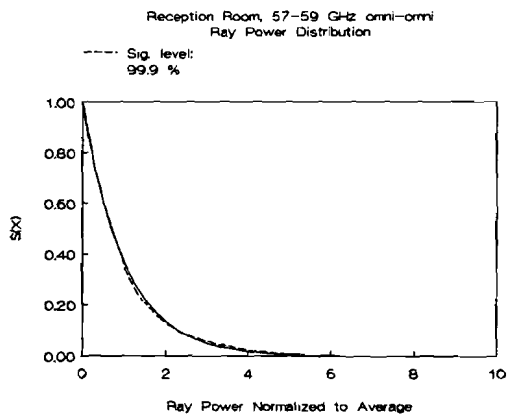

Figure 34: Best Fit of Ray Power Distribution

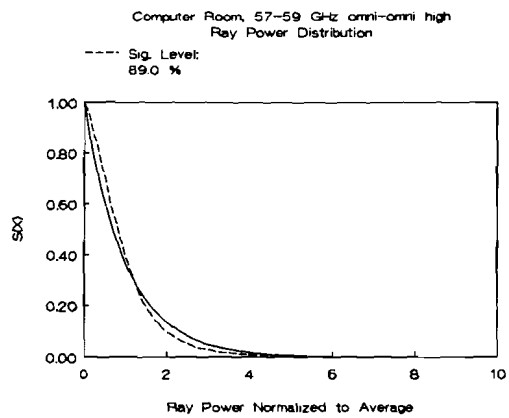

Figure 35: Worst Fit of Ray Power Distribution

The value of the normalization parameter of the Rayleigh distribution can be calculated using the average decay slopes according to

$$\overline{\alpha^2(t)} = \overline{\alpha^2(0)}.e^{-\frac{t}{\gamma}}, \tag{56}$$

where $\alpha^2(0)$ is the power of the line-of-sight ray. It can be calculated using the power distance formula (21). Line-of-sight dominance can be modelled by offsetting this ray, by for example 10-15 dB, above the value predicted by (56). The exponential power-time decay rate γ is calculated from the slopes B in formula (45) according to

$$\gamma = -\frac{10}{B.\ln(10)}. \tag{57}$$

The measured values of γ are tabulated in table 2. In this table the significance level of the chi-square goodness-of-fit test is included.

Table 2: Power-Time Decay Exponent γ for all Series

Measurement series	γ (ns)	Sig. Level
Reception Room 60 GHz	35	99.99 %
Computer Room 60 GHz base station at 2.75 m	47	89.0 %
Vax Room	52	98.9 %
Hall	60	98.3 %
Corridor	75	98.1 %
Amphitheatre	31	99.9 %
Room 11.21	25	99.6 %
Lecture Room	16	99.6 %
Reception Room 40 GHz	35	99.99 %
Reception Room circular horn on remote	40	99.3 %
Reception Room circular horn in corner	44	97.0 %
Computer Room 40 Ghz	47	89.7 %
Computer Room 60 GHz base station at 1.60 m	49	99.5 %
Computer Room 60 GHz circular horn in corner	41	99.9 %

Note the small differences between 41-43 GHz and 57-59 GHz in the Computer and Reception Room. Both γ **and** the significance level are the same.

How do the values in table 2 compare to the decay, measured by Saleh and Valenzuela [5], in the UHF region? These researchers modelled their profiles by two exponential decay rates, because they found that rays arrive in clusters. The leading peaks of these clusters decay exponentially with time and so do rays within a single cluster. The clustering, they conclude, is related to the building superstructure. This means that a number rays which arrive at the receiver with approximately the same delay, come from the same direction (propagation through the same walls of a room for example). These rays will form a cluster. The measurements in [5] covered a whole building floor.

For indoor radio communications at mm-wave frequencies the signal coverage is limited to one room, therefore the individual clusters suggested here are not observed. If a comparison should be made with their model then all our resolved rays belong to the same, first, cluster. In [5] a single value for γ of 20 ns is reported. This value does fall within the range measured at Eindhoven, our values vary from 16 to 75 ns. Larger γ values indicate a slower decay of power. The diversity of values in table 2 shows that a single power time decay value is inadequate to describe all of the indoor radio channels at mm-wave frequencies. Other researchers [18] model the rays to be correlated, with log-normally distributed amplitudes. This correlation of rays is attributed to clustering.

So far it has been shown that the amplitude of a ray at an excess delay time t can be calculated for a random position within a room using the Rayleigh probability distribution. In other words: the rays with identical delay times in a single measurement series (cross-section at delay t of the ensemble of profiles) have an amplitude which is Rayleigh distributed. The phases of these rays should be uniformly distributed over $[0,2\pi]$, the ray process then corresponds to a complex Gaussian process. This assumption was checked for all series and found to be true. An example of a typical phase distribution is drawn in figure 36. The straight line corresponds to a uniform distribution over [-180°,180°].

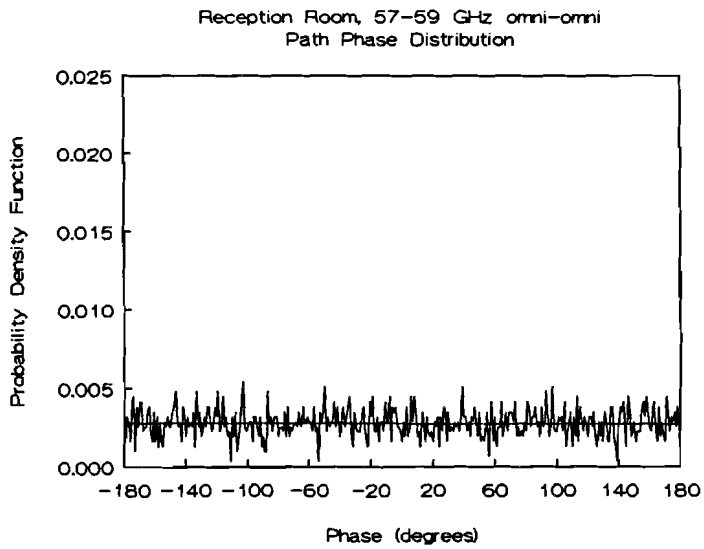

Figure 36 : Typical Path Phase Distribution

8.3 Ray Interarrival Time Distribution

The last parameter necessary for a statistical description of indoor multipath radio channels is the probability of a ray arrival at an excess delay time *t*. Equivalently it is also sufficient if the statistical distribution of the time between consecutive paths, the interarrival time, is known. Because the data points of the power delay paths are equally spaced at 0.5 ns intervals, the time of arrival of a detected ray is also a multiple of 0.5 ns, i.e

$$\Delta\tau = \tau_{n+1} - \tau_n = i.0.5\ ns\ ,\ where\ i = 0,1,2,.... \qquad (58)$$

The 'three point' path search algorithm automatically implies that interarrival times of 0.5 ns (two consecutive data points) cannot be detected. To exclude noise a minimal threshold of -40 dB is used. The interarrival time statistics are also considered per measurement series. An example of an empirical probability density function is drawn in figure 37. Empirical means that the probability of an interarrival time $\Delta\tau$ is simply the quotient of the number of times this inter-arrival time occurred and the total number of interarrival times found in a particular measurement series. Not included in figure 37 are incidental high values (up to 100 ns) found, for these values are a result of the threshold. Because the area under a probability density function must equal 1, the height of a single bar in figure 37 is adjusted in such a way that:

Height * Width = Probability * Unit Area.

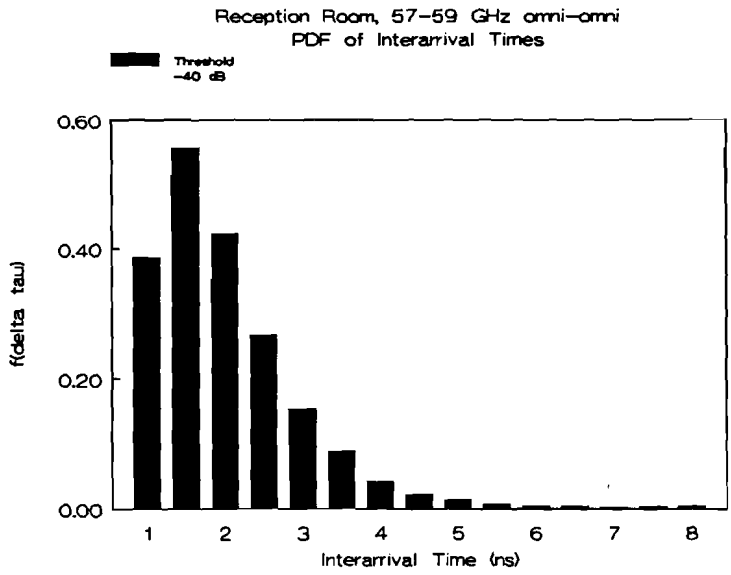

Figure 37: Typical Interarrival Time Frequency Histogram

The shape of the histogram drawn in figure 37 is common to all series, and as will be shown, for different threshold values.

Because the probability of an interarrival time of 1 ns is smaller than the probability at 1.5 ns, the shape of the empirical distribution suggests that the interarrival time distribution should generally follow a function as follows

$$f(x) = Ax^p e^{-\beta x^q} . \tag{59}$$

However, keep in mind that 1 ns is the measurement resolution. In [21,22], where indoor radio channels in manufacturing environments have been researched, an interarrival time distribution with the same shape as ours is reported. These radio channels are modelled as uncorrelated rays with log-normal amplitudes, and a Weibull interarrival time distribution. This distribution approaches zero for small $\Delta\tau$. Their measured interarrival distribution also started to decrease for interarrival times smaller than the measurement setup resolution.

Because the distribution drops for interarrival times which are smaller than or equal to the measurement resolution, it is believed that this drop is caused by domination of weak rays by neighbouring strong rays. The weak rays will not be detected, thus resulting in a lower probability for small interarrival times. For an uncorrelated scattering model an interarrival distribution according to (59) would predict that rays could not overlap. There is really no conceivable reason why pulse overlap could not occur for independent rays. That this overlap cannot be detected is an entirely different matter! So we believe that an interarrival distribution with a shape according to (59) does not depict reality.

For many situations were random arrivals are being considered, like customer arrivals at a supermarket check-out for example, it is found that the Poisson distribution provides a good description of the random arrival pattern. Random arrival means that each occurrence is independent and cannot be predicted exactly. Using the Poisson distribution the probability of k arrivals in a time period t equals

$$\begin{aligned} P_k(t) &= Pr(k \text{ arrivals} \in \text{interval } t) \\ &= \frac{e^{-\lambda t}.(\lambda t)^k}{k!}, \quad k = 0,1,2,3,.... \end{aligned} \tag{60}$$

This distribution is equivalent with a time between two consecutive arrivals (interarrival time) of

$$\begin{aligned} f(\Delta t) &= Pr(\tau_{n+1} \mid \tau_n) = \lambda e^{-\lambda(\tau_{n+1}-\tau_n)} \\ &= \lambda e^{-\lambda \Delta t}. \end{aligned} \tag{61}$$

So for a Poisson arrival process the interarrival times follow a negative exponential distribution. The parameter λ is known as the mean arrival rate, and the reciprocal value $1/\lambda$ is the mean time between two consecutive arrivals.

Let us look at the empirical distribution drawn in figure 37 differently. Could the measured interarrival time distribution be approximated by a negative exponential distribution?

This is possible if the data for $\Delta t = 1ns$ is omitted from an exponential fit. The interarrival time distribution does decay exponentially, starting from $\Delta t = 1.5ns$. Because a number of weak rays is missed the total number of resolved rays is left as a parameter which is to be optimized for fitting an exponential distribution. The total number of rays determines the height of the bars in a frequency histogram. If the assumption is made that the ray arrival process is in fact a Poisson process then the following procedure is used for finding the mean ray arrival rate:
First all interarrival values of 1 ns are removed from the data set. Next an exponential function $A_0 \exp(-A_1 t)$ is fitted to the empirical interarrival distribution according to a MMSE criterion. The fit parameter A_1 is equated to the arrival rate λ. The next step is decreasing the heights of the bars in the frequency histograms (actual number of rays is larger than resolved total) until the deviation from (61) is minimal (MMSE). In figures J.1-J.14 the interarrival distributions for the 14 measurement series are drawn, with corresponding exponential fits. Values at 1 ns are included **after** the fit has been made. Three different threshold values: -40, -30 and -20 dB were used for comparison purposes. Increasing the threshold value causes λ to increase for all profiles. This is to be expected for a Poisson ray arrival process.

The interarrival time distributions were subjected to a chi-squared goodness-of-fit test. Unfortunately this test failed to yield significant results. This is mainly caused by the limited set size (1.5, 2.0, 2.5 etc.) of the interarrival data, even though the

total number of values is considerable, typically several thousand values per measurement series. The number of classes for a chi-squared test is therefore too small. This is not the case for the ray amplitudes, for these data values are real continuous variables. However, good correlation coefficients (MMSE) between exponential fit and empirical frequency distributions are found, R is larger than 0.98 for a -40 dB threshold.

The charts drawn in J.1-J.14 show that the exponential decay can still be detected even with a threshold of -20 dB. Deviations from the fits increase with an increase of threshold. Because a significant part of the data is lost if the threshold is increased, a threshold of -40 dB should give the best estimation of the mean arrival rates. In table 3 the mean interarrival times are presented for all series.
The mean arrival times vary from 0.68 to 1.08 ns. An average over all series is 0.85 ns. This is smaller than the 1 ns measurement resolution. The mean interarrival time does not increase dramatically for very large environments. The low value for the Corridor is caused by its narrow structure. Note the increase from 0.88 to 1.08 if the base station is lowered in the Computer Room. For a low base station reflected rays are much stronger due to antenna gains, so more weak rays will be dominated. This results in a larger value for $1/\lambda$.

8.4 Summary of Statistical Model

The statistical model presented in this chapter shows that the impulse response of indoor radio channels at mm-wave frequencies fit very well to the uncorrelated discrete scattering model first suggested by Saleh and Valenzuela [5]. Rays decay exponentially with time. Exponential decay factors vary from 16 to 75 ns. Ray amplitudes at a fixed delay time fit very well to a Rayleigh distribution. A single Poisson arrival rate was used to model the ray arrival times. The mean interarrival times vary from 0.68 to 1.1 ns. On average over all measurement series the mean interarrival time is 0.85 ns. This value is comparable to the measurement resolution. In [5] a mean interarrival time of 5 to 10 ns is reported. These values were also comparable to the measurement resolution. This suggests that the multipath process of indoor radio channels converges toward a continuous Rayleigh model, and that the blocking of a single ray which we observed is actually only one of many arrivals at a particular time t. If the mean interarrival times had been larger (say 2 or 3 ns), we could have concluded that the ray arrivals are indeed a true discrete process. However, this is not the case. To discern a discrete arrival process from a continuous process the measurement resolution may have to be increased even further in future measurements.

Table 3: Mean Interarrival Times for all Series

Measurement series	$1/\lambda$ (ns)
Reception Room 60 GHz	0.83
Computer Room 60 GHz base station at 2.75 m	0.88
Vax Room	0.97
Hall	1.03
Corridor	0.68
Amphitheatre	0.93
Room 11.21	0.91
Lecture Room	0.71
Reception Room 40 GHz	0.93
Reception Room circular horn on remote	1.06
Reception Room circular horn in corner	1.07
Computer Room 40 Ghz	0.78
Computer Room 60 GHz base station at 1.60 m	1.08
Computer Room 60 GHz circular horn in corner	0.96

9 Comparison of Measurement Results with Simulations

In chapter three a deterministic model for predicting indoor radio channel behaviour has been presented. The question which immediately rises to mind is whether this mathematical model could yield a fair representation of reality. Simulated profiles must look like measured profiles. It was already mentioned that this Geometric Optics model requires actual scattering parameters of objects in the vicinity of transmitting and receiving antennas. To ensure that the simulations are as accurate as possible some rudimentary time domain reflection coefficient measurements were performed in the Reception Room, Room 11.21 and the Lecture Room. In these rooms plus the Computer Room and Corridor the exact locations of transmitting and receiving antennas were administrated. These relative positions were entered in the simulation software. In this chapter simulations at 58 GHz using two biconical horn antennas will be compared to the measured channel characteristics in these five rooms at 57 to 59 GHz.

Figures 19 and 20 in chapter 7 clearly demonstrate that the antenna radiation patterns have a significant impact on channel simulation. To describe the radio channel as accurately as possible a look-up table of a measured elevation radiation pattern of an 58 GHz biconical horn is used for the simulations. The 'simulation' antenna is assumed to be perfectly omnidirectional in the azimuth plane. The software normalizes all profiles to the maximum in that profile, so no statistics on absolute power gains can be given. For the time delay spread, however, the total power gain does not have to be known. The radiation look-up table is also normalized to its maximum.

9.1 Reflection Coefficient Measurements

The simulation software is based on the Fresnel reflection coefficients (22) and (23).
For non-conducting materials these coefficients can be approximated by

$$R_{\perp} = \frac{E_{\perp}^{r}}{E_{\perp}^{i}} = \frac{\cos\theta_i - \sqrt{\epsilon_r - \sin^2\theta_i}}{\cos\theta_i + \sqrt{\epsilon_r - \sin^2\theta_i}}, \tag{62}$$

and

$$R_{\parallel} = \frac{E_{\parallel}^{r}}{E_{\parallel}^{i}} = \frac{\epsilon_r\cos\theta_i - \sqrt{\epsilon_r - \sin^2\theta_i}}{\epsilon_r\cos\theta_i + \sqrt{\epsilon_r - \sin^2\theta_i}}. \tag{63}$$

The program described in [1] expects an ϵ_r for every surface in the room.

For $\theta_i = 0°$ the reflection coefficients become:

$$R_{\perp} = -R_{\parallel} = \frac{1-\sqrt{\epsilon_r}}{1+\sqrt{\epsilon_r}} . \tag{64}$$

So the relative permittivity can be determined using (64) and a measurement of a reflection coefficient with zero incident angle. For metal surfaces formulas (22) and (23) are equal to 1, independent of the incident angle.

9.1.1 Method of Measuring Reflection Coefficients

The method of measuring reflection coefficients of walls is based on the reflecting property of metal. It is known that metal has a unity reflection coefficient. This makes it possible to perform a relative measurement. Two biconical horns were used for the experiments. The horns were placed alongside each other at 1.5 metres height and 1.5 m in front of the wall under consideration. A 1 m*2 m metal plate was placed vertically against the wall in such a way that the Geometric Optical reflection point was located in the middle of the plate. The next step is locating the correct ray in a measured time domain impulse response. This is done by placing a piece of absorber in front of the metal plate and observing the changes in the impulse response.

Once the time of arrival of the reflected ray is known, the absorber is removed and the impulse response is measured again. The strength of the ray is noted. After this the metal plate is removed, the impulse response is measured again and the ray strength at the same time delay is noted again. The quotient of the two strengths is the reflection coefficient we seek. Very important is that for the second measurement the **only** change is the removal of the metal plate. The antennas were not moved in any way between measurements.

Reflection coefficient values found in this manner should be treated with some caution. Frequency dependency of the reflection coefficients cannot be measured because the biconical horns are not frequency independent, that is why these measurements are performed in the time domain. This type of measurement assumes that walls and objects have only one reflecting surface. Because the measurement resolution is limited to 1 ns, it could be possible that the ray strength which was measured without the metal plate is actually a sum of multiple reflections due to a layered structure of the wall. Layered structures up to 15 cm thick will be seen as one surface.

A disadvantage of using Snell's laws of reflection for simulation is that surfaces are electromagnetically flat. Rough surfaces cause EM scattering in directions other than predicted according to Snell's law. At 60 GHz walls with surface irregularities greater than 5 mm are considered to be rough (Rayleigh criterion [9]). This

scattering of EM energy may make the detection of single rays more difficult. Further investigation into this phenomenon may be necessary.

9.2 Reflection Coefficient Values

In table 4 the measured reflection coefficients are given with corresponding ε_r. Due to the limited flexibility of the measurement setup (rigid WR19 waveguides) only walls could be measured. Values of reflection coefficients for floors and ceilings had to be estimated.

Table 4: Measured Reflection Coefficients

Room	Material	R (dB)		ε_r	
		41-43 GHz	57-59 GHz	41-43 GHz	57-59 GHz
Reception Room	windows	-2.1	-13.1	69.1	2.5
	wooden doors	-3.2	-3.9	30.1	20.5
	wooden panels	-9.6	-7.9	4.0	5.5
Lecture Room	wooden lathing	_	-13.0	_	2.6
Room 11.21	concrete walls	_	-2.0	_	81
	metal	1	1	-	-

The values for ε_r were used directly in simulations. For carpeting a relative permittivity of 2 was used (i.e low reflection coefficient). Aluminium ceilings were modelled as metal. Note the increase in reflectivity of the windows and wooden doors, and the decrease of the wooden panels in the Reception Room at 41-43 GHz.

9.3 Discussion of Simulation Results

In figures K.1 to K.10, a comparison is made between measured and simulated average power delay profiles in five rooms. Rooms are modelled as empty rectangular structures. In figures K.11 to K.15 time delay spread statistics of simulations and measurements are compared. These figures also show a decrease in time delay spread values if the maximum time up to which data values are used in the calculations is reduced. The maximal time is limited to the time up to which the simulations predict ray arrivals. Looking at the average power delay profiles the

following conclusions can be drawn:
In the simulations the ray power for small t does not follow an exponential decay in all rooms. The Corridor is an exception. This is caused by the antenna gain compensation of the free-space losses. Rays which arrive just after the LOS ray must have reflected via surfaces which make up the smallest dimension (height) of the room, i.e. the floor and ceiling. These rays experience a small antenna gain. Rays which arrive at the 'end' of the level part of the average power delay profile have travelled further, and consequently suffered a greater free-space loss. These rays reflect against surfaces which make up a larger dimension of the room (length or width), i.e. the walls. The additional free-space loss is amply compensated by the increase in antenna gains which these rays experience (doubling the propagation length causes the free-space loss of an individual ray to increase by only 6 dB). Once the linear slope has set in, the propagation distances are large enough to ensure that rays always reflect off walls at least once. The slope therefore describes the reflection characteristics of the walls of the room. Rays with longer delays which bounce off the floor and ceiling in smaller rooms enter the radiation patterns of the antennas at high angles and are attenuated strongly.

A level part in the average power delay profile of the Corridor is not observed, because the antenna gain compensation of free space losses is much less due to the long narrow structure of the corridor. Simulated time delay spread values are larger than measured results in the Lecture Room. This could indicate that the measured reflection coefficient of the wooden lathing is too large.

Comparison of the measured and simulated profiles clearly indicates that limiting the number of reflections to 4 causes the profiles to terminate to quickly (fig. K.1-K.6). A maximum of 4 reflections causes a simulation profile to end at an excess time delay which corresponds to approximately 4 times the largest dimension of a room. Simulations are inadequate for small rooms with highly reflective walls. Simulated time delay spreads are much to small (fig. K.11). This is also shown by the large decrease in time delay spread if the maximum time considered in calculating σ is reduced. The simulations are, however, adequate for small rooms with low reflective walls, because the average power delay profiles decay rapidly in these rooms (fig. K.3 -K.6). Simulated time delay spread values are definitely comparable to experimental values (fig. K.12 and K.13), especially in the Lecture Room.

For larger rooms like the Reception Room and the Corridor (fig. K.7-K.10), the decrease in power with time is predicted correctly by simulations using Geometric Optics. The limited number of reflections considered in the simulations causes gaps in the average profiles. These rooms were all but empty, so the gaps will not be filled if the model is expanded to incorporate diffracted rays. The simulated time delay spread values for these rooms, however, are still a good representation of the measured results (fig. K.14 and K.15). Note that the standard deviation (i.e. slope of the survival function) of the simulated time delay spreads is comparable to the standard deviation of measured time delay spread values in all rooms. The spatial channel behaviour within a single room can therefore be described very well with

a Geometric Optical model.

9.4 Concluding Remarks on Geometrical Optics Model

In this chapter simulations of the impulse response of indoor radio channels at mm-wave frequencies were compared to actual measured responses. The comparisons show that a Geometric Optical model can definitely be a useful tool for determination of channel behaviour, even with a limited knowledge on reflection coefficients of walls at mm-wave frequencies. To ensure that the model predicts channel behaviour correctly in all indoor environments the software may have to be altered in such a way that a larger number of reflections is considered. Rays which reflect up to 10 times may have to be incorporated in the Geometric Optical model. The theoretical model can only be used for **prediction** of channel behaviour if more data on reflection coefficients becomes available by extensive measurements at mm-wave frequencies.

10 Conclusions and Recommendations

Wideband measurements of indoor radio channels at mm-wave channels have been performed, using nearly omnidirectional biconical horns and one circular horn. Eight different rooms were subjected to propagation experiments. Measurements were performed at at least 20 randomly chosen positions of the remote, with a fixed base station, in each room. An unprecedented measurement resolution of 1 ns was achieved using a vector network analyzer. The measurements were performed in the frequency domain at 41-43 GHz and 57-59 GHz. Using an IFFT algorithm the equivalent complex lowpass impulse response could be calculated. The channels were stationary during measurements. Different setups were considered in two of the rooms. A setup with an omnidirectional remote at table-height and a central omnidirectional base station near the ceiling of a room is most favourable for a uniform spatial channel behaviour, i.e. variations in power gain and time delay spread are small. This should give every user fair access to the communication system. The uniform behaviour is caused by antenna gain compensation of the free-space losses. As a result the power-distance decay rate is very small compared to free-space: less than 0.5 instead of 2. Directional antennas could yield a decrease in time delay spread and an increase in total multipath signal power gain compared to an omni-omni setup. Pointing of antennas, however may be cumbersome in a real office.

Channel behaviour is very diverse in different rooms. This is caused by differences in room-size and reflection properties of walls. A higher wall-reflectivity implies that time delay spread values increase. Metal walls are, however, favourable for total multipath power gain and channel uniformity. Metal objects in a room cause a larger spread in spatial channel behaviour. Differences in channel behaviour at 41-43 GHz and 57-59 GHz are very small, this indicates that the attenuation by the propagation medium has a negligable effect on indoor radio channel behaviour. The higher frequencies are preferable because they suffer a higher atmospheric attenuation, so signal power which leaks through windows, for example, will decay faster outside a building.

Individual rays could be detected in the channel impulse responses. Because of this the multipath rays are modelled as a discrete uncorrelated scattering process. Ray statistics are very similar for all rooms and setups. Rays decay exponentially with time delay. The power-time decay exponents measured in Eindhoven ranged from 16 to 75 ns. The ray arrivals are modelled as a Poisson process with a single arrival rate. The mean of the interarrival times per measurement series ranged from 0.68 to 1.1 ns. Ray amplitudes at a particular delay time follow a Rayleigh distribution. Because the mean of the interarrival times are comparable to the measurement resolution (1 ns) in all rooms, it appears that the ray statistics converge towards a continuous Rayleigh model. Measurements with an even higher resolution could verify this assumption.

The model found here is very similar to the one that Saleh and Valenzuela first proposed. The only difference is that our power delay profiles consist of one cluster only, because signal coverage is limited to one room. The single power-time decay rate they found (20 ns) falls within the range measured at the EUT. Our measurements show, however, that a single value is not adequate for describing all environments.

Time delay spread values between 15 and 100 ns were measured. A worst-case spread of 100 ns is expected in a medium-sized office. This value would limit the achievable unequalized symbolrate to 2 Ms/s. The feasibility of B-ISDN, which operates via mm-wave radio links, must be evaluated by simulation of Decision Feedback Equalizers (DFE). To this end the statistical channel parameters presented in this thesis can be used. Validity of this model can be verified by comparison of DFE simulations which use a statistical description of an indoor radio link or measured profiles.

The number of environments measured is limited. However, because of the difference in size and wall-properties, the measured channel parameters presented in this report should at least give an indication of the range of parameter values which can be expected in comparable rooms.

Comparisons of measurements to simulations which use a Geometric Optics model indicate that this deterministic model could be a useful tool for evaluation and prediction of indoor radio channel behaviour. The number of reflections considered in the software is limited to 4. It is shown that this is insufficient if small rooms with highly reflective walls are considered. The software may have to be altered in such a way that up to 10 reflections are included in the model. Attenuation by the propagation medium can easily be incorporated in the GO model, because the path length of every ray is known. A drawback of this model is that it requires actual scattering parameters of walls and objects in the environment under consideration. These parameters have not yet been reported in literature. Accurate measurement of reflection coefficients at mm-wave frequencies is therefore strongly recommended if this model is to be used in the future. The accuracy of these measurements can be checked by comparison of our measurements to simulations. The Geometric Optics model assumes that walls and objects are electromagnetically smooth. The Rayleigh criterion at 60 GHz, however, shows that walls with surface irregularities which are larger than 5 mm should already be considered as rough surfaces. Further investigation into this phenomenon may be necessary.

11 References

[1] Melters, M.A.A.
Simulation of an indoor radio channel at mm-wave frequencies,
Eindhoven: Eindhoven University of Technology, 1990, graduation thesis

[2] Pugliese, G. and P.W. Huish
A 60 GHz radio system for propagation studies in buildings,
IEE, 3rd Int. Conf. on Antennas and Propagation, pp.181-185, 1983

[3] Ganesh, R. and K. Pahlavan
On the modeling of fading multipath indoor radio channels,
IEEE, GLOBECOM '89, Volume 3, pp.1346-1350

[4] Rappaport, T.S. and S.Y. Seidel
Statistical channel impulse response models for factory and open plan building radio communication system design,
IEEE, Trans. on Comm., Volume 39 no.5, May 1991

[5] Saleh, A.A.M. and R.A. Valenzuela
A statistical model for indoor multipath propagation,
IEEE, Journal on Selected Areas in Communication, Volume SAC-5, pp.128-137, February 1987

[6] Bensebti, M. , J.P. McGeehan and M.A. Beach
Indoor multipath propagation measurements and characterisation at 60 GHz,
21st European Microwave Conference, Stuttgart, September 1991

[7] Pahlavan, K. and S.J. Howard
Frequency domain measurements of indoor radio channels,
Electronic Letters, Volume 25 no. 24, pp.1645-1647, November 1989

[8] Zaghloul, H. , G. Morrison and M. Fattouche
Frequency response and path loss measurements of indoor channels,
Electronic Letters, Volume 27 no. 12, pp.1021-1022, June 1991

[9] Arnbak, J.C. and M.H.A.J. Herben
Radio en Radar,
Eindhoven: Eindhoven University of Technology, lecture notes no.5653, September 1987

[10] Kuo, F.F. and J.F. Kaiser
System analysis by digital computer,
New York: John Wiley and sons, Inc., 1966

[11] Chatterjee, R.
Advanced microwave engineering, special advanced topics,
Chichester: John Wiley and sons, Inc., 1988

[12] Tharek, A.R. and J.P. McGeehan
Propagation and bit error measurements withtin buildings in the mm-wave band about 60 GHz,
IEEE, IICC, pp.318-321, 1988

[13] Allen, G. and A. Hammoudeh
Frequency diversity propagation measurements for an indoor 60 GHz mobile radio link,
IEE, 7th Int. Conf. on Ant. and Prop., pp.298-301, April 1991

[14] Proakis, J.G.
Digital communications,
London: McGraw-Hill, 1983

[15] Uenakada, K. and K. Yasunaga
Horizontal polarization biconical horn antenna exited by TE11 mode in circular guide,
IECE, 1971 Int. Symposium on Ant. and Prop., Summary of Papers, pp.125-126, Sendai, Japan, 1-3 September 1971

[16] Glance, B. and L.J. Greenstein
Frequency selective fading effects in digital mobile radio with diversity combining,
IEEE, Trans. on Comm., Volume COM-31, no. 9, pp.1085-1094, September 1983

[17] Cox, D.C.
Correlation bandwidth and delay spread multipath propagation statistics for 910 urban mobile radio channels,
IEEE, Trans. on Comm., Volume COM-23, no. 11, pp.1271-1280, November 1975

[18] Turin, G. L., et al.
A statistical model of urban multipath propagation,
IEEE, Trans. on Veh. Tech., Volume VT-21, no. 1, pp.1-8, February 1972

[19] Stutzman, W.L. and G.A. Thiele
Antenna theory and design,
New York: John Wiley and Sons, Inc., 1981

[20] Mentzer, C.A., L. Peters Jr. and R.C. Rudduck
Slope diffraction and its application to horns,
IEEE, Trans. on Ant. and Prop., Volume AP-23, pp.153-159, March 1975

[21] Yegani, P. and C.D. McGillem
A statistical model for line-of-sight (LOS) factory radio channels,
IEEE, Proc. 39th Veh. Tech. Conf., pp. 496-503, San Fransisco, May 1989

[22] Yegani, P. and C.D. McGillem
A statistical model for the obstructed factory radio channel,
IEEE, GLOBECOM '89, Volume 3, pp.1351-1355

[23] ERC recommendation T/R 22-03
Provisional recommended use of the frequency range 54.25-66 GHz
by terrestrial fixed and mobile systems,
Athens, 1990

[24] Latheenmaki, J.
Indoor measurements and simulations of propagation at 1.7 GHz,
COST Document: Reference no. 231TD(90)084, January 1990

APPENDIX 1: Influence of non-zero Pulse Width on Parameter Calculations

Total power gain *G*

Suppose each ray is modelled as a δ pulse with height α_n^2 . The total power gain *G* defined by (14) in this case is:

$$G_\delta = \sum_n \alpha_n^2 = \int_{-\infty}^{\infty} \alpha_n^2 \delta(t-\tau_n)\,dt$$

Suppose that instead of delta pulses each path is actually a function $u^2(t)$ i.e. path n is $\alpha_n^2 . u^2(t-\tau_n)$ with

$$u(t) = \frac{1}{\pi I_0(\omega_a \tau)} \cdot \frac{\sin(\omega_a \sqrt{t^2-\tau^2})}{\sqrt{t^2-\tau^2}}$$

So the power gain becomes:

$$\begin{aligned} G_u &= \int_{-\infty}^{\infty} \alpha_n^2 u^2(t-\tau_n)\,dt \\ &= \sum_n \alpha_n^2 . \int_{-\infty}^{\infty} u^2(t)\,dt \\ &= G_\delta . \int_{-\infty}^{\infty} u^2(t)\,dt \end{aligned}$$

The calculation of the total multipath power gain can simply be split into two parts, one for actual gain caused by multiple paths and the second due to the power gain of a single pulse. This is also true for the time delay spread. Suppose that one pulse contains 1 nW of power and that 100 of such pulses (very small number for a practical profile) make up the the total power *G*. The total power then equals -70 dBW. In this case the error is only 1%.

Time delay spread σ

Suppose the spread (second centralised moment) of a single pulse is denoted by σ_p , the time delay spread calculated with non-zero width pulses is σ_s and real time delay spread is σ_t . It will be shown that:

$$\sigma_t^2 = \sigma_s^2 - \sigma_p^2$$

σ_p^2 is equal to:

$$\sigma_p^2 = \frac{\int_{-\infty}^{\infty} t^2 u^2(t)\,dt}{\int_{-\infty}^{\infty} u^2(t)\,dt} - \frac{\left(\int_{-\infty}^{\infty} t u^2(t)\,dt\right)^2}{\left(\int_{-\infty}^{\infty} u^2(t)\,dt\right)^2}$$

σ_s (15) equals:

$$\sigma_s^2 = \frac{\int_{-\infty}^{\infty} \left(t^2 \sum_n \alpha_n^2 u^2(t-\tau_n) \right) dt}{\int_{-\infty}^{\infty} \sum_n \alpha_n^2 u^2(t-\tau_n)\,dt} - \frac{\left(\int_{-\infty}^{\infty} \left(t \sum_n \alpha_n^2 u^2(t-\tau_n) \right) dt \right)^2}{\left(\int_{-\infty}^{\infty} \sum_n \alpha_n^2 u^2(t-\tau_n)\,dt \right)^2}$$

$$\sigma_s^2 = \frac{\int_{-\infty}^{\infty} \left((t+\tau_n)^2 \sum_n \alpha_n^2 u^2(t) \right) dt}{\left(\sum_n \alpha_n^2\right) \int_{-\infty}^{\infty} u^2(t)\,dt} - \frac{\left(\int_{-\infty}^{\infty} \left((t+\tau_n) \sum_n \alpha_n^2 u^2(t) \right) dt \right)^2}{\left(\sum_n \alpha_n^2\right)^2 \left(\int_{-\infty}^{\infty} u^2(t)\,dt \right)^2}$$

$$\sigma_s^2 = \frac{\sum_n \alpha_n^2 \tau_n^2}{\sum_n \alpha_n^2} + \frac{\left(2 \sum_n \alpha_n^2 \tau_n\right) \int_{-\infty}^{\infty} t u^2(t)\,dt}{\left(\sum_n \alpha_n^2\right) \int_{-\infty}^{\infty} u^2(t)\,dt} + \frac{\int_{-\infty}^{\infty} t^2 u^2(t)\,dt}{\int_{-\infty}^{\infty} u^2(t)\,dt} +$$

$$- \frac{\left(\sum_n \alpha_n^2 \tau_n\right)^2 \left(\int_{-\infty}^{\infty} u^2(t)\,dt\right)^2}{\left(\sum_n \alpha_n^2\right)^2 \left(\int_{-\infty}^{\infty} u^2(t)\,dt\right)^2}$$

$$- \frac{2\left(\sum_n \alpha_n^2 \tau_n\right)\left(\sum_n \alpha_n^2\right)\left(\int_{-\infty}^{\infty} u^2(t)\,dt\right)\left(\int_{-\infty}^{\infty} t u^2(t)\,dt\right)}{\left(\sum_n \alpha_n^2\right)^2 \left(\int_{-\infty}^{\infty} u^2(t)\,dt\right)^2} +$$

$$- \frac{\left(\sum_n \alpha_n^2\right)^2 \left(\int_{-\infty}^{\infty} t u^2(t)\,dt\right)^2}{\left(\sum_n \alpha_n^2\right)^2 \left(\int_{-\infty}^{\infty} u^2(t)\,dt\right)^2}$$

So σ_s^2 equals:

$$\sigma_s^2 = \frac{\sum_n \alpha_n^2 \tau_n^2}{\sum_n \alpha_n^2} + \frac{\int_{-\infty}^{\infty} t^2 u^2(t)\,dt}{\int_{-\infty}^{\infty} u^2(t)\,dt} - \frac{\left(\sum_n \alpha_n^2 \tau_n\right)^2}{\left(\sum_n \alpha_n^2\right)^2} - \frac{\left(\int_{-\infty}^{\infty} t u^2(t)\,dt\right)^2}{\left(\int_{-\infty}^{\infty} u^2(t)\,dt\right)^2}$$

$$= \sigma_i^2 + \sigma_p^2$$

Q.E.D.

Suppose that for a worst case calculation $u^2(t) = 1$ for abs(t) < 2 ns and 0 for abs(t) > 2 ns.

σ_p then equals:

$$\sigma_p = \frac{5.333 \cdot 10^{-27}}{4 \cdot 10^{-9}} - 0 = 1.15 \quad (ns)$$

For delay spreads greater than 10 ns this non-zero pulsewidth introduces an error which is less than 1%.

APPENDIX 2: Tabulation of Average Power versus Time Delay Slopes

Measurement series	slope B (dB/ns)	R
Reception Room 60 GHz	-0.125	0.99
Computer Room 60 GHz base station at 2.75 m	-0.093	0.98
Vax Room	-0.084	0.95
Hall	-0.072	0.90
Corridor	-0.058	0.95
Amphitheatre	-0.142	0.99
Room 11.21	-0.173	0.98
Lecture Room	-0.268	0.98
Reception Room 40 GHz	-0.124	0.99
Reception Room circular horn on remote	-0.110	0.95
Reception Room circular horn in corner	-0.099	0.94
Computer Room 40 Ghz	-0.092	0.98
Computer Room 60 GHz base station at 1.60 m	-0.088	0.97
Computer Room 60 GHz circular horn in corner	-0.105	0.98

APPENDIX 3: Tabulation of Power Decay Exponents

Measurement series	decay rate *m* LOS	decay rate *m* OBS
Reception Room 60 GHz	0.17	0.078
Computer Room 60 GHz base station at 2.75 m	0.46	0.48
Vax Room	-0.30	0.014
Hall	0.10	0.73
Corridor	0.49	0.75
Amphitheatre	0.21	-0.048
Room 11.21	-0.59	-0.13
Lecture Room	-1.65	-0.051
Reception Room 40 GHz	0.20	0.25
Reception Room circular horn on remote	0.50	-0.026
Reception Room circular horn in corner	0.59	0.11
Computer Room 40 Ghz	-0.19	-0.16
Computer Room 60 GHz base station at 1.60 m	0.008	-0.062
Computer Room 60 GHz circular horn in corner	-0.66	-1.30

FACULTY OF ELECTRICAL ENGINEERING
EINDHOVEN UNIVERSITY OF TECHNOLOGY
Telecommunications Division

Measurement and Statistical Modelling of Indoor Radio Channels in the mm-Wave Frequency Band

PART 2: Additional Figures

By: A.G. Wagemans

Graduation Thesis

Period	:	May 1991 - February 1992
Mentors	:	Ir. P.F.M. Smulders
		Dr. Ir. M.H.A.J. Herben
Supervisor	:	Prof. Dr. Ir. G. Brussaard

Contents

PART 1

A Phase Response of Polarizers

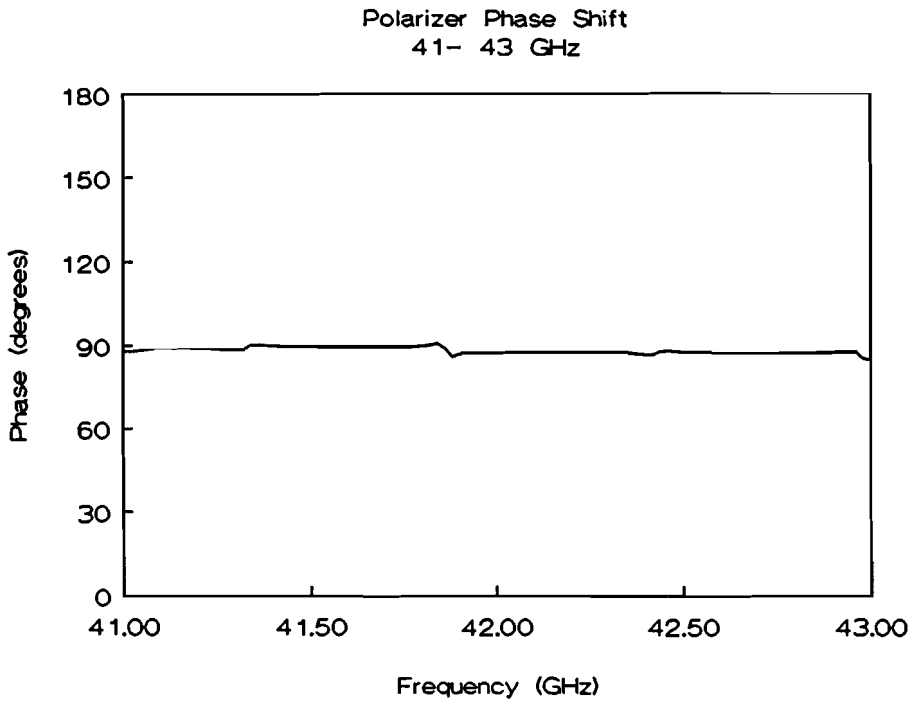

Figure A.1

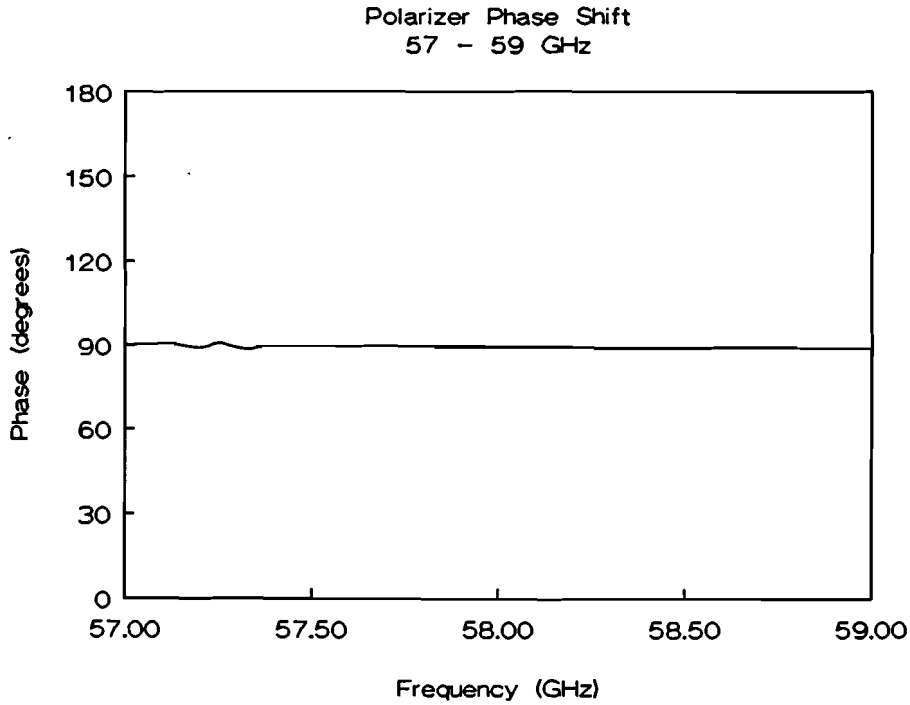

Figure A.2

B Standing Wave Ratios of the Biconical Horns

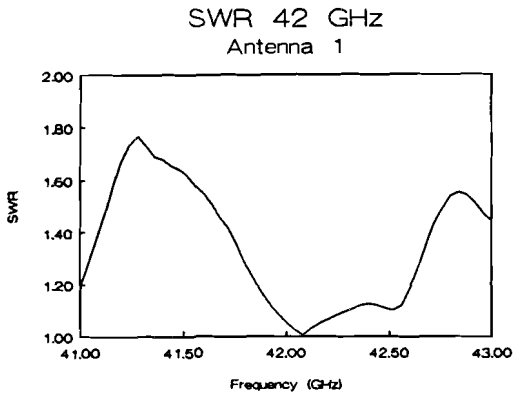

Figure B.1

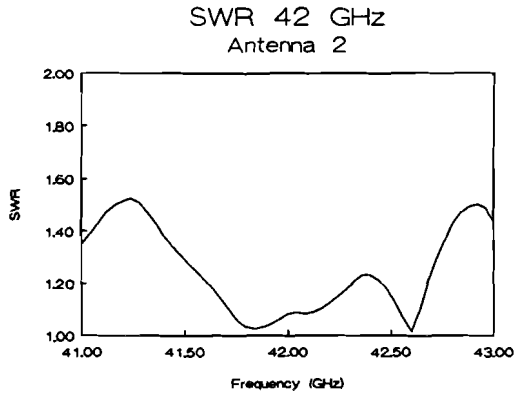

Figure B.2

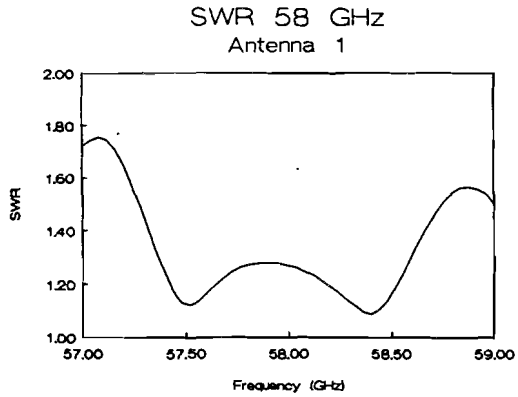

Figure B.3

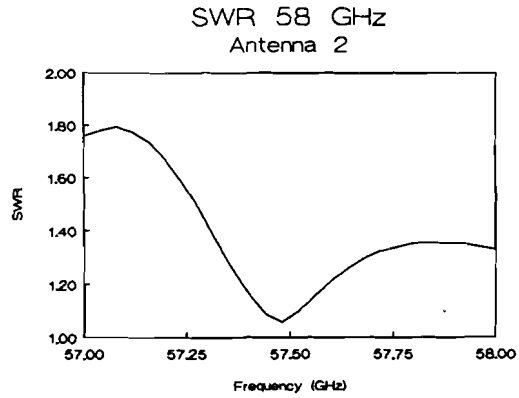

Figure B.4

C Measured Radiation Patterns of Biconical Horns

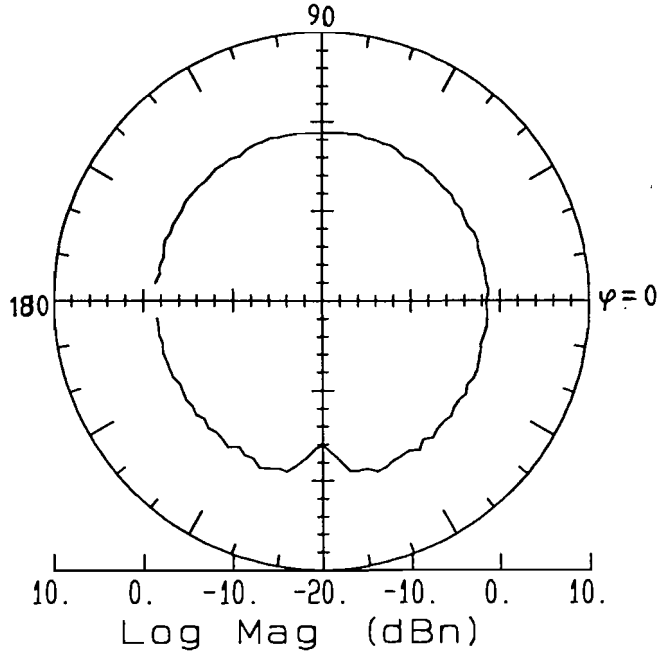

Figure C.1: Co-polar Radiation in the Azimuth Plane, 42 GHz, Biconical Horn 1.

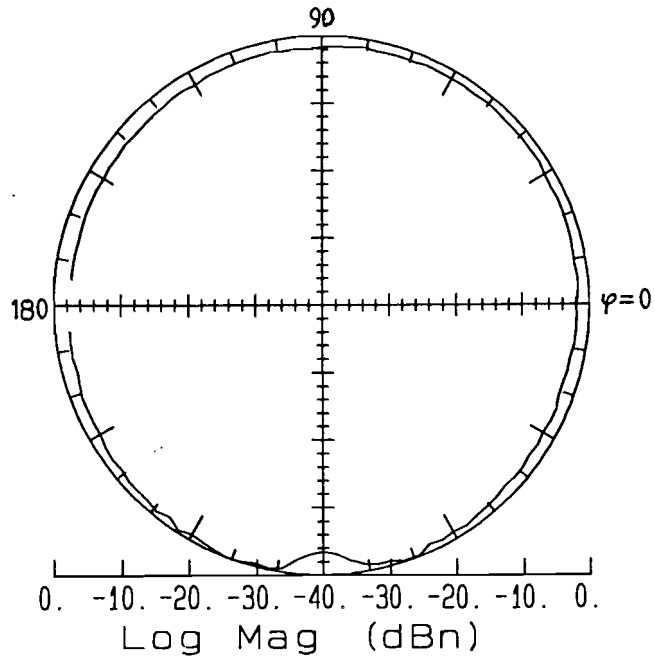

Figure C.2: Co-polar Radiation in the Azimuth Plane, 42 GHz, Biconical Horn 2.

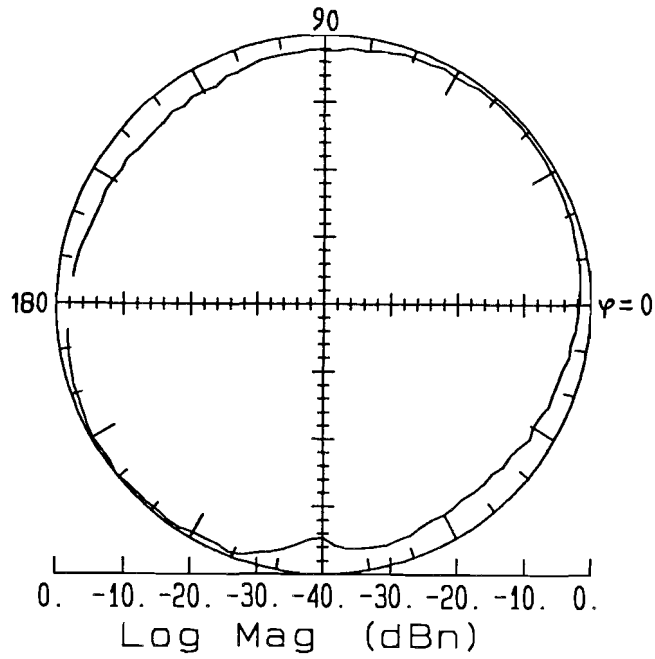

Figure C.3: Co-polar Radiation in the Azimuth Plane, 58 GHz, Biconical Horn 1.

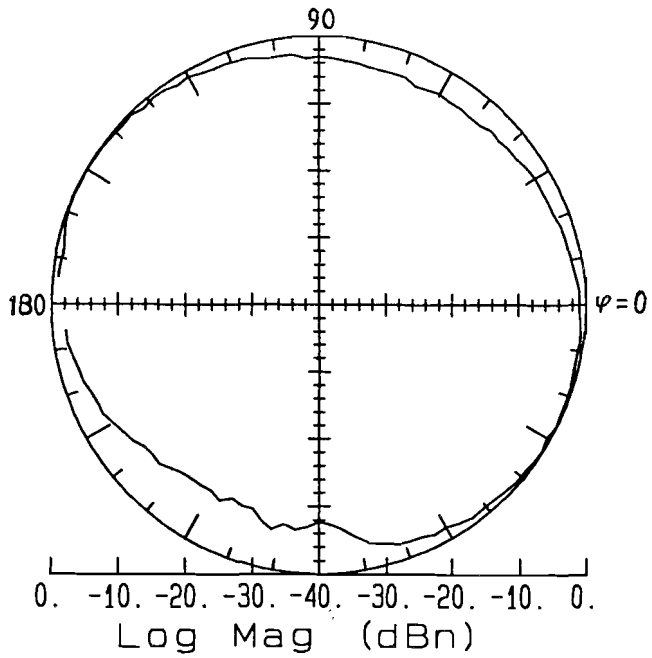

Figure C.4: Co-polar Radiation in the Azimuth Plane, 58 GHz, Biconical Horn 2.

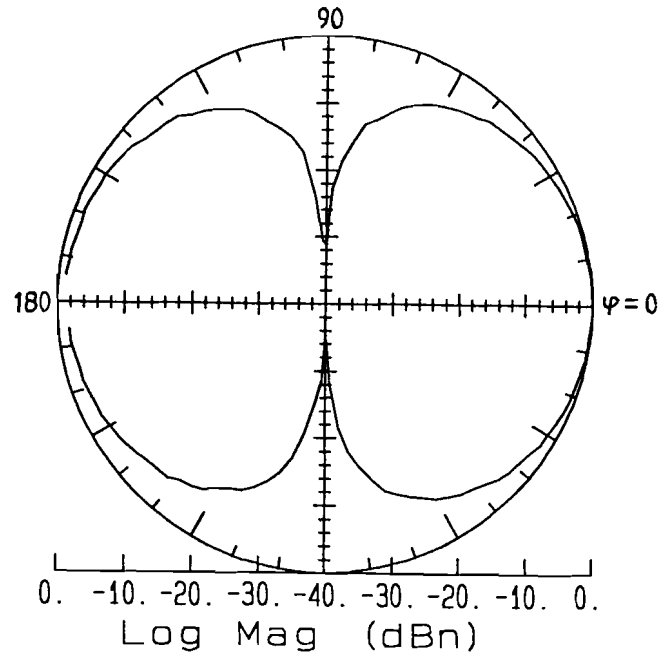

Figure C.5: Co-polar Radiation in the Azimuth Plane, 58 GHz, Biconical Horn 2, no Polarizer.

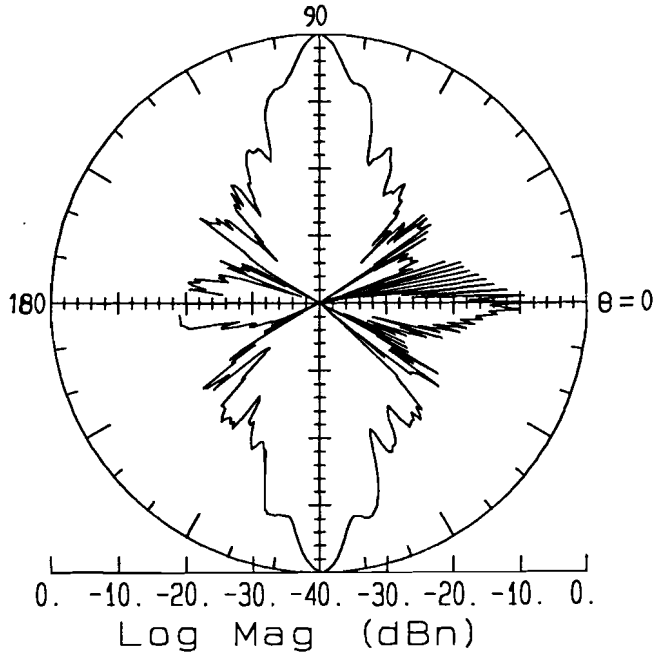

Figure C.6: Co-polar Radiation in the Elevation Plane, 42 GHz, Biconical Horn 1.

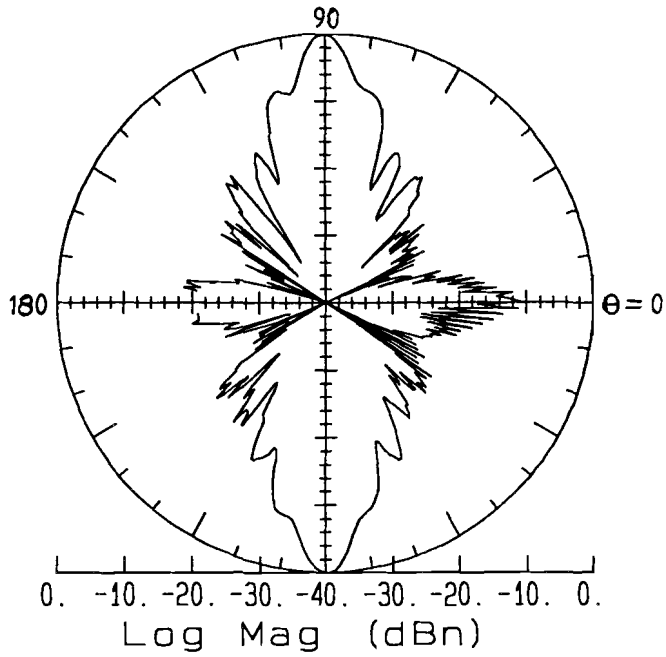

Figure C.7: Co-polar Radiation in the Elevation Plane, 42 GHz, Biconical Horn 2.

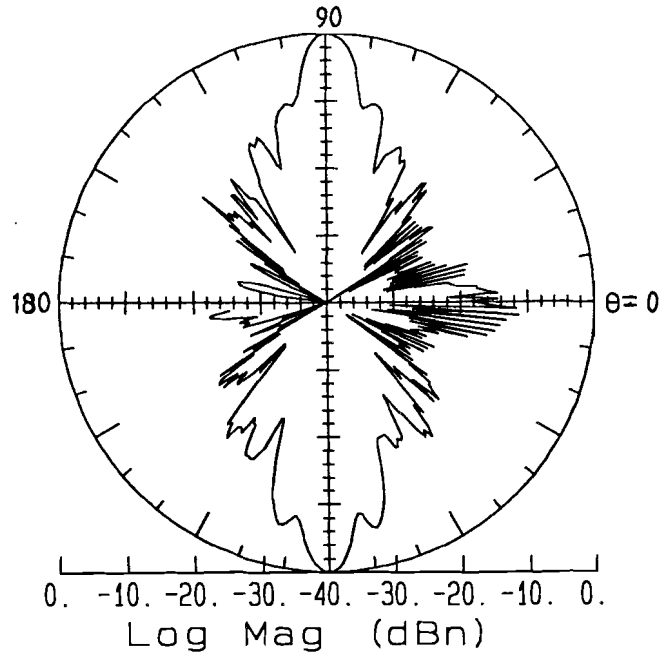

Figure C.8: Co-polar Radiation in the Elevation Plane, 58 GHz, Biconical Horn 1.

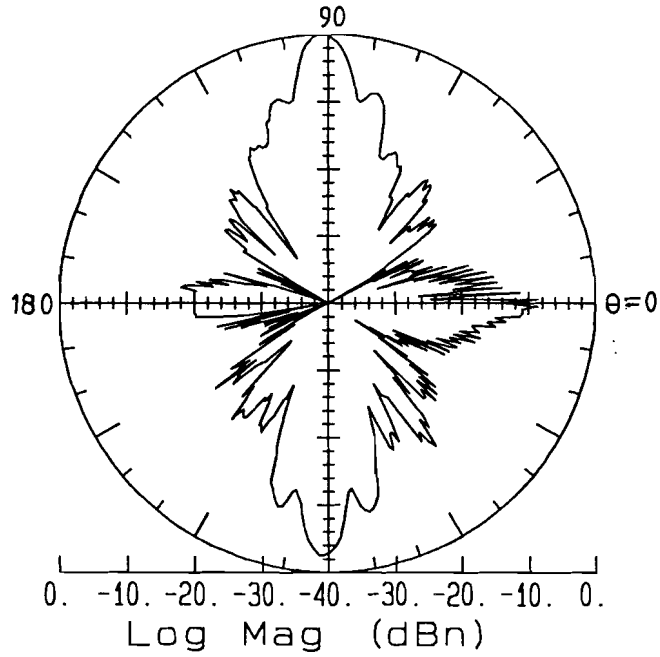

Figure C.9: Co-polar Radiation in the Elevation Plane, 58 GHz, Biconical Horn 2.

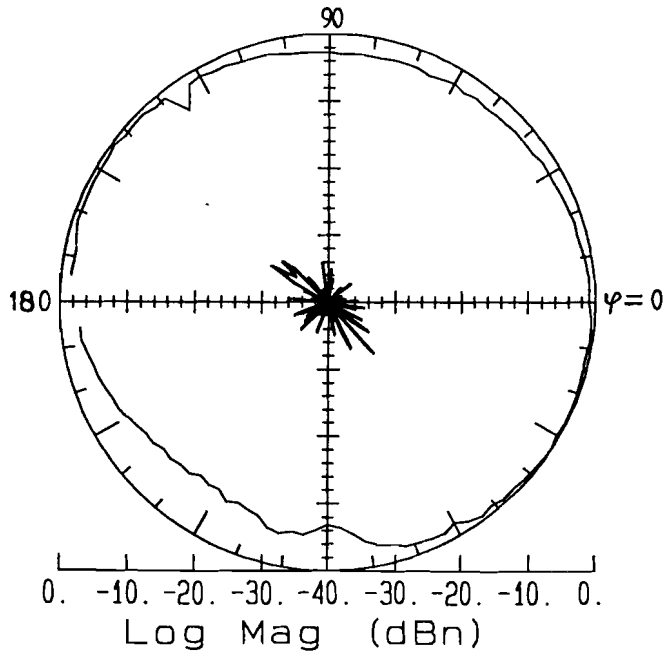

Figure C.10: Co- and Cross-polar Radiation in the Azimuth Plane, 58 GHz Biconical Horn 2.

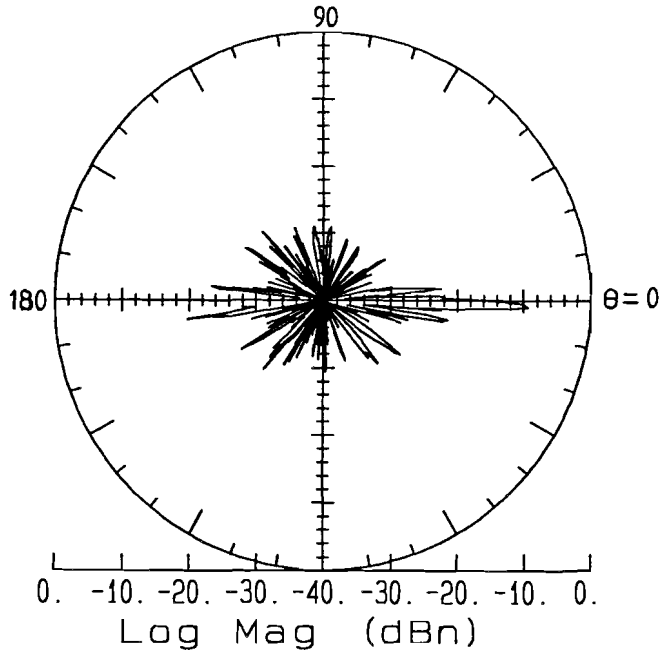

Figure C.11: Cross-polar Radiation in the Elevation Plane, 58 GHz, Biconical Horn 2.

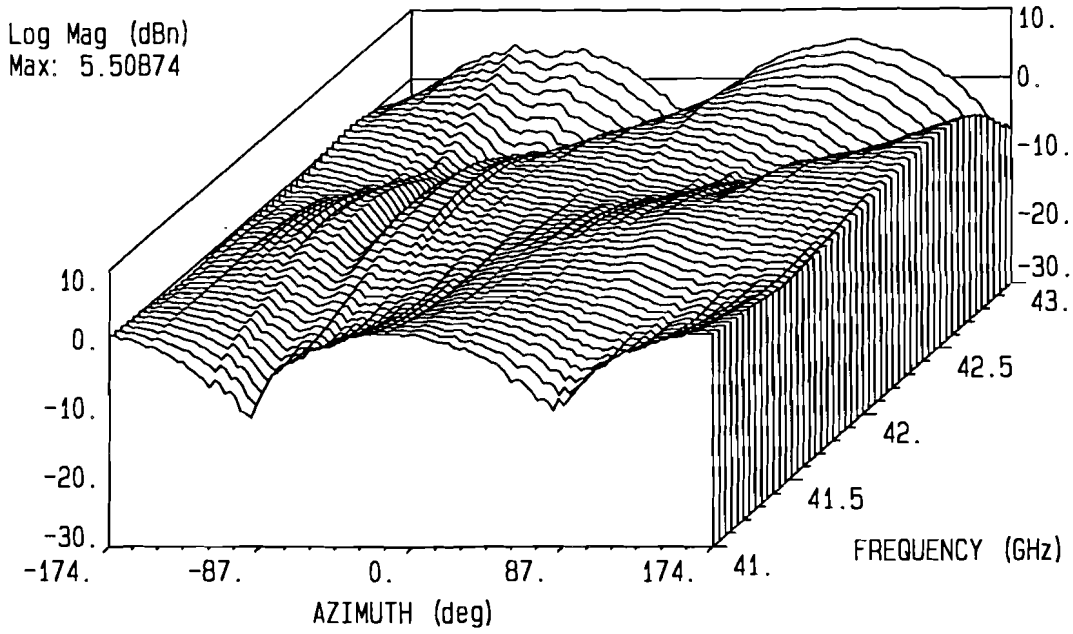

Figure C.12: Co-polar Azimuth Plane Radiation versus Frequency, 41-43 GHz, Biconical Horn 1, with Polarizer.

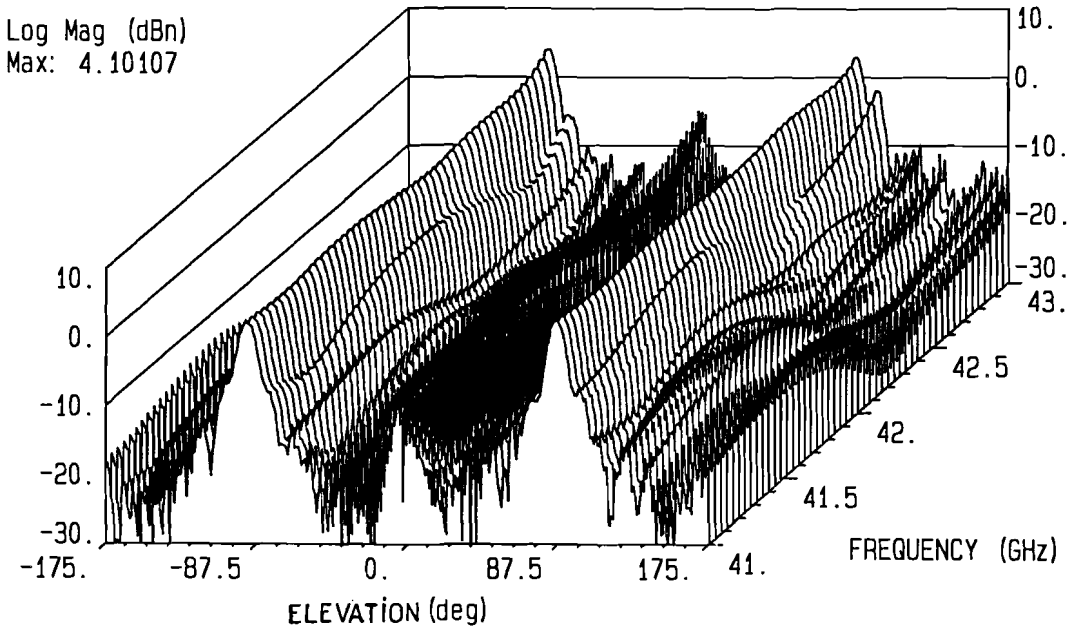

Figure C.13: Co-polar Elevation Plane Radiation versus Frequency, 41-43 GHz, Biconical Horn 1, with Polarizer.

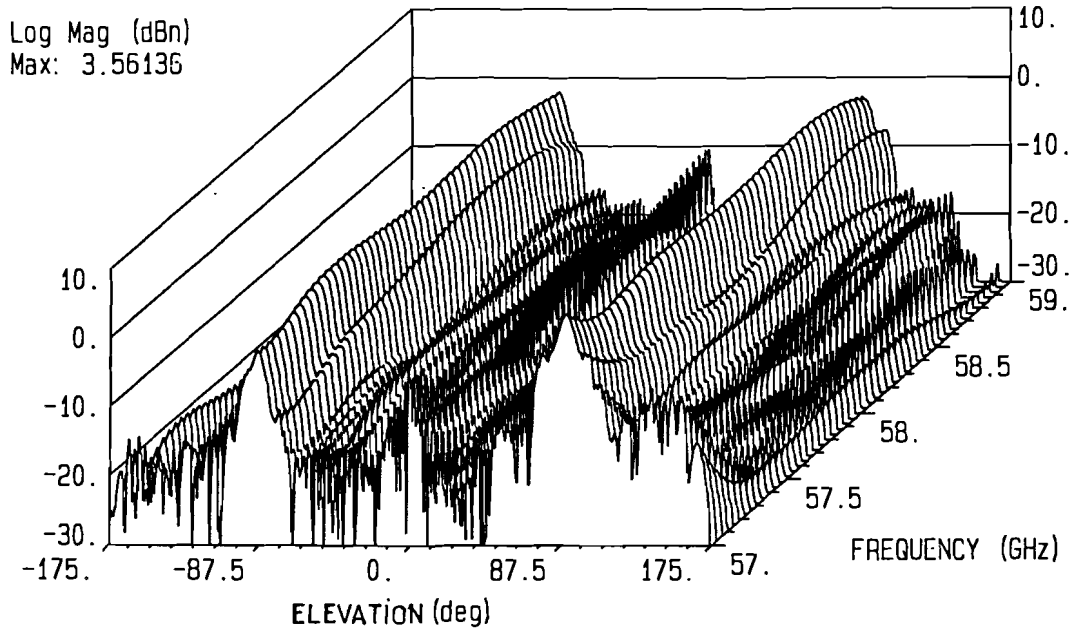

Figure C.14: Co-polar Elevation Plane Radiation versus Frequency, 57-59 GHz, Biconical Horn 1, with Polarizer.

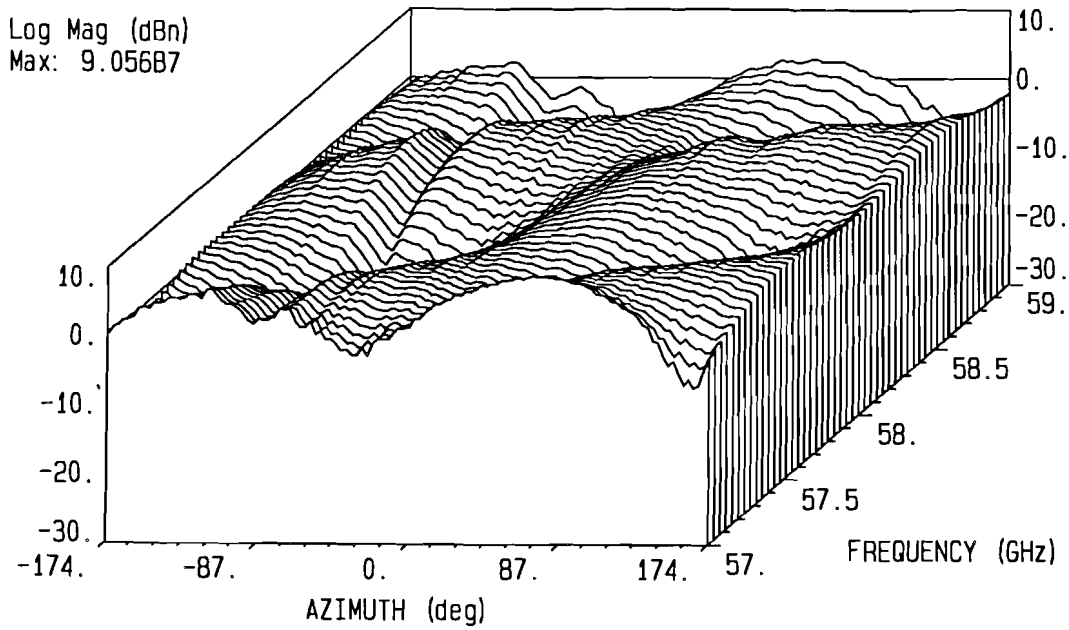

Figure C.15: Co-polar Azimuth Plane Radiation versus Frequency, 57-59 GHz, Biconical Horn 1, with Polarizer.

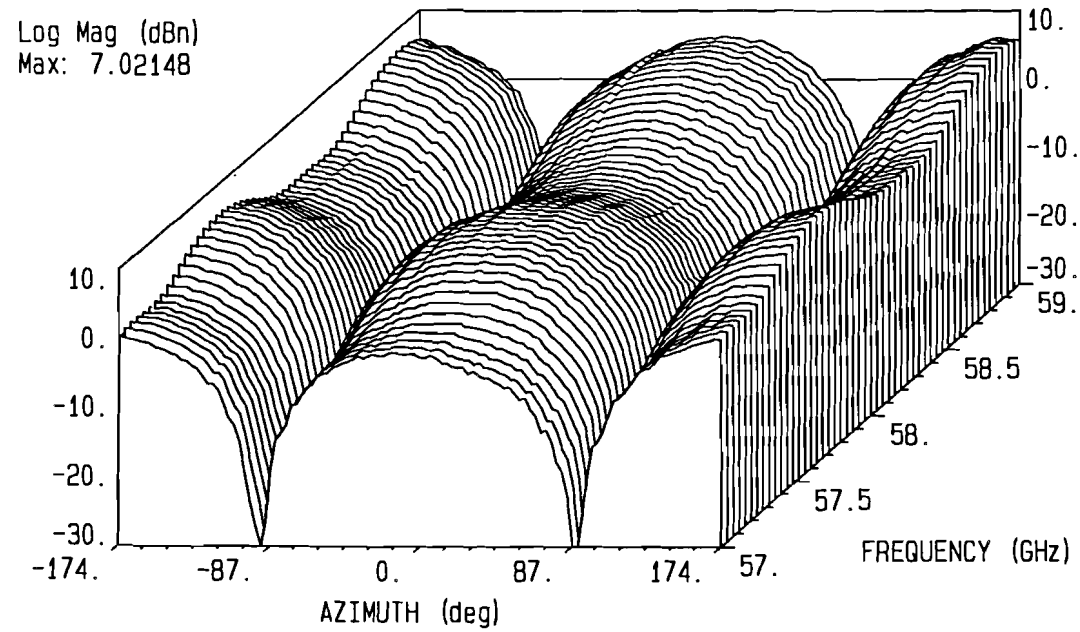

Figure C.16: Co-polar Azimuth Plane Radiation versus Frequency, 57-59 GHz, Biconical Horn 1, no Polarizer.

D Biconical Horn Directivity

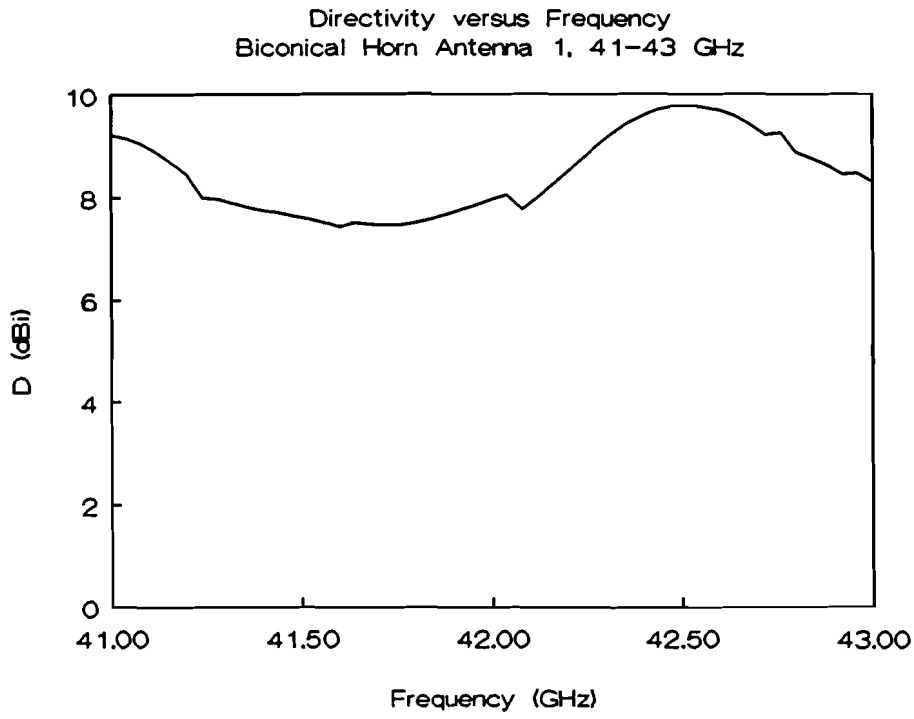

Figure D.1

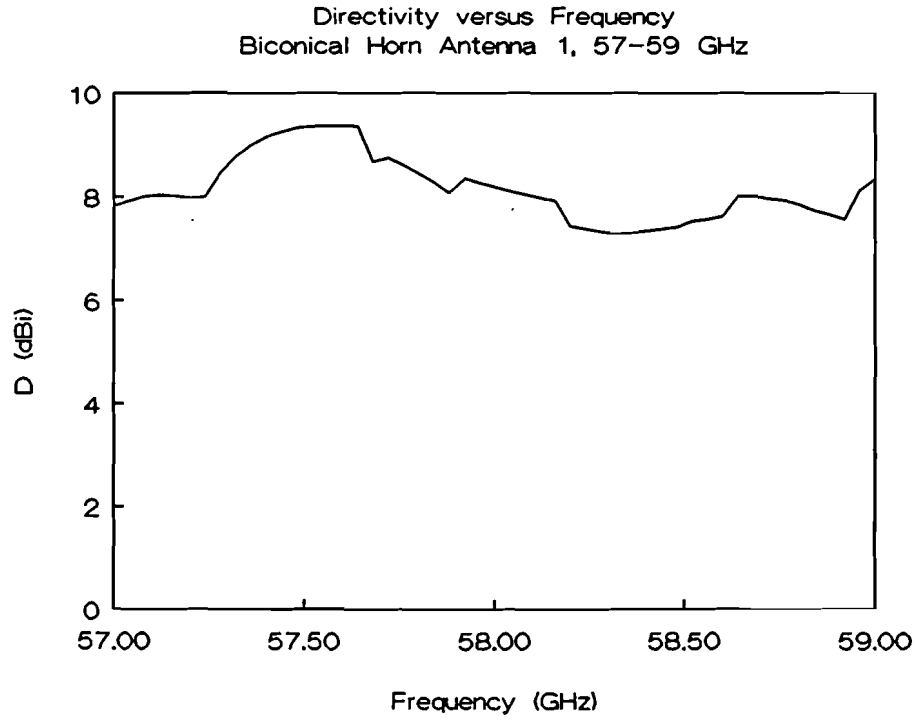

Figure D.2

E Measured Properties of the 58 GHz Circular Horn

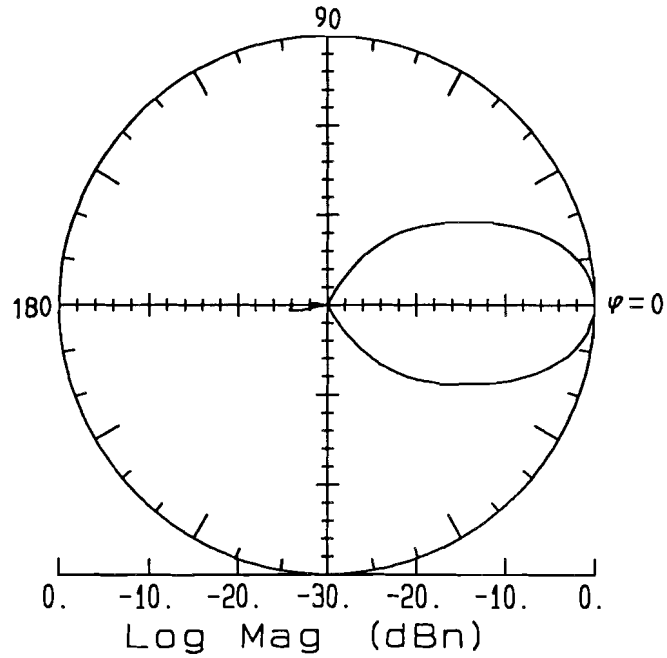

Figure E.1: Co-polar Azimuth Radiation Pattern.

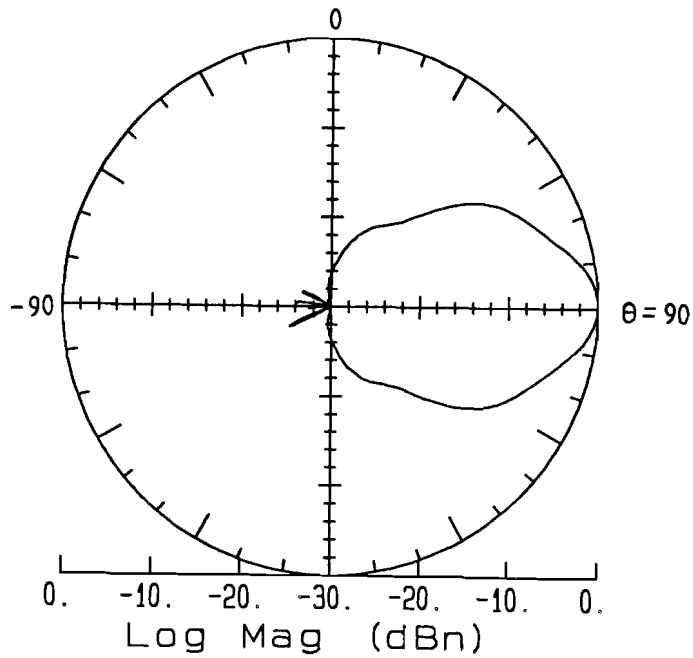

Figure E.2: Co-polar Elevation Radiation Pattern.

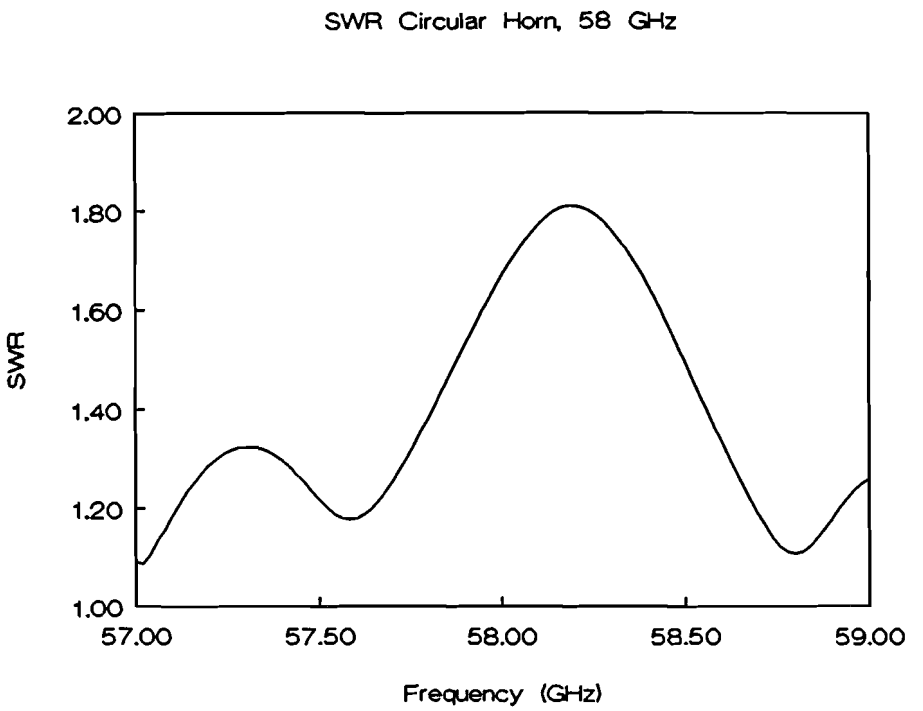

Figure E.3

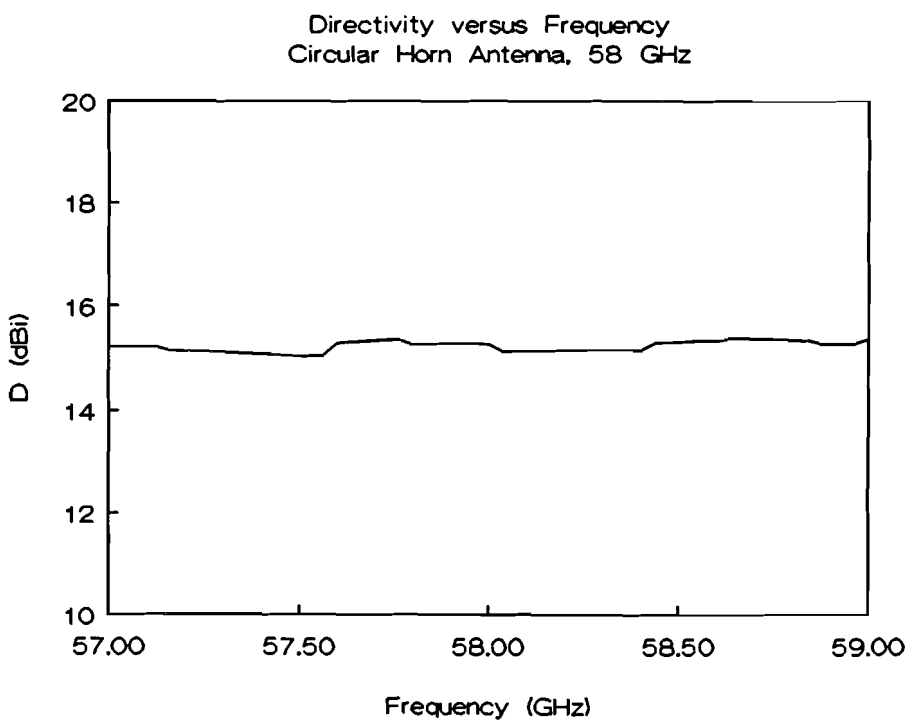

Figure E.4

F Documentation of the Indoor Measurement Environments

F.1 Corridor in Computing Centre Building

One 60 GHz measurement series at 21 positions. Coordinates noted at every position. Filenames: T**6ol.
Base station: Centrally placed biconical horn at 2.75 m height.
Remote : Biconical horn at 1.38 m height.

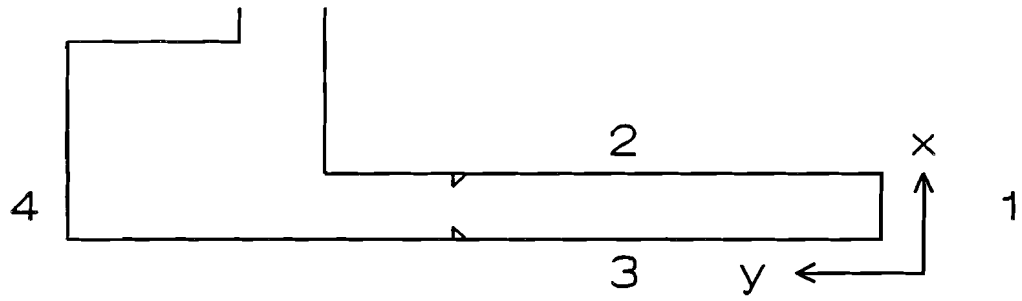

Figure F.1: Layout Corridor

Size (h*w*l) : 3.12 m * 2.43 m * 44.68 m

Floor : thin carpeting
Ceiling : Aluminium profiles
Walls 2 and 3 : metal with glass above
Walls 1 and 4 : glass doors in steel frame

Measurement positions:

Position	x (m)	y(m)	Position	x (m)	y (m)
1	0.88	26.95	12	1.50	15.60
2	1.36	28.23	13	1.34	13.75
3	1.79	29.95	14	1.48	12.20
4	1.20	31.80	15	0.78	10.40
5	0.90	33.85	16	1.70	8.70
6	1.25	35.95	17	0.55	6.75
7	2.30	37.10	18	1.30	5.25
8	3.52	37.32	19	1.65	3.45
9	0.75	36.60	20	0.38	3.50
10	1.77	24.40	21	0.50	12.65
11	0.90	23.75	base station	1.23	

Remarks:

Position 8: No LOS.

Special measurements:

T046old glass doors halfway in corridor closed.

F.2 Computer Room in Computing Centre Building

3 Measurement series at 57-59 GHz and one series at 41-43 GHz.
Series 1: Central biconical base station at 2.75 m height, biconical remote at 1.38 m height. Frequency 57-59 GHz. Filenames: T**6ol.
Series 2: Same as series 1, except base station height is 1.60 m. Filenames: T**6oll.
Series 3: Same as 1, except frequency is 41-43 GHz. Filenames: T**4ol.
Series 4: Circular horn base station placed in corner, biconical remote at 1.38 m height. Frequency is 57-59 GHz. Filenames: T**6hl.

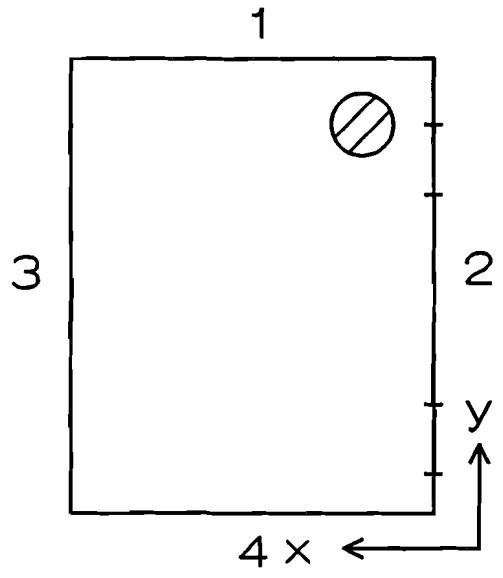

Figure F.2: Layout Computer Room

Size (h*w*l) : 3.12 m * 8.65 m * 9.86 m

Floor : thin carpeting
Ceiling : aluminium profiles
Walls 1,2 and 4 : metal with glass above
Wall 3 : glass windows in steel frame

Measurement positions:

Position	x (m)	y (m)	Position	x (m)	y (m)
1	1.60	4.18	12	7.05	7.25
2	1.06	2.72	13	7.02	5.81
3	0.53	1.15	14	6.86	6.00
4	2.44	1.05	15	5.39	5.31
5	1.04	5.73	16	7.05	3.82
6	1.12	6.91	17	5.90	2.92
7	1.52	7.98	18	4.16	2.86
8	2.96	8.00	19	2.78	2.84
9	3.95	9.23	20	4.15	3.85
10	5.24	7.92	21	4.32	4.93
11	7.02	9.30	cent. base station	4.32	4.93
corner base stn	7.32	0.71			

Special measurements:

T**6hn: LOS path obstructed with absorber.
T076hlc: chairs placed on top of tables.
T146olg: curtains in front of windows closed.

F.3 Vax Room in Computing Centre Building

One 57-59 GHz measurement series at 20 positions. Filenames T**6ol.
Base station: Centrally placed biconical horn at 2.75 m height.
Remote : Biconical horn at 1.38 m height.

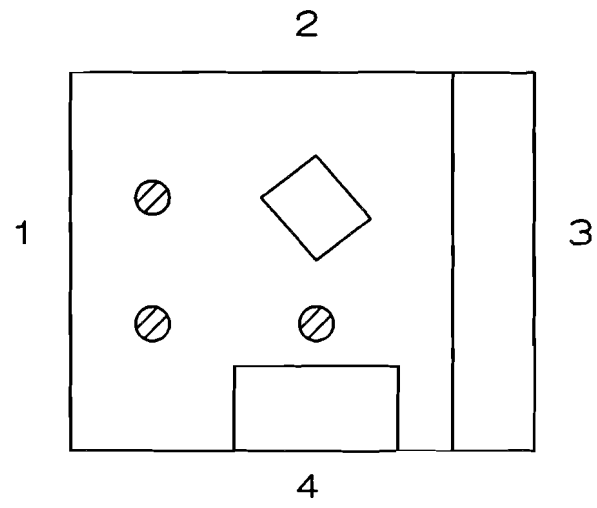

Figure F.3: Layout Vax Room

Size (h*w*l) : 3.12 m * 32.20 m * 33.50 m

Floor : linoleum on concrete
Ceiling : aluminium profiles
Walls : glass, concrete and metal

Measurement positions:

Position	Hor. distance (m)	Postition	Hor. distance (m)
1	9.10	11	15.35
2	12.40	12	17.90
3	10.40	13	20.50
4	5.35	14	18.00
5	3.55	15	15.30
6	2.25	16	13.35
7	7.45	17	11.50
8	10.30	18	11.20
9	12.30	19	8.50
10	7.55	20	7.25

Remarks:

Position 3 : LOS path obstructed by concrete pillar.
Position 18: LOS path obstructed by concrete pillar.

Special measurements:

File T156olb : One dominant reflected ray from a metal filing cabinet blocked by absorber.
File T156olh : Human blocking LOS path at 1m from remote.

F.4 Reception room in Auditorium

3 Measurement series at 57-59 GHz and one series at 41-43 GHz.
Series 1: Central biconical base station at 3.00 m height, biconical remote at 1.38 m height. Frequency 57-59 GHz. Filenames: T**6ol.
Series 2: Same as series 1, except frequency is 41-43 GHz. Filenames T**4ol.
Series 3: Circular horn base station placed in corner at 3.00 m, biconical remote at 1.38 m height. Frequency is 57-59 GHz. Filenames: T**6hl.
Series 4: Central biconical base station at 3.00 m height, circular horn remote at 1.38 m height. Remote horn aimed towards base station at every position. Frequency is 57-59 GHz. filenames: T**6ml.

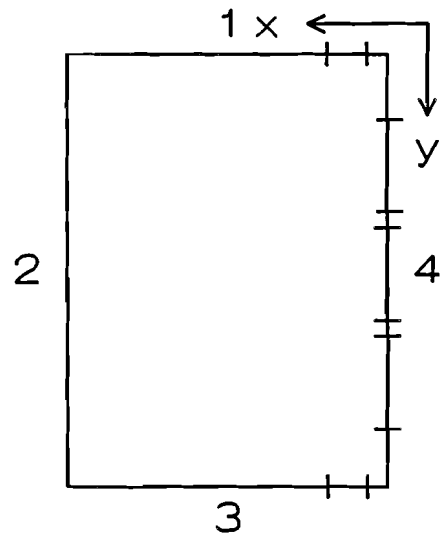

Figure F.4: Layout Reception Room

Size (h*w*l)	: 4.50 m * 11.15 m * 24.30 m
Floor	: thick carpeting
Ceiling	: complex plastic and metal structure
Walls 1 and 3	: smooth wooden panels
Wall 2	: glass windows in steel frame
Wall 4	: wooden doors and wood panelling

Measurement positions:

Position	x (m)	y (m)	Position	x (m)	y (m)
0	5.55	12.20	13	1.13	12.20
1	0.89	1.35	14	1.06	15.22
2	3.60	2.79	15	3.55	15.22
3	5.95	2.79	16	7.39	15.22
4	8.58	2.79	17	7.40	18.30
5	8.68	6.02	18	4.43	18.30
6	5.98	6.02	19	1.58	18.30
7	3.67	6.02	20	5.70	21.33
8	1.41	6.02	21	3.15	23.69
9	1.40	9.13	22	9.47	21.50
10	5.60	9.13	23	1.88	2.54
11	9.35	9.13	24	7.84	19.66
12	8.53	12.20	cent. base station	5.55	12.20
corner base stn	10.43				

F.5 Hall in Auditorium Building

One measurement series at 57-59 GHz at 22 positions.
Base station: Centrally placed biconical horn at 3.00 m height.
Remote : Biconical horn at 1.38 m height.

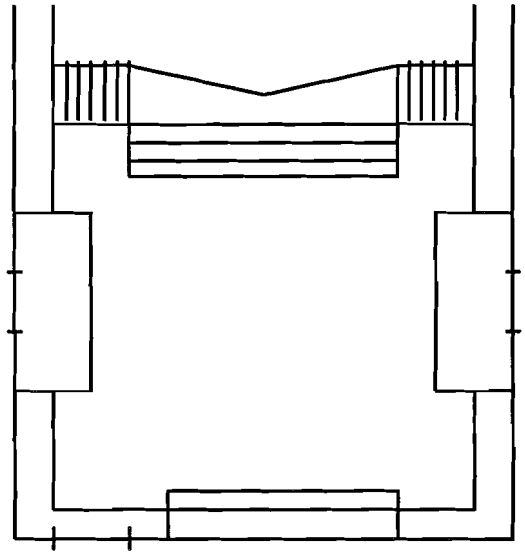

Figure F.5: Layout Auditorium Hall

Size (h*w*l) : 8.5 m * 41 m * 43 m

Floor : linoleum on concrete
Ceiling : aluminium
Walls : glass windows, bare concrete

Measurement positions:

Position	Hor. distance (m)	Postition	Hor. distance (m)
1	15.50	12	15.80
2	18.65	13	19.40
3	21.55	14	21.35
4	13.65	15	12.45
5	10.30	16	17.00
6	8.55	17	20.00
7	5.80	18	23.25
8	4.00	19	25.35
9	2.70	20	27.40
10	6.65	21	31.15
11	10.60	22	28.10

Special measurements:

T176ols: Metal screen parallel to LOS path added to channel.
T176olp: Same screen perpendicular to LOS path between T_x and R_x. LOS.
T176olq: Same as T176olp, except screen placed higher to block LOS.
T176olr: Same as T176olq, except LOS path just blocked by a few cm of screen. Diffraction.
T176olt: Same as T176olr, except LOS path nearly blocked.
T176olu: Complete blockage of LOS path by broad wooden screen in vincinity of remote.
T176olv: Same as T176olu, except screen is made of chip board.

F.6 Amphitheatre in Auditorium Building

One measurement series at 57-59 GHz at 21 positions.
Base station: Centrally placed biconical horn at 3.00 m height.
Remote : Biconical horn at 1.38 m height.

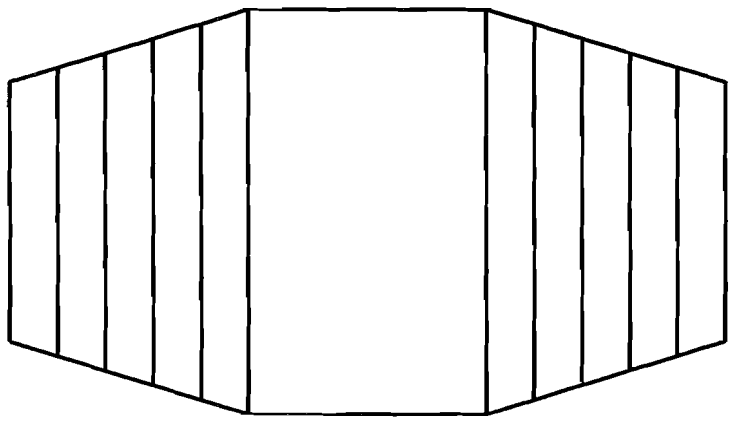

Figure F.6: Layout Auditorium Amphitheatre

Size(h*w*l) : 7.2 m * 21 m * 30 m

Floor : wood
Ceiling : plastic
Walls : concrete covered with acoustic absorbent materials

Measurement positions:

Position	Hor. distance (m)	Postition	Hor. distance (m)
1	12.85	12	1.65
2	14.40	13	3.68
3	12.85	14	5.48
4	11.25	15	8.10
5	10.40	16	9.70
6	8.40	17	9.85
7	6.78	18	12.46
8	9.25	19	12.00
9	8.80	20	6.10
10	10.70	21	5.75
11	7.80		

F.7 Lecture room in Auditorium Building

One measurement series at 57-59 GHz at 18 positions.
Base station: Centrally placed biconical horn at 2.75 m height.
Remote : Biconical horn at 1.38 m height.

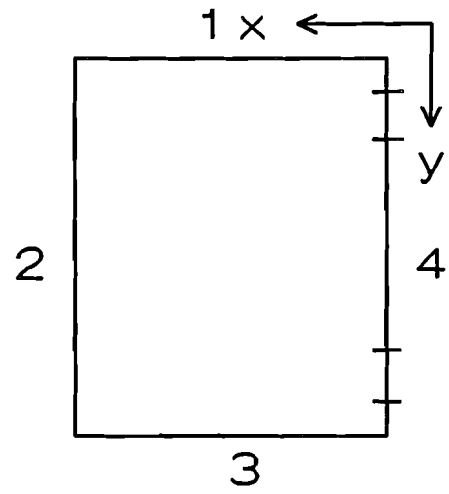

Figure F.7: Layout Lecture Room

Size (h*w*l)	: 4.00 m * 8.85 m * 12.85 m
Floor	: linoleum on concrete
Ceiling	: aluminium
Wall 2	: glass windows in a steel frame
Walls 1,3 and 4	: wooden lathing

Measurement positions:

Position	x (m)	y (m)	Position	x (m)	y (m)
1	0.43	3.19	10	4.30	12.24
2	1.85	3.19	11	4.60	10.03
3	1.62	4.61	12	5.90	11.74
4	0.70	6.05	13	8.60	12.29
5	2.18	6.20	14	7.00	10.68
6	1.90	7.80	15	7.02	9.28
7	1.80	9.82	16	7.81	8.20
8	2.67	11.06	17	7.82	6.65
9	1.55	12.24	18	7.10	5.95
base station	4.30	6.83			

Special measurement:

TBUITEN: remote placed outside room with door closed.

F.8 Room 11.21 in Electrical Faculty Building

One 57-59 GHz measurement series at 20 postitions.
Base station: Centrally placed biconical horn at 2.75 m height.
Remote : Biconical horn at 1.38 m height.

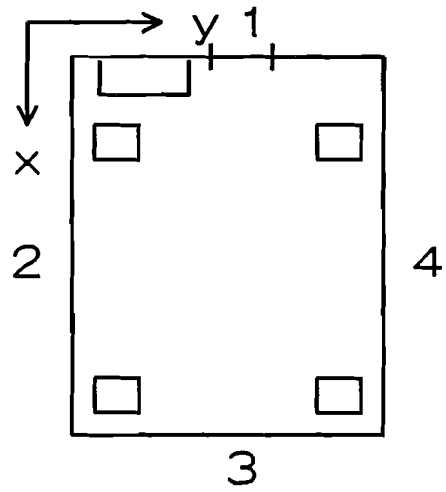

Figure F.8: Layout Room 11.21

Size (h*w*l)	: 3.07 m * 7.30 m * 11.30 m
Floor	: linoleum on concrete
Ceiling	: aluminium profiles
Walls 1,2 and 4	: smooth plastered concrete
Wall 1	: glass windows in steel frame

Measurement positions:

Position	x (m)	y (m)	Position	x (m)	y (m)
1	1.23	1.12	11	6.13	4.40
2	1.11	2.78	12	7.09	6.63
3	0.18	3.57	13	7.18	4.75
4	0.23	6.70	14	7.15	0.54
5	1.45	3.88	15	7.12	2.15
6	2.80	3.88	16	7.77	3.25
7	4.11	4.49	17	9.60	4.03
8	4.53	6.01	18	9.62	5.65
9	4.02	2.47	19	9.59	2.66
10	3.37	1.42	20	9.59	1.40
base station	5.45	3.65			

G Measured Average Power Delay Profiles for all Series

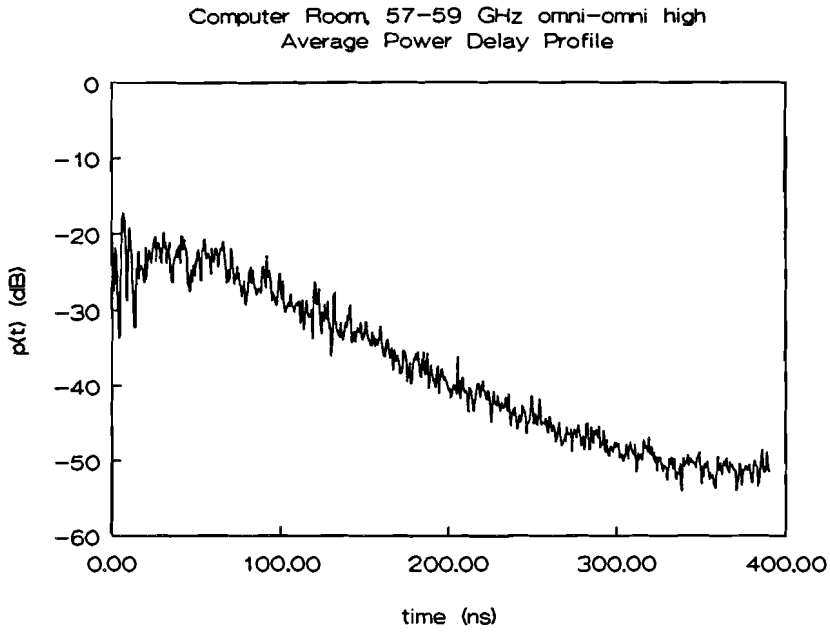

Figure G.1

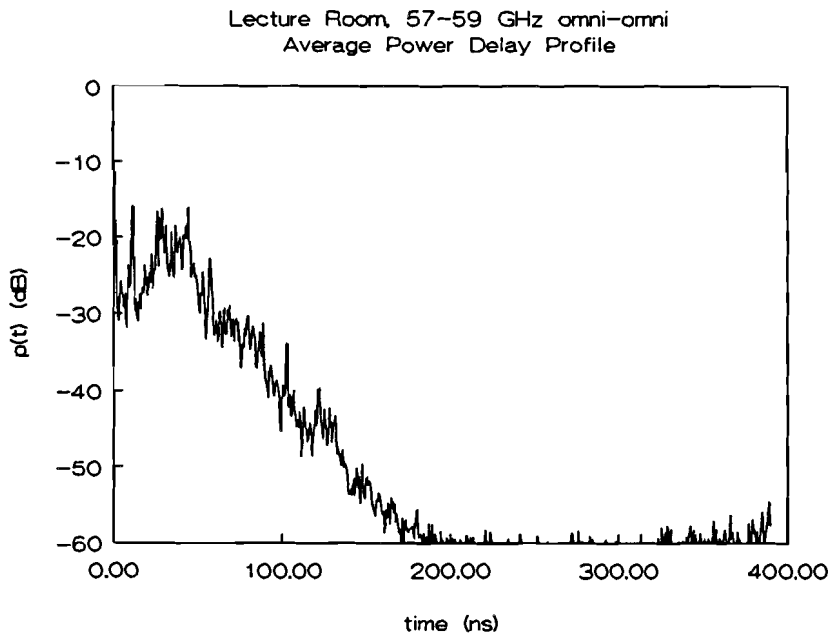

Figure G.2

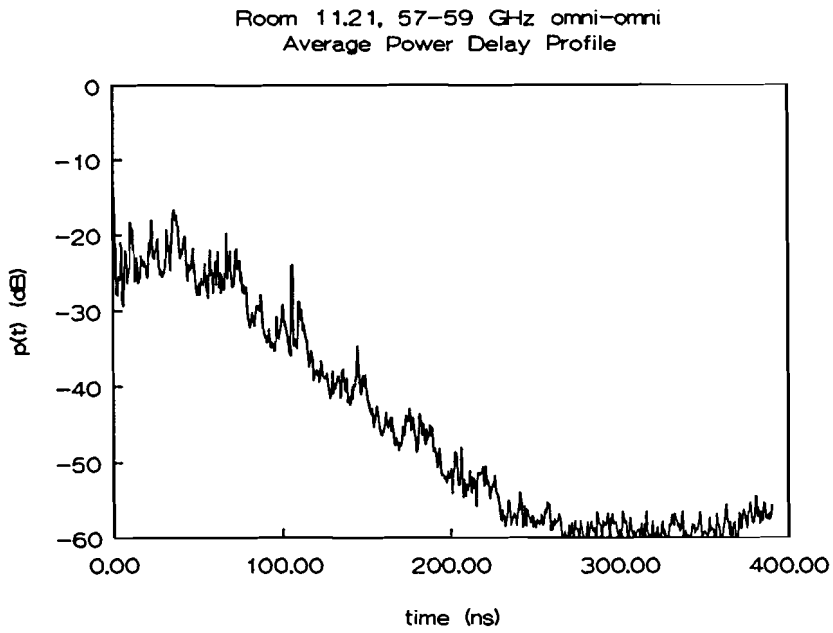

Figure G.3

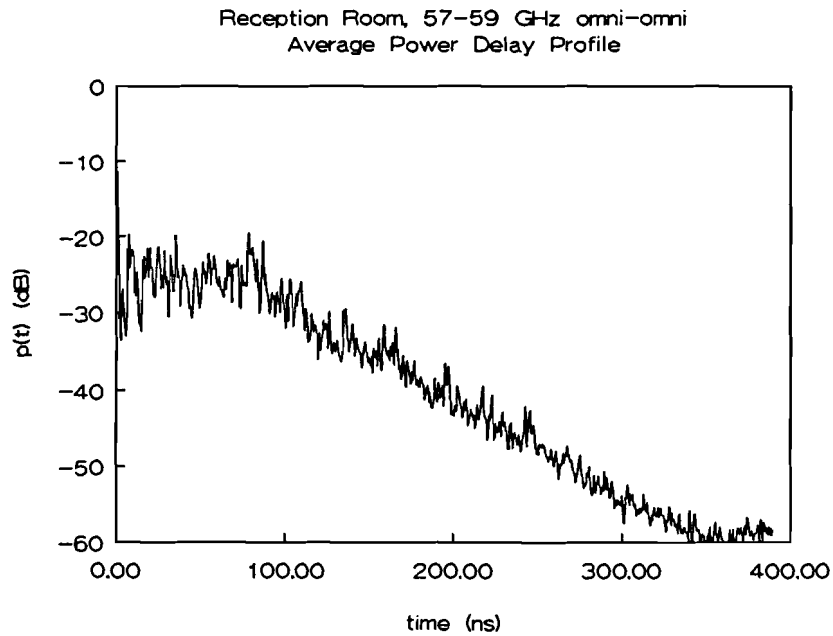

Figure G.4

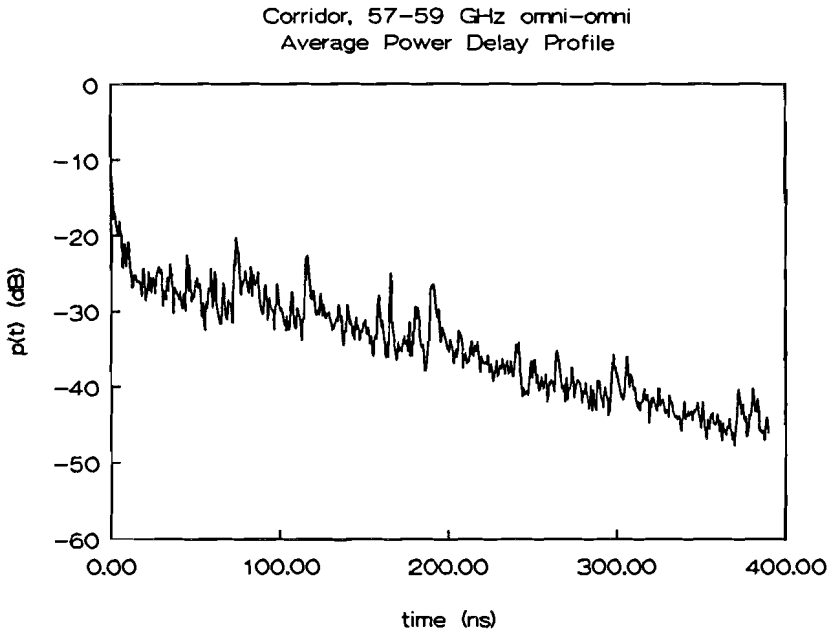

Figure G.5

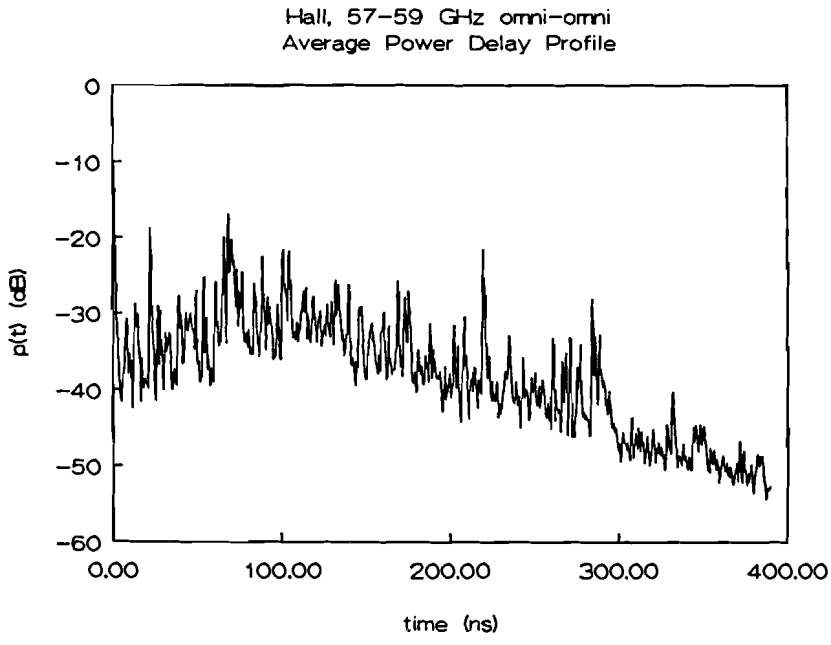

Figure G.6

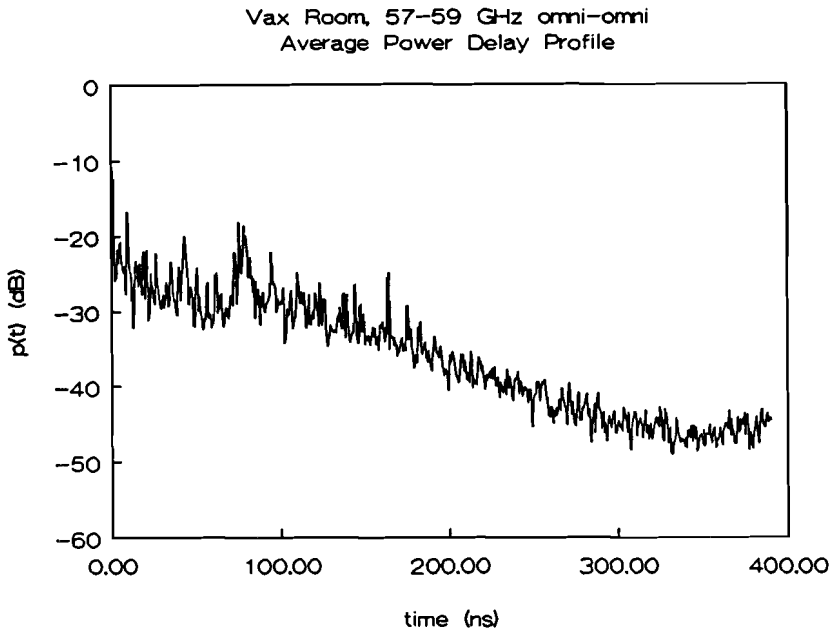

Figure G.7

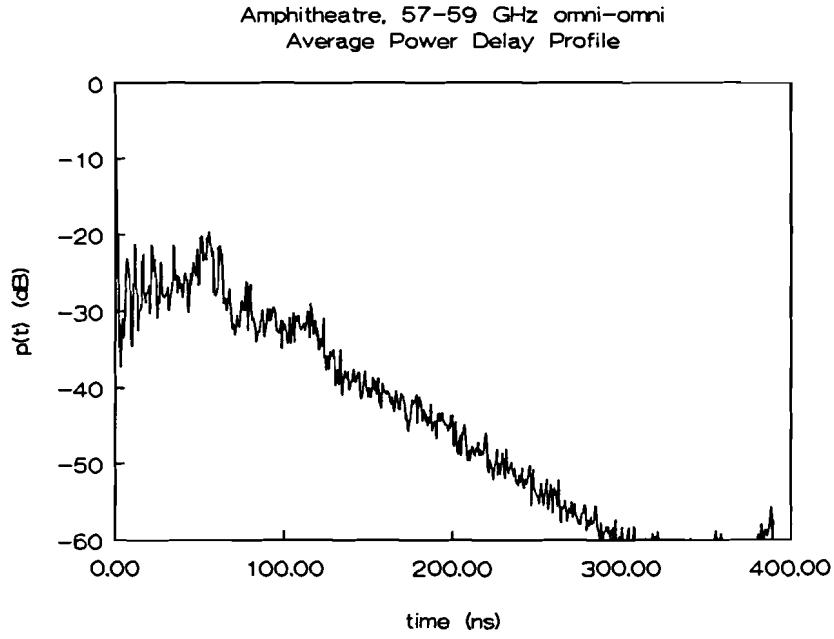

Figure G.8

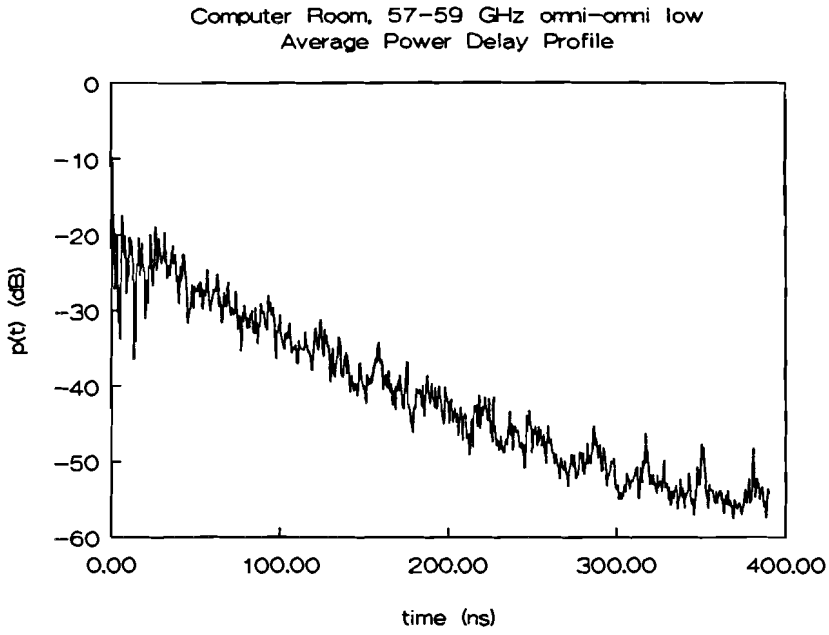

Figure G.9

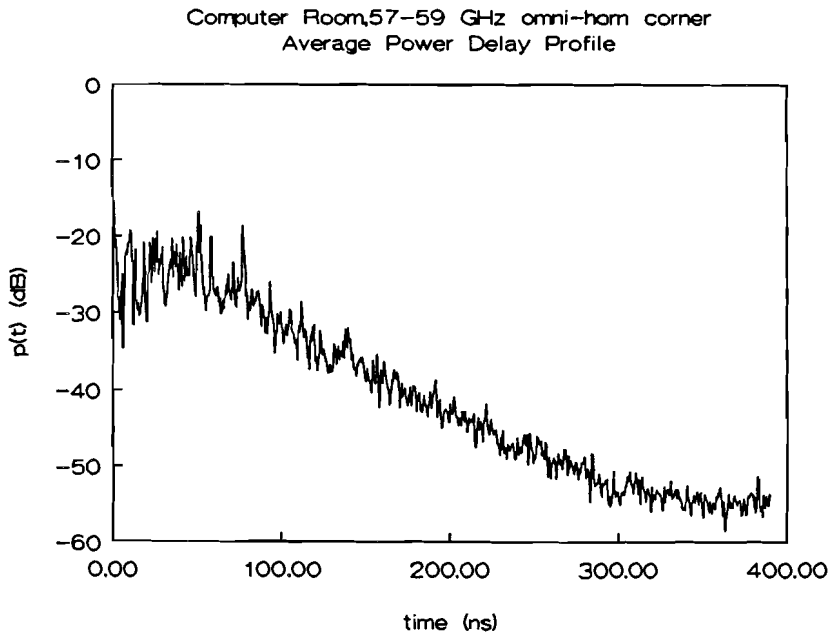

Figure G.10

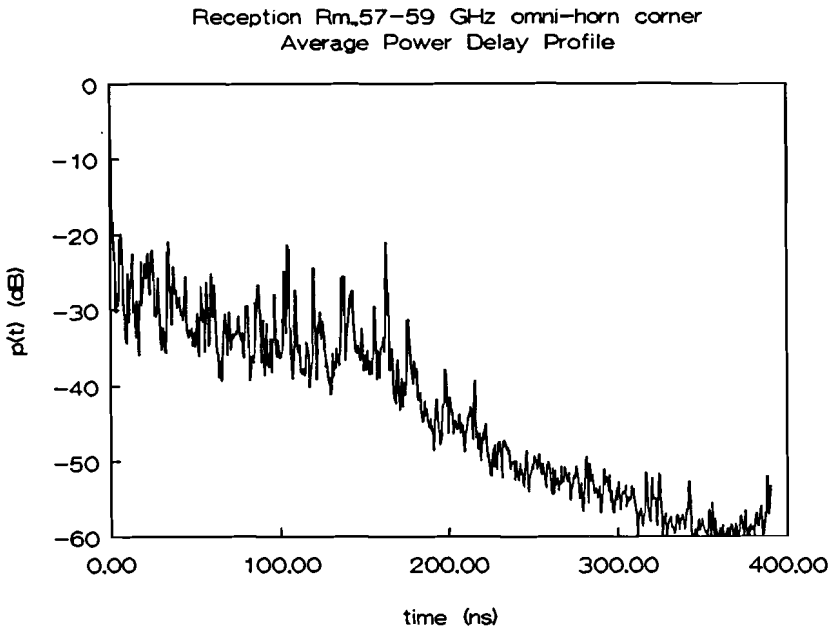

Figure G.11

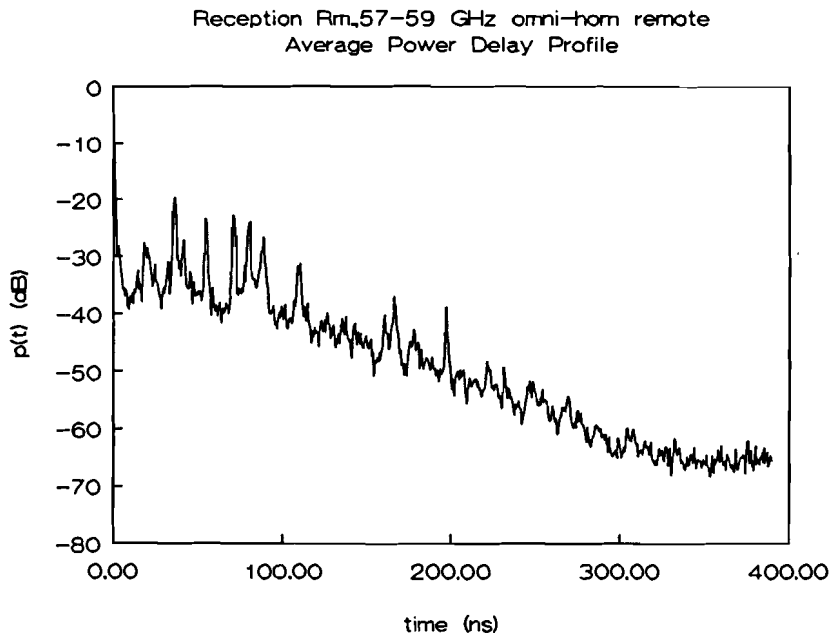

Figure G.12

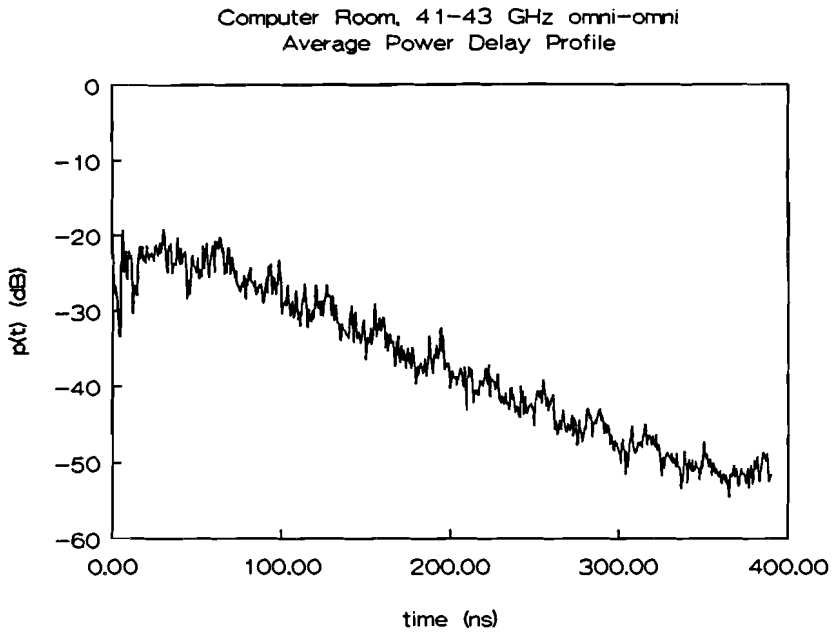

Figure G.13

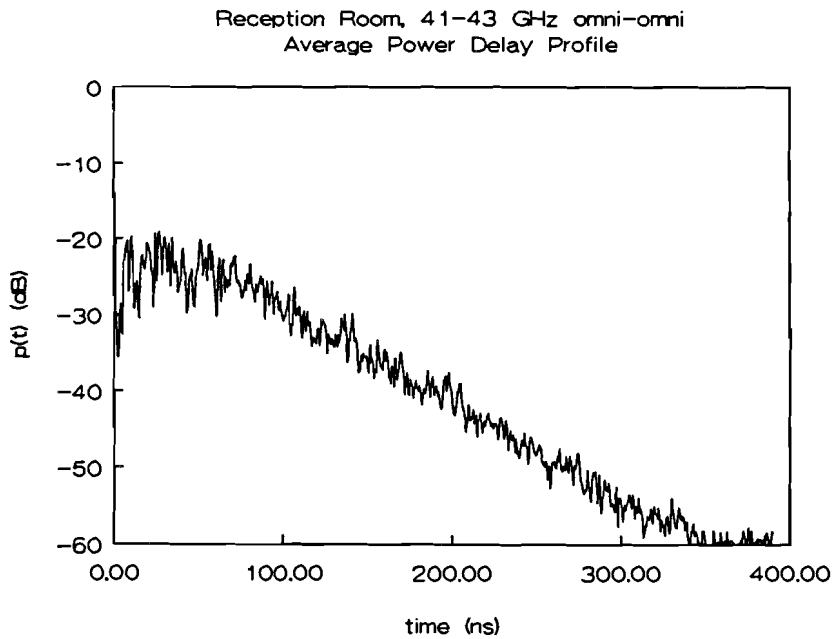

Figure G.14

H Power versus LOS Distance for all Series

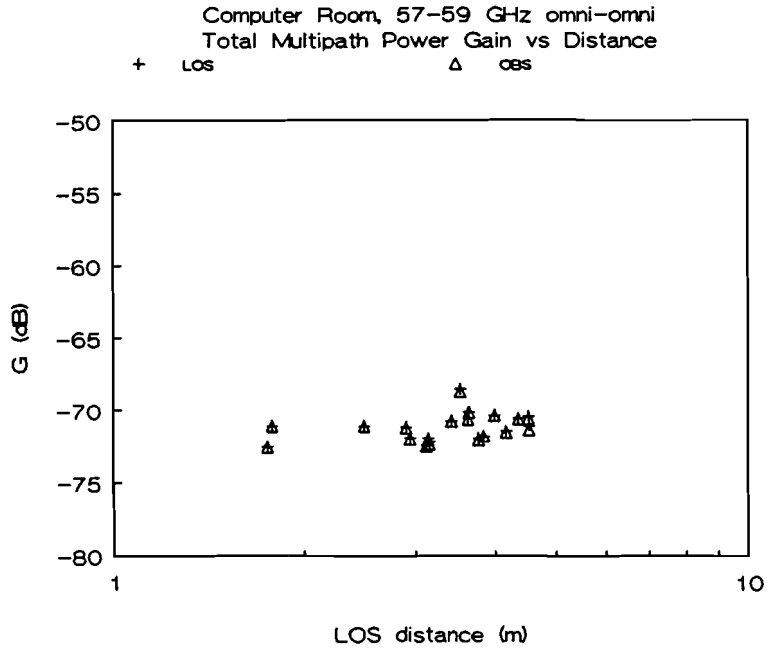

Figure H.1

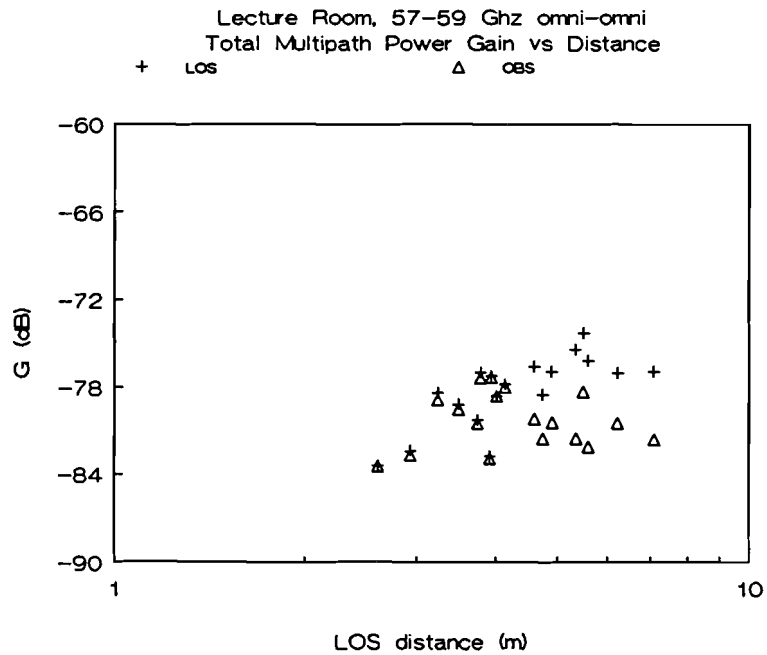

Figure H.2

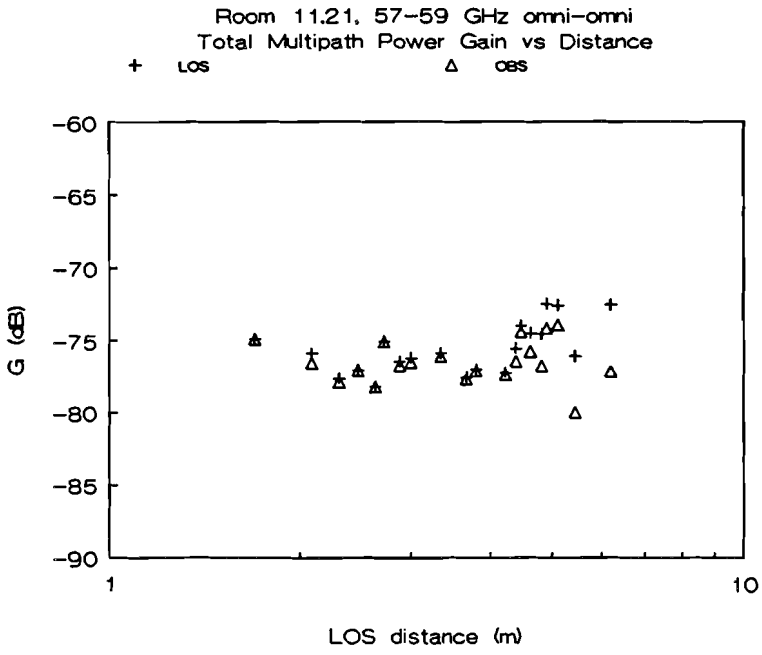

Figure H.3

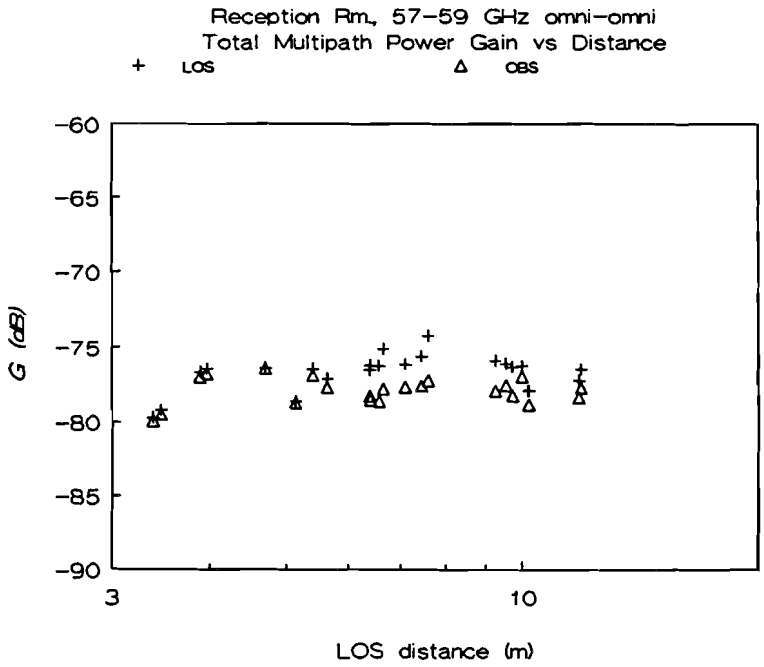

Figure H.4

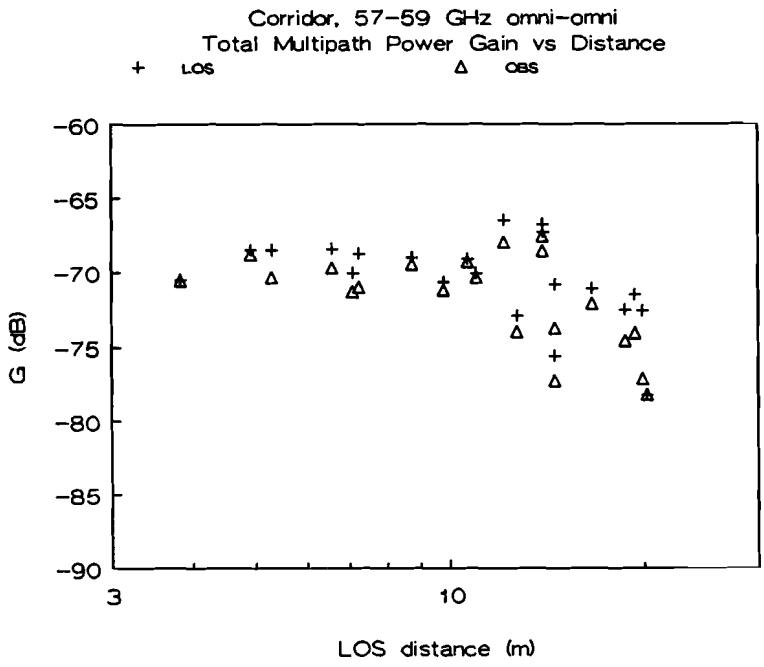

Figure H.5

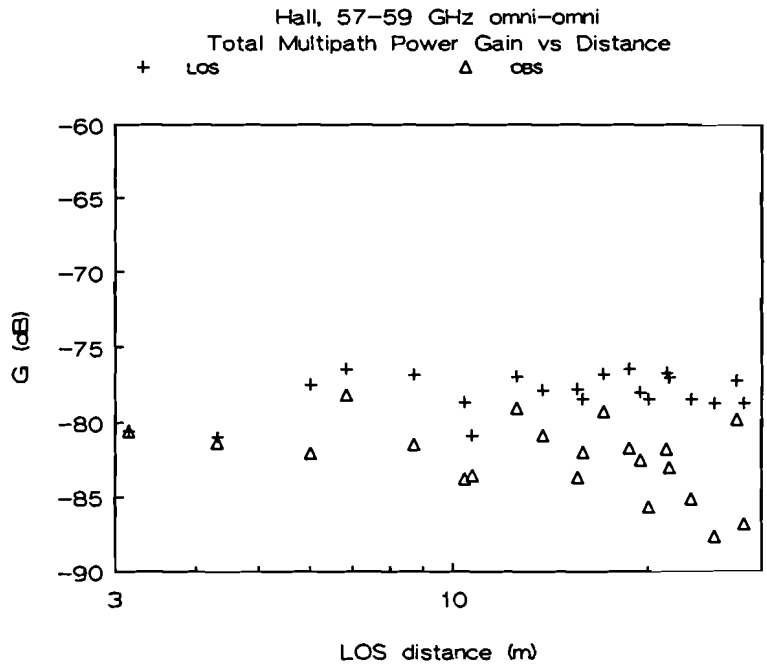

Figure H.6

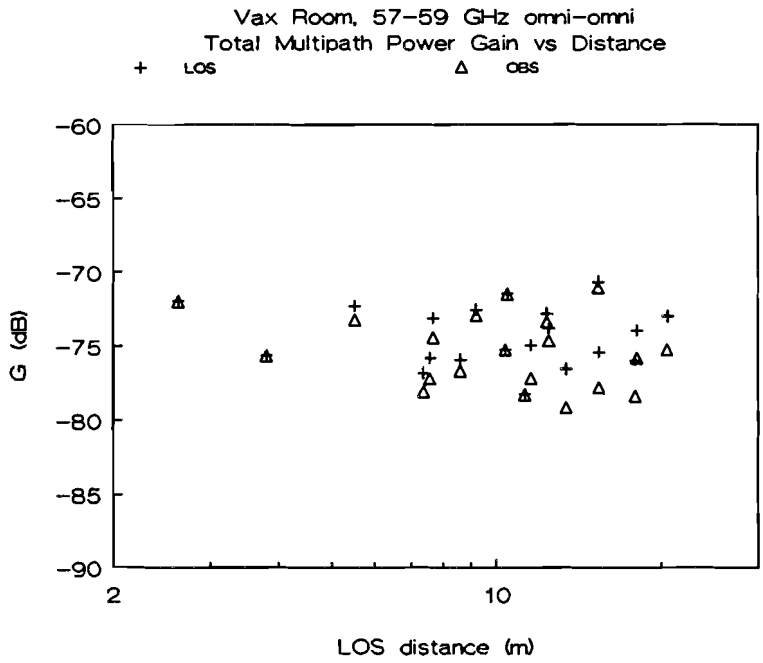

Figure H.7

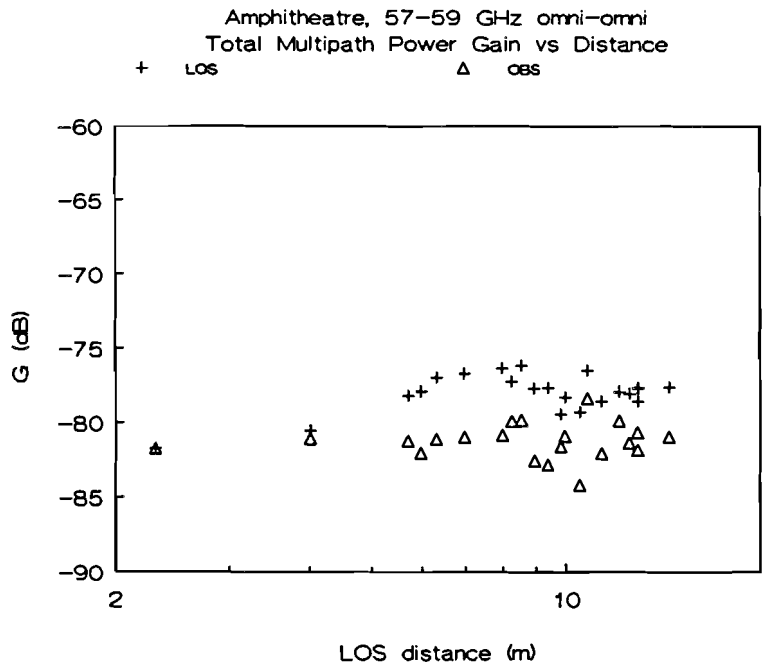

Figure H.8

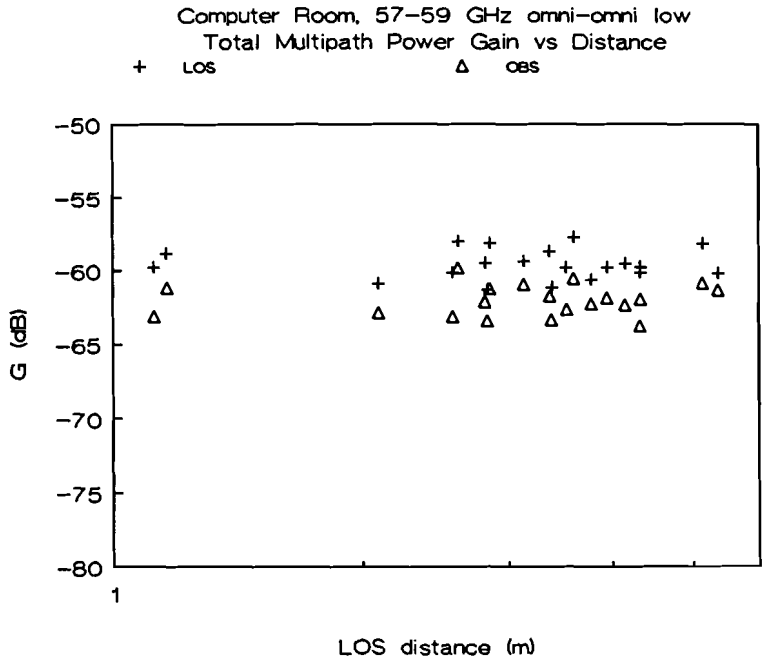

Figure H.9

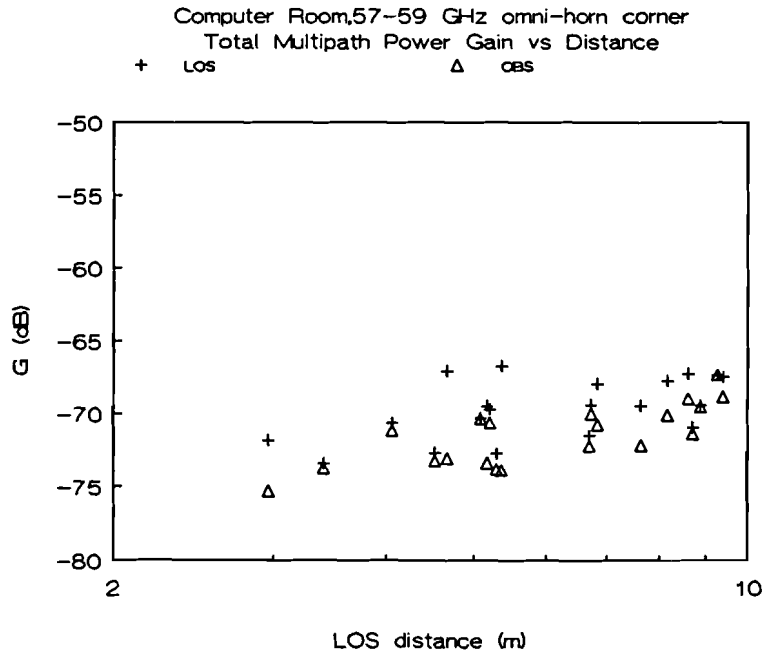

Figure H.10

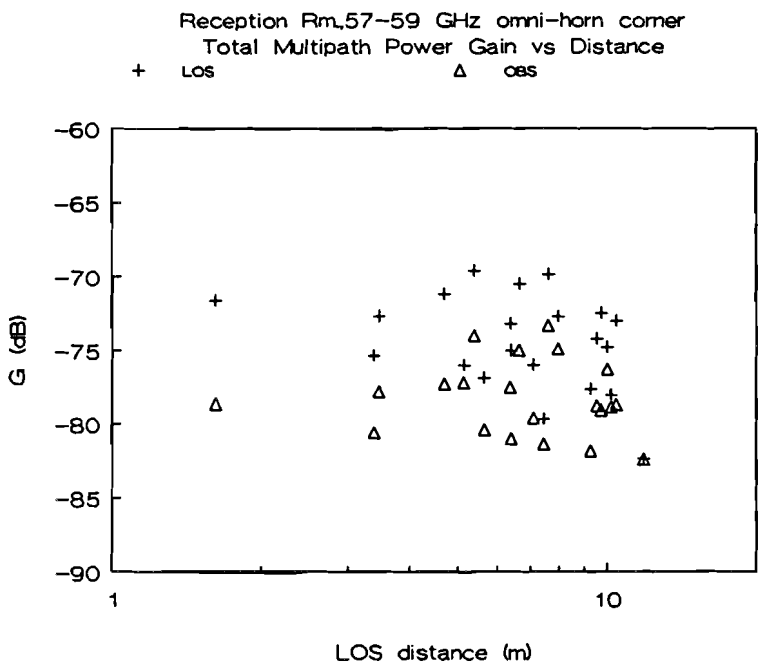

Figure H.11

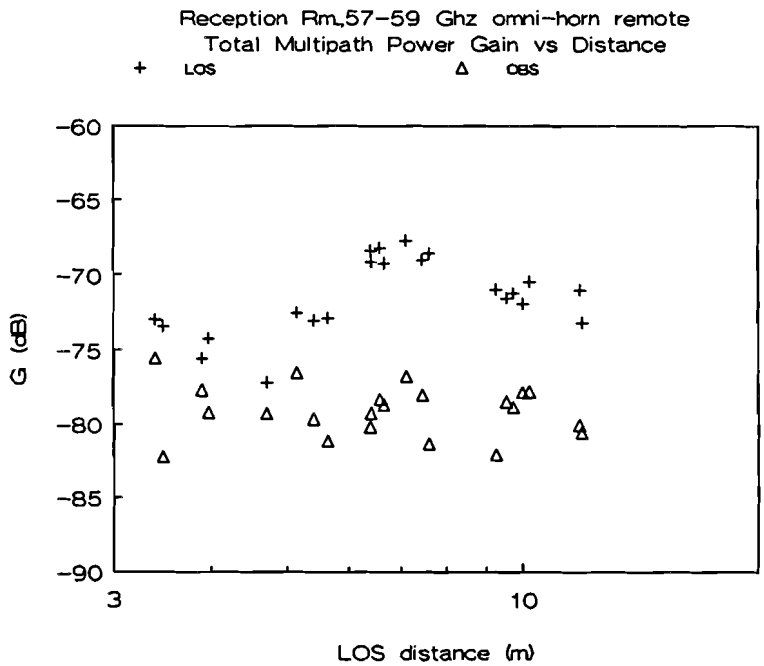

Figure H.12

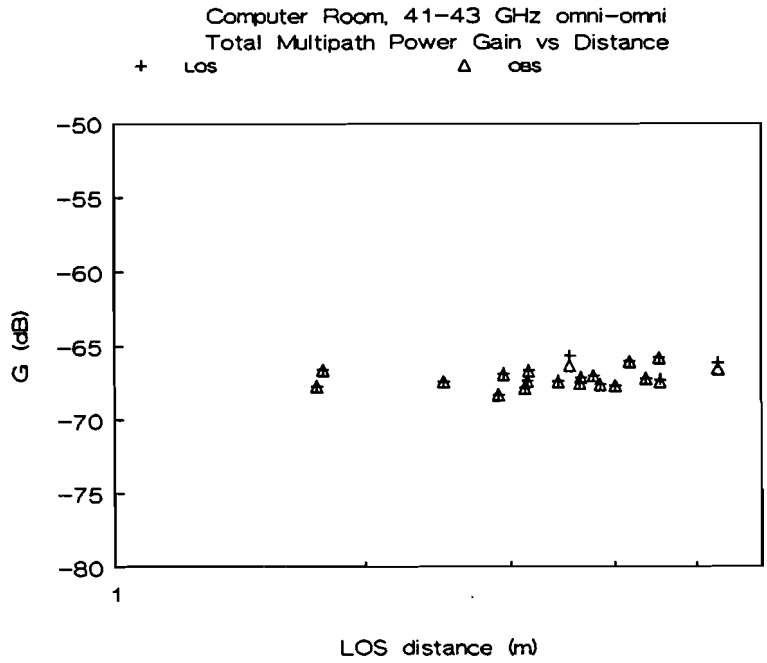

Figure H.13

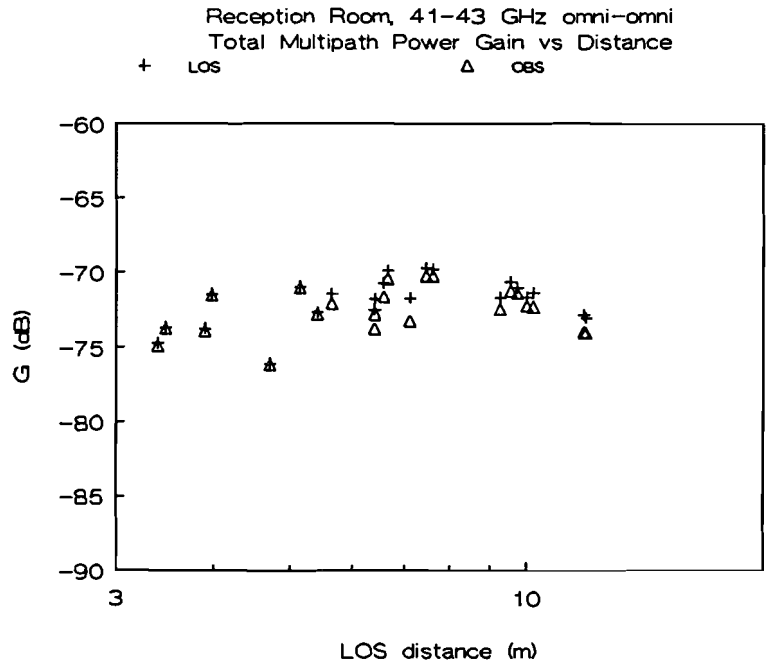

Figure H.14

I Time Delay Spread versus LOS Distance for all Series

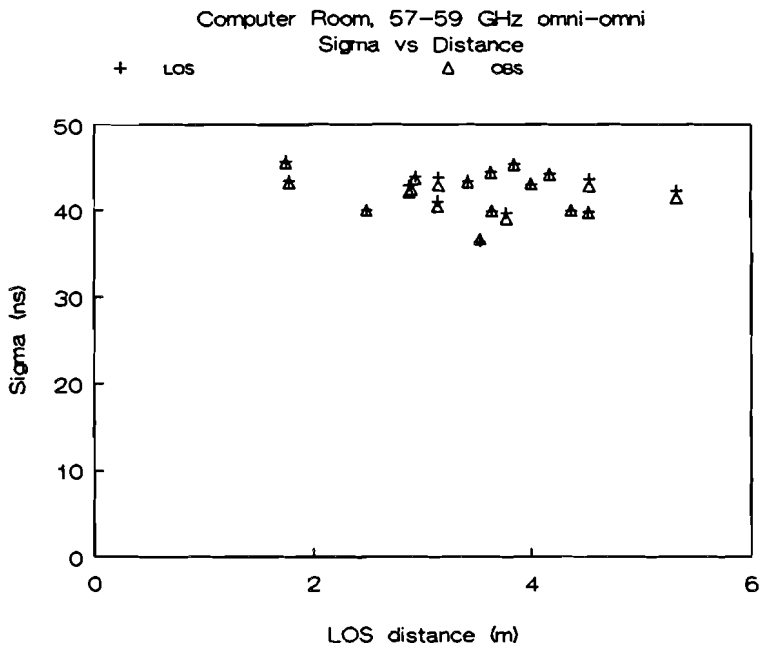

Figure I.1

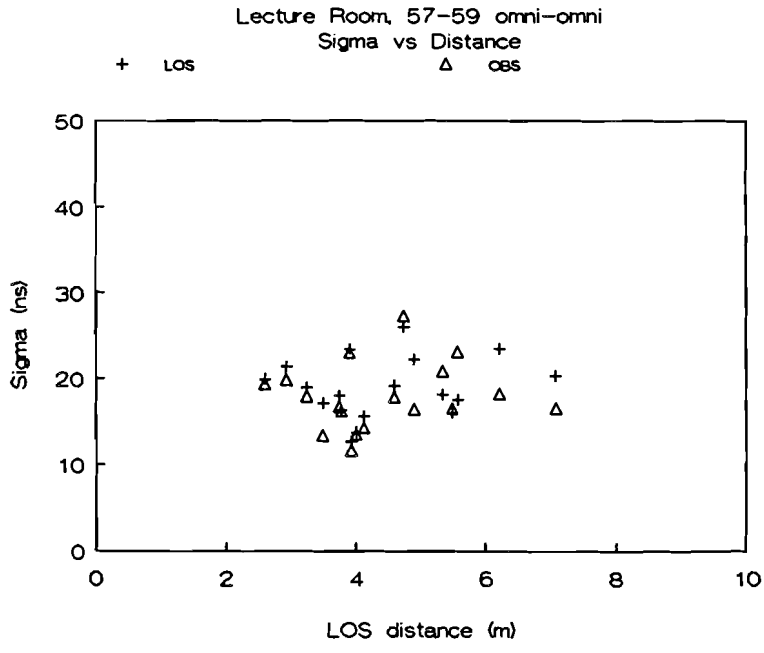

Figure I.2

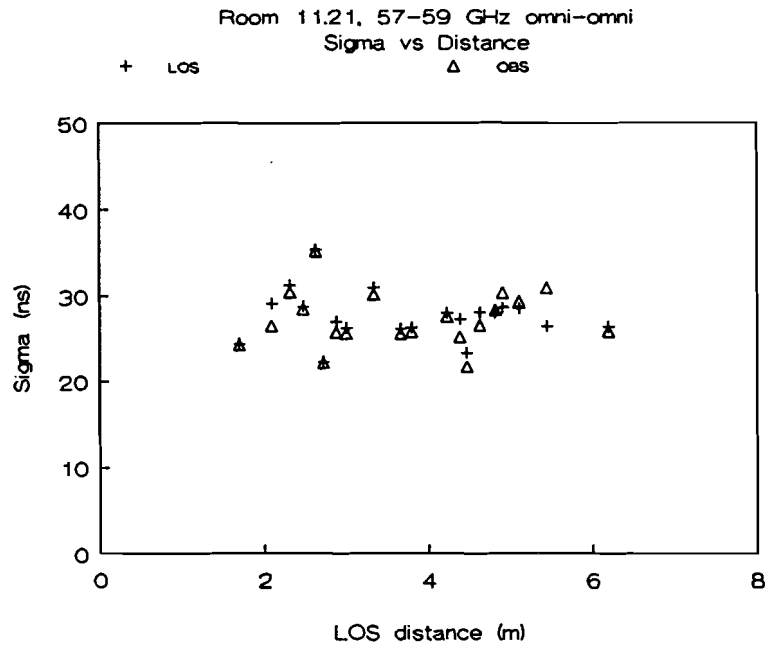

Figure I.3

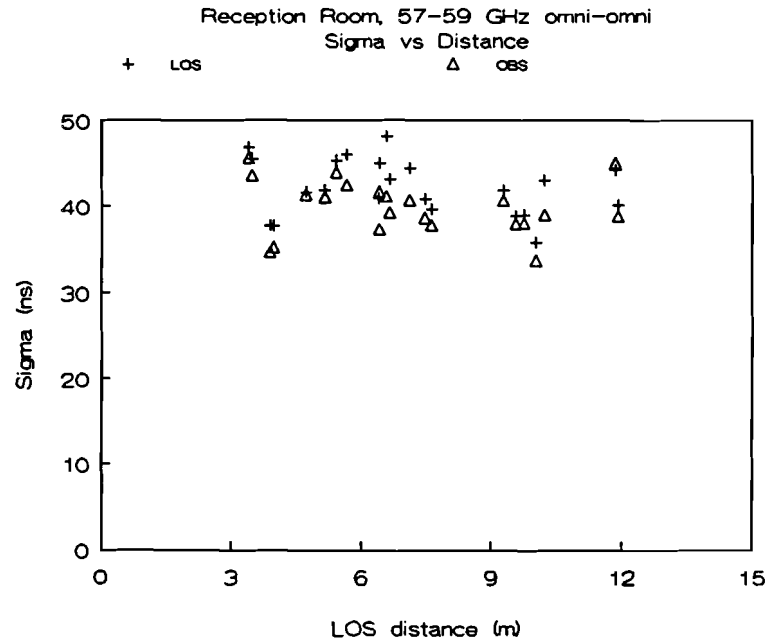

Figure I.4

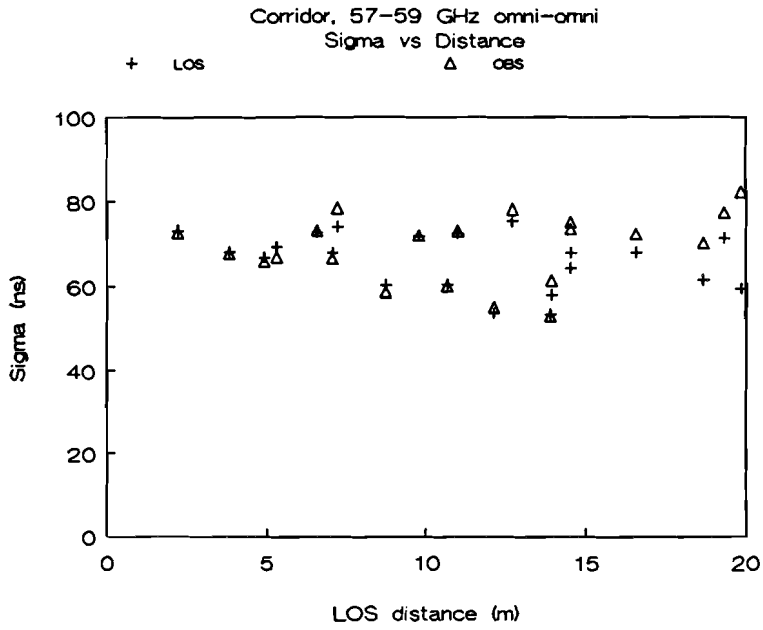

Figure I.5

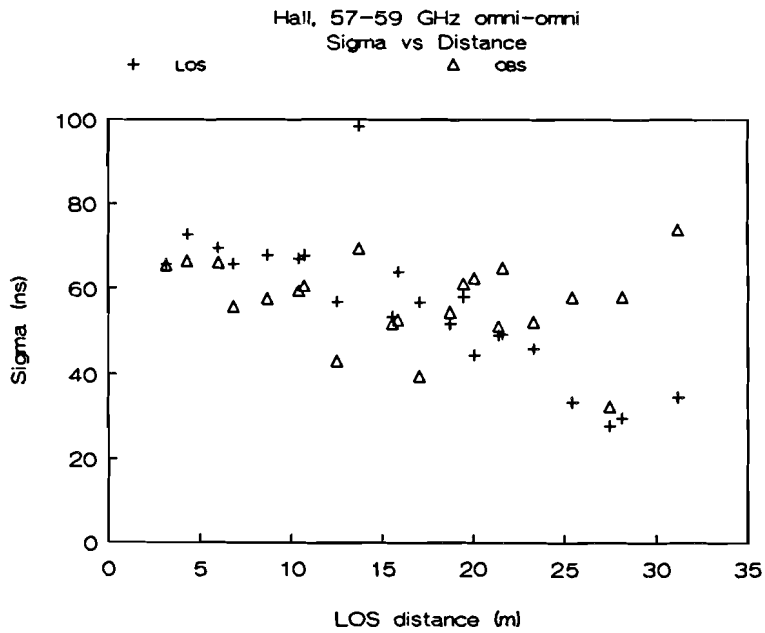

Figure I.6

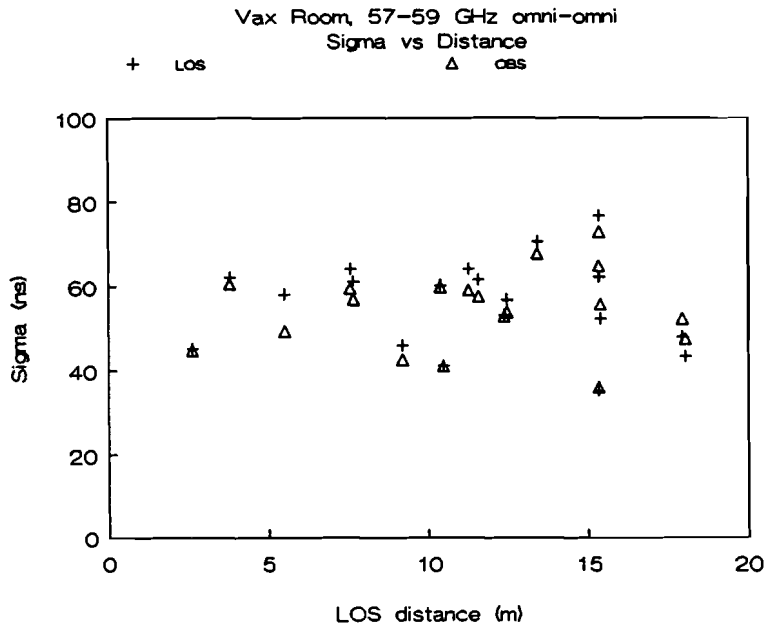

Figure I.7

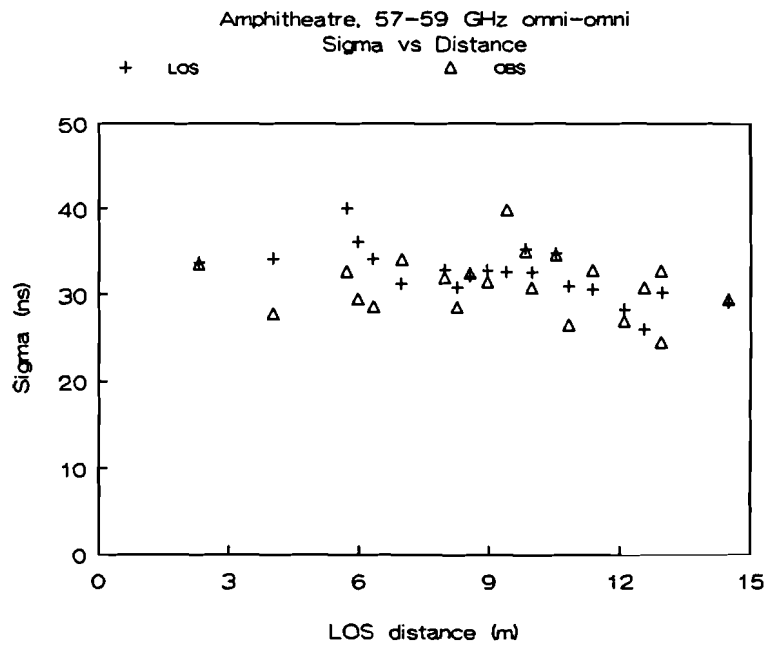

Figure I.8

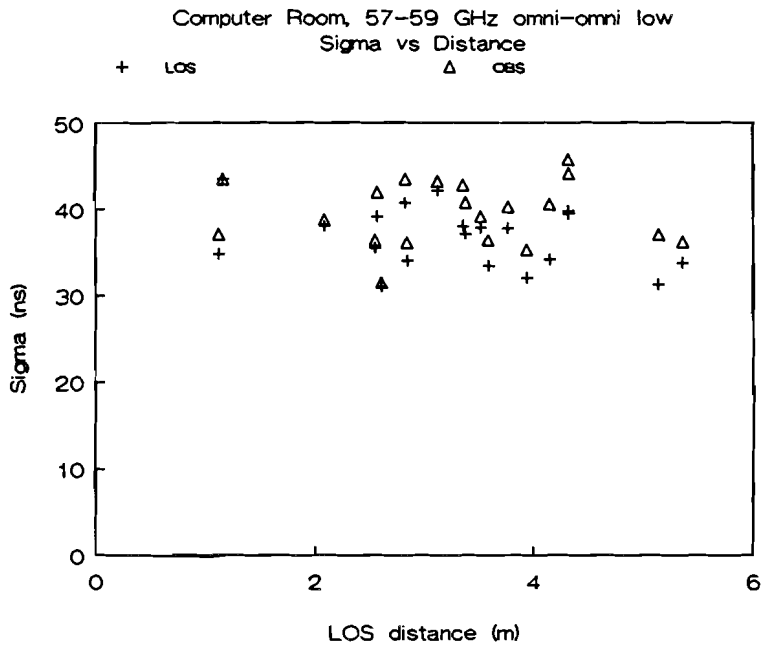

Figure I.9

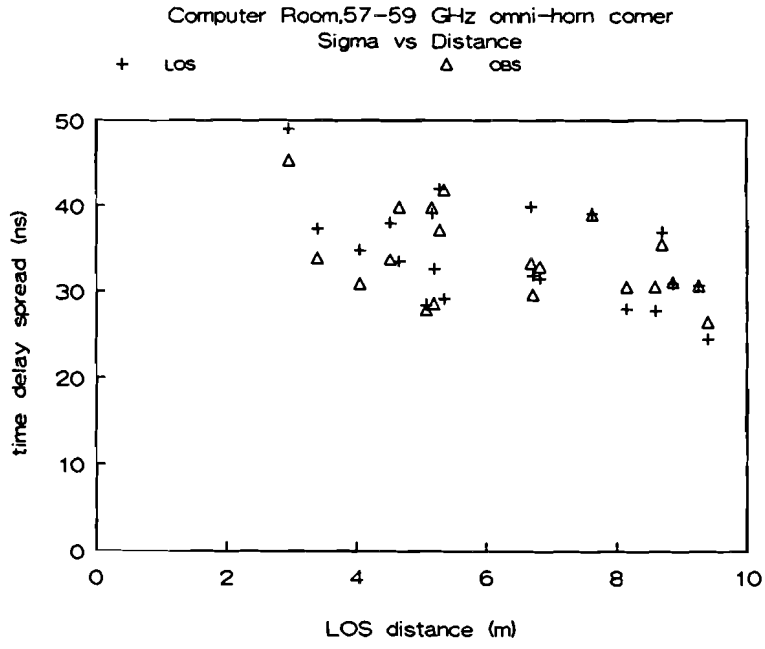

Figure I.10

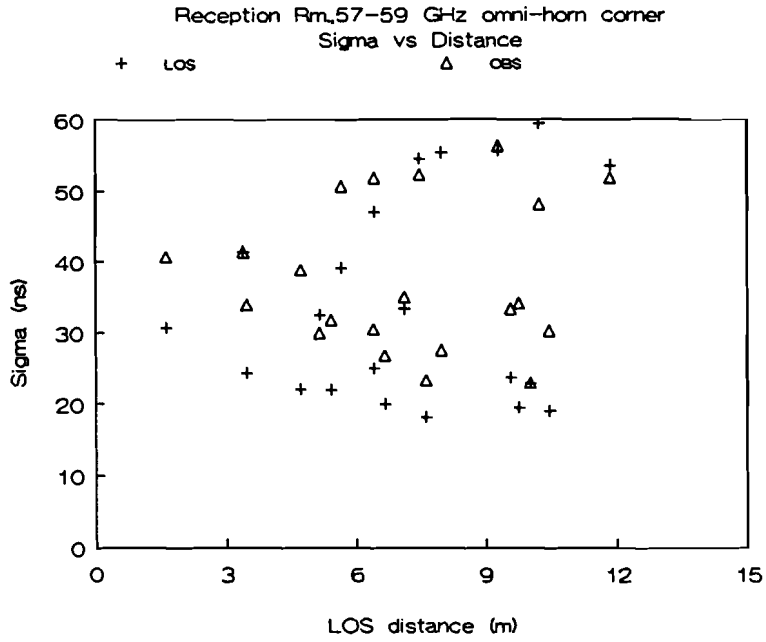

Figure I.11

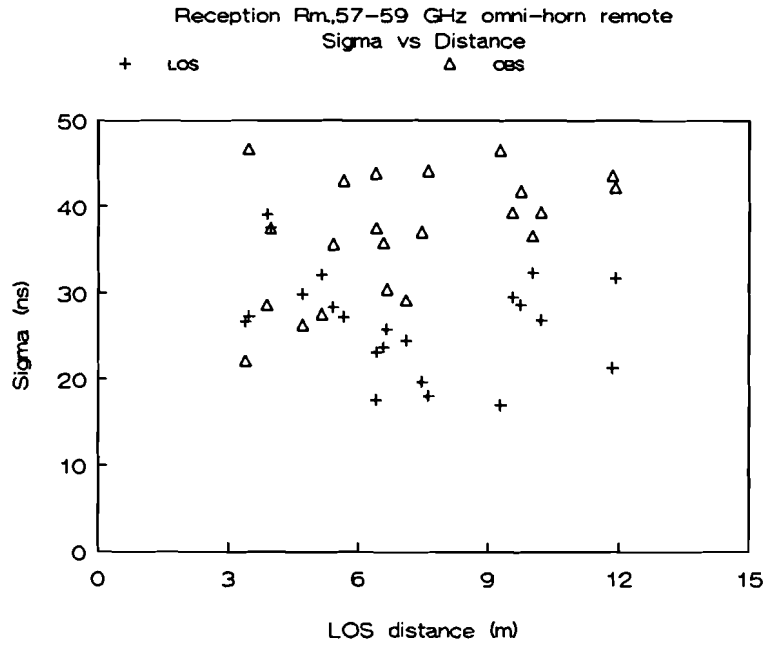

Figure I.12

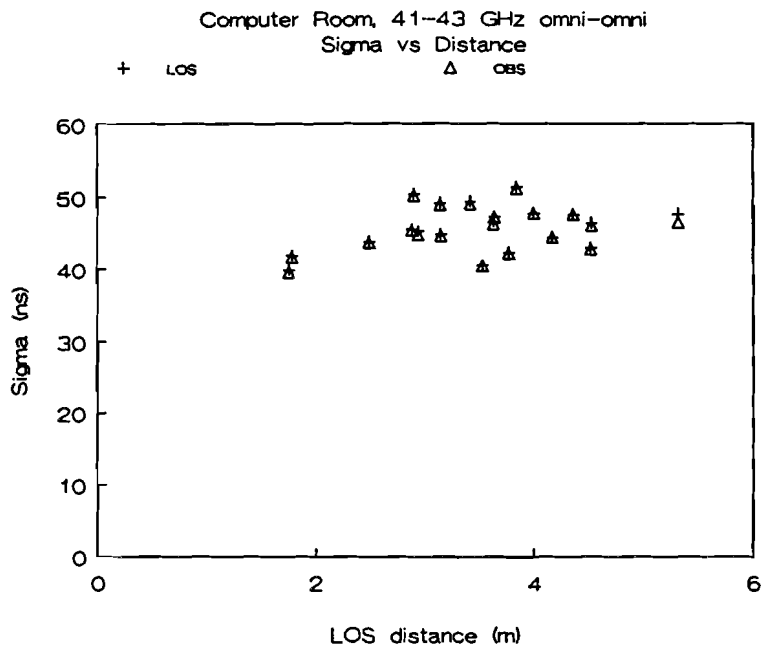

Figure I.13

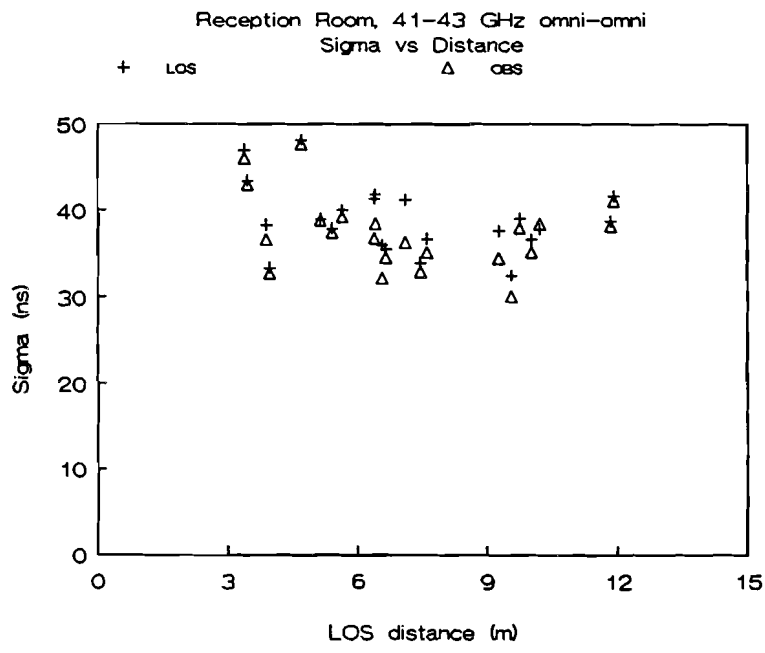

Figure I.14

J Interarrival Distributions for all Series

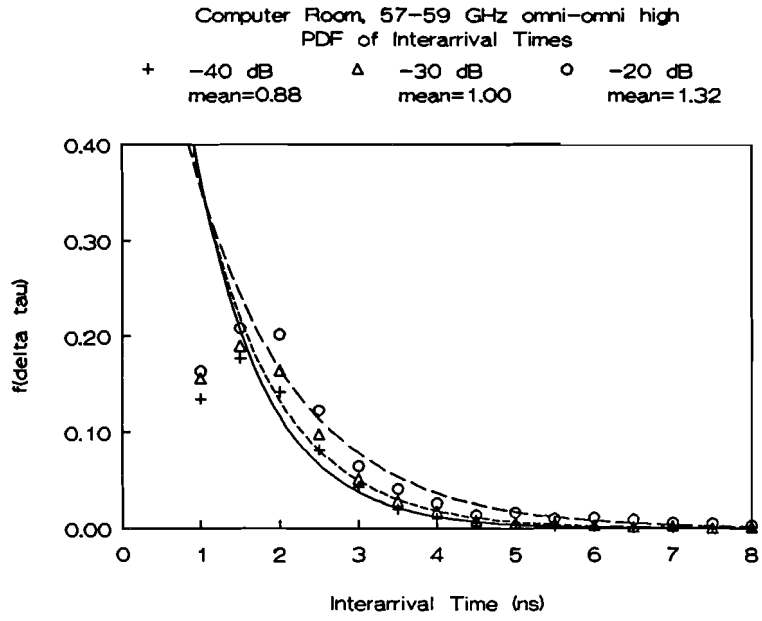

Figure J.1

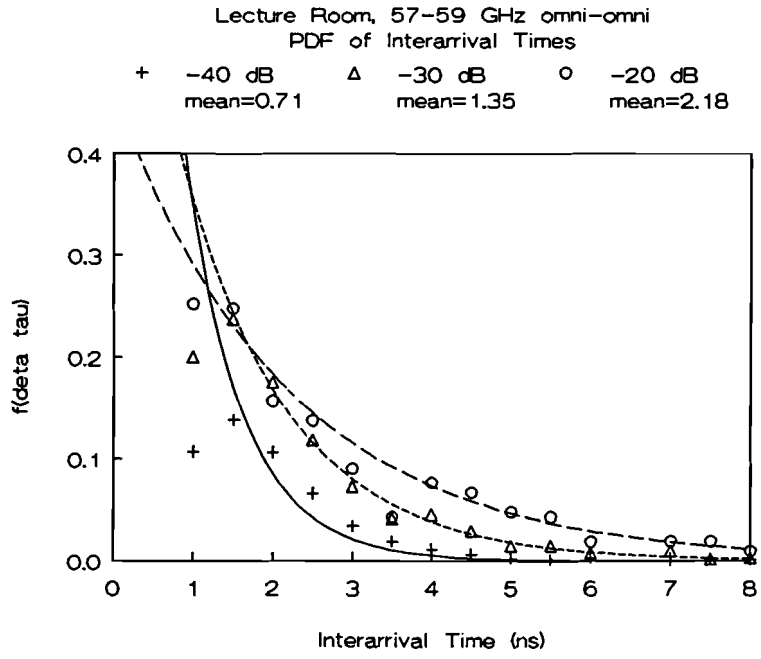

Figure J.2

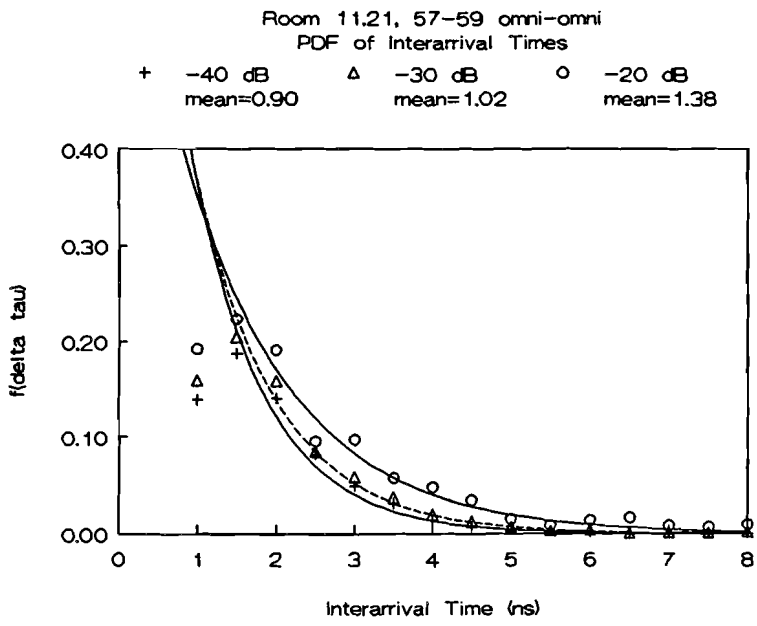

Figure J.3

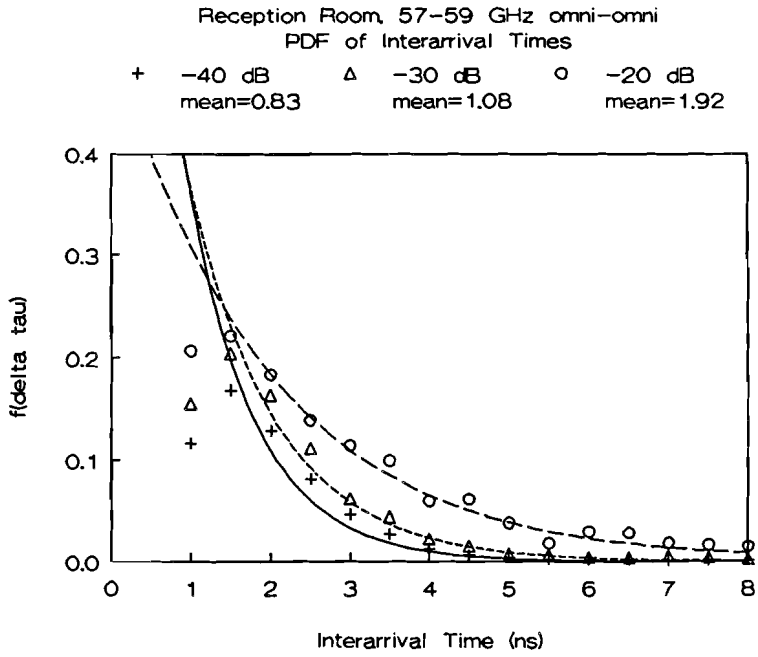

Figure J.4

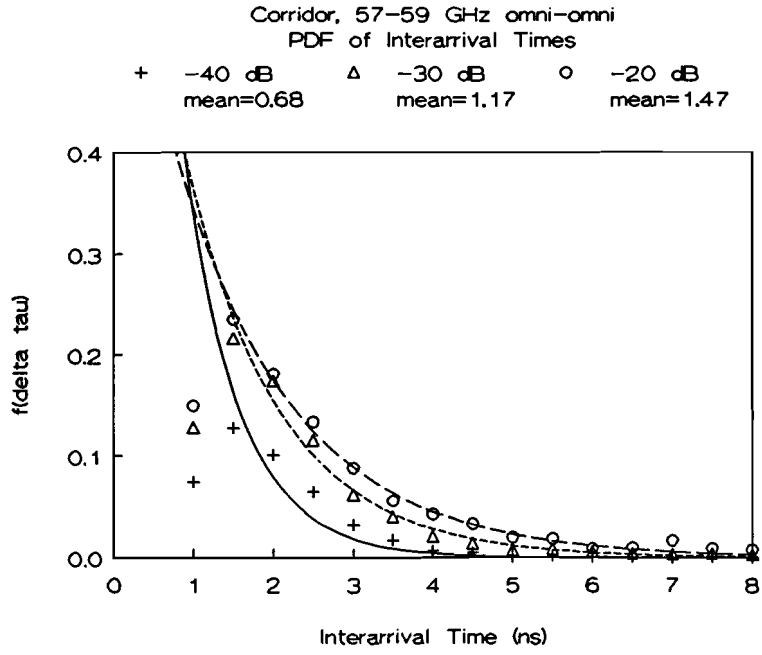

Figure J.5

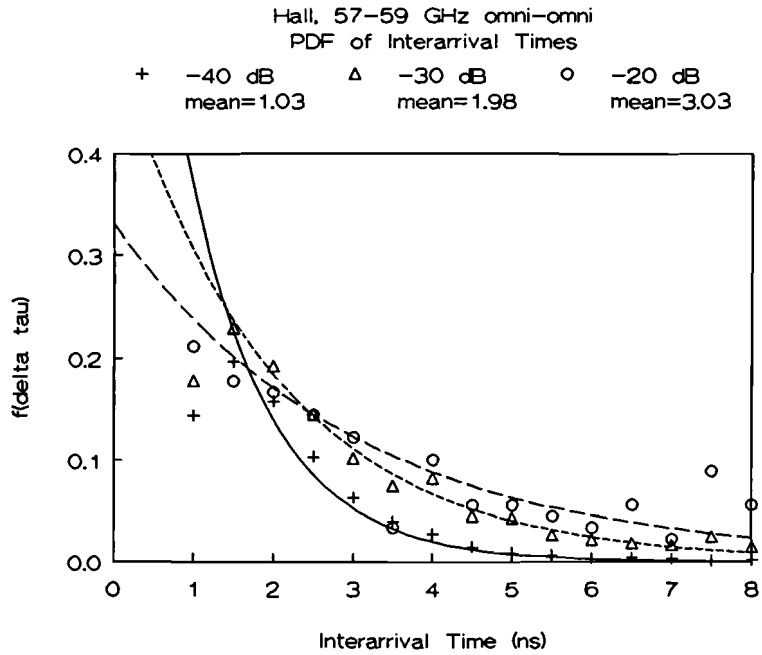

Figure J.6

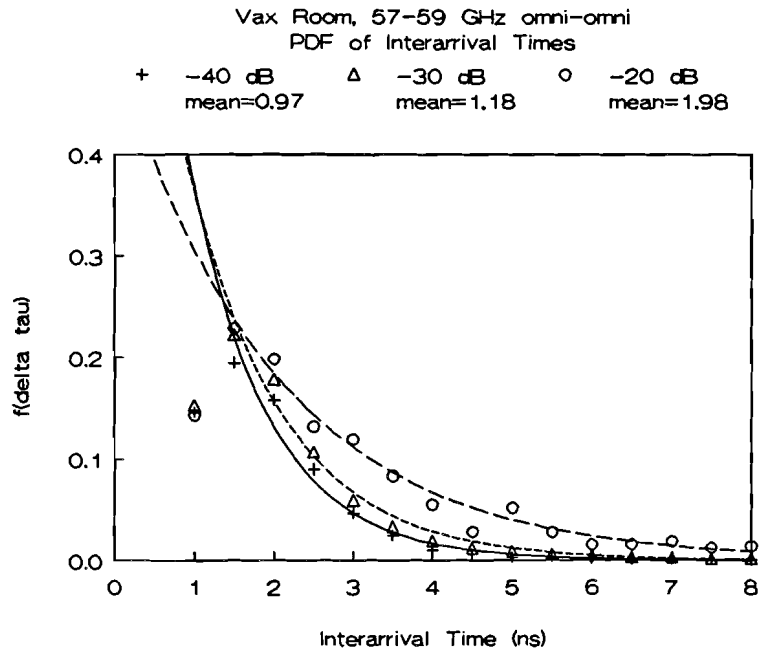

Figure J.7

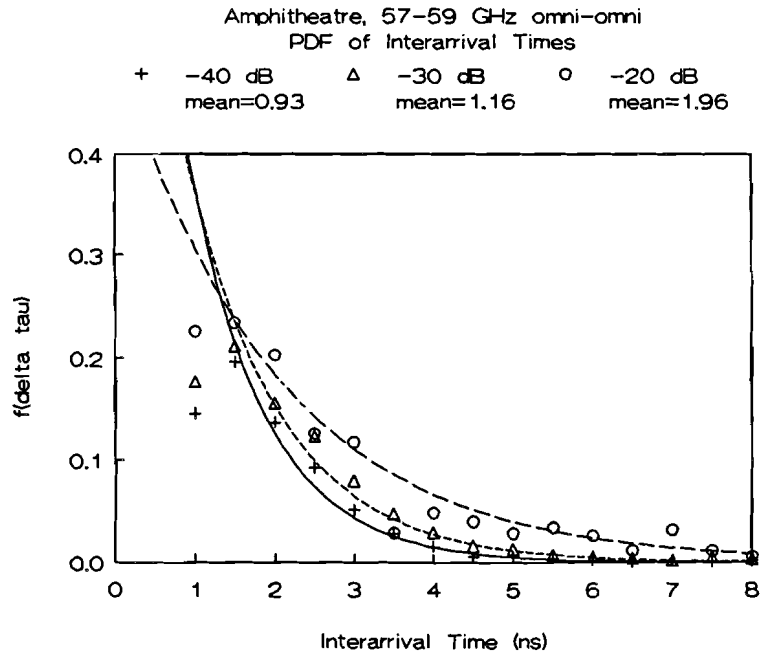

Figure J.8

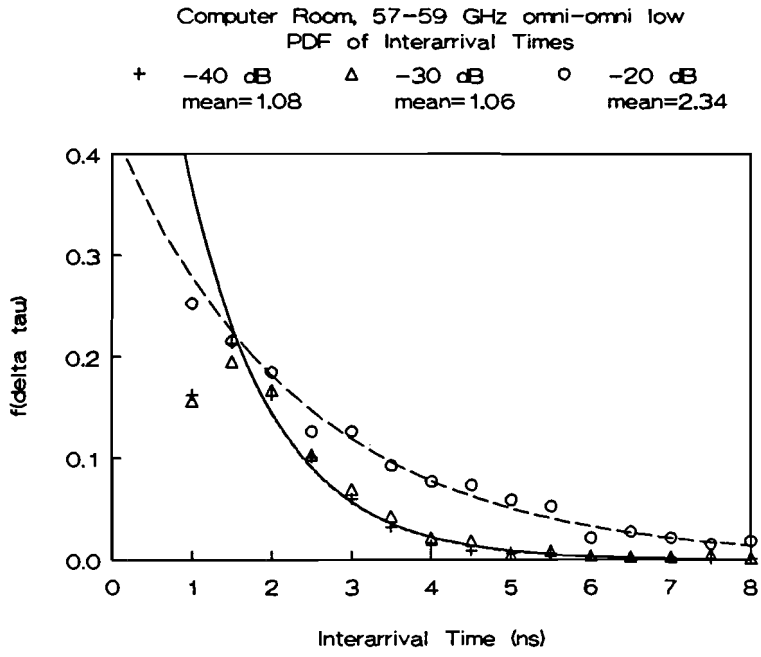

Figure J.9

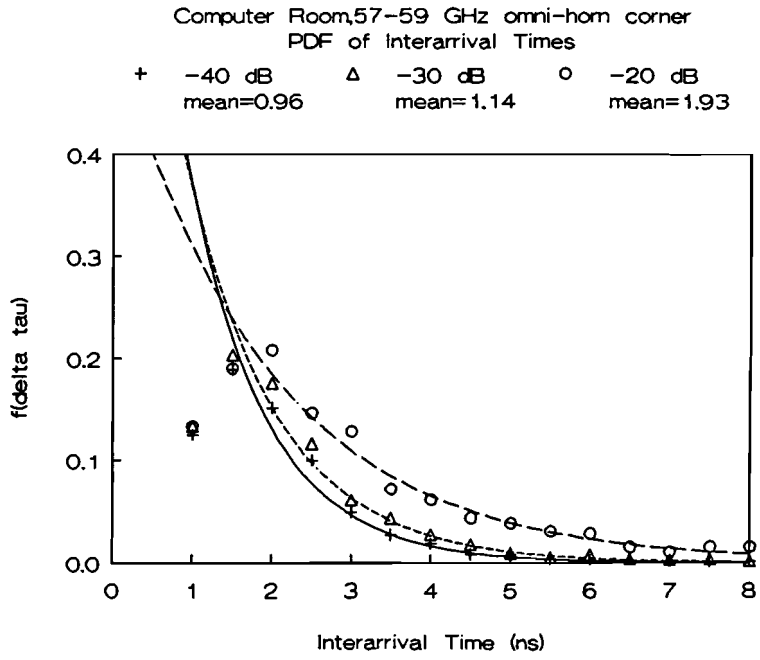

Figure J.10

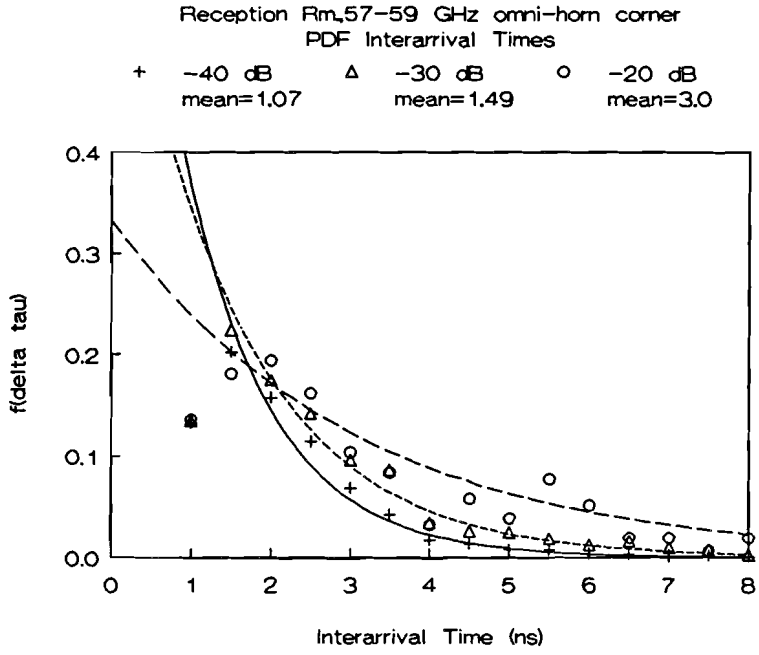

Figure J.11

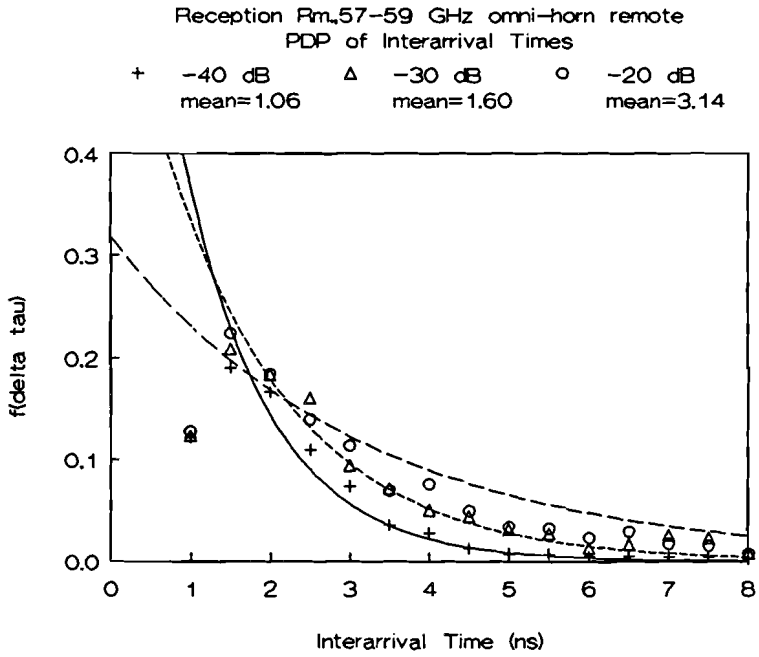

Figure J.12

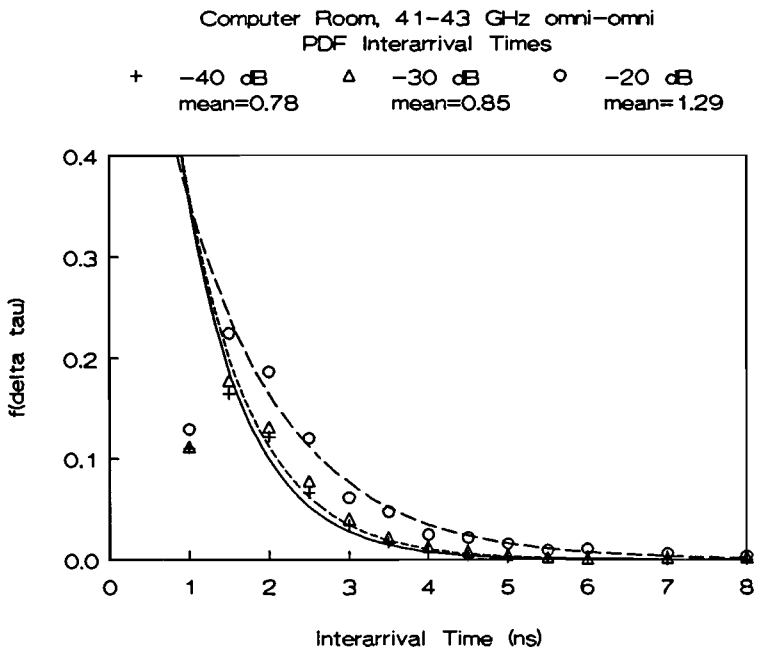

Figure J.13

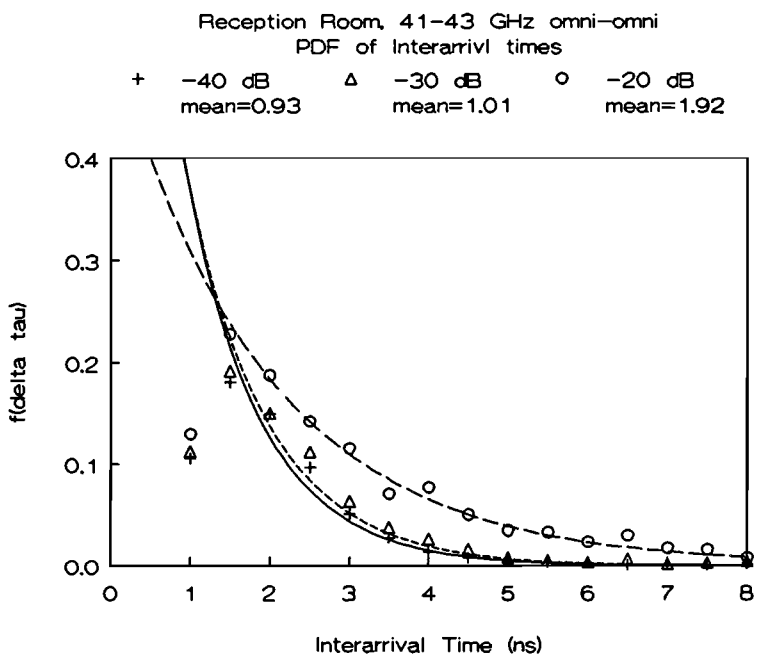

Figure J.14

K Comparison of Simulations and Measurements

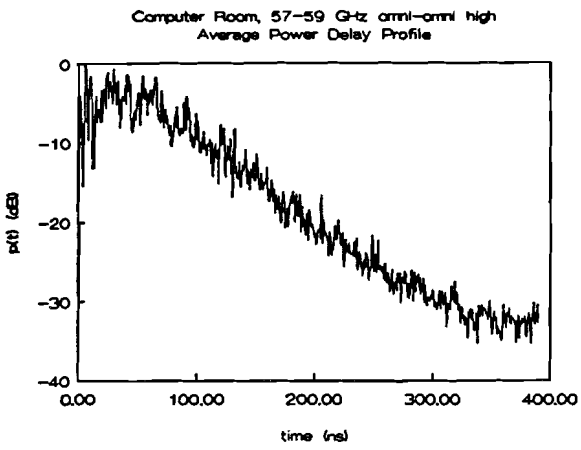

Figure K.1: Measurement

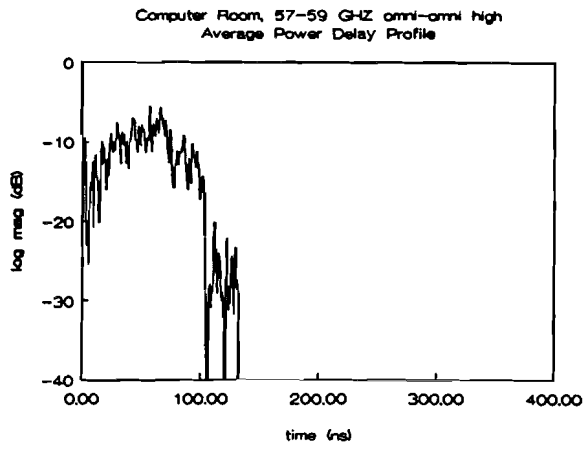

Figure K.2 : Simulation

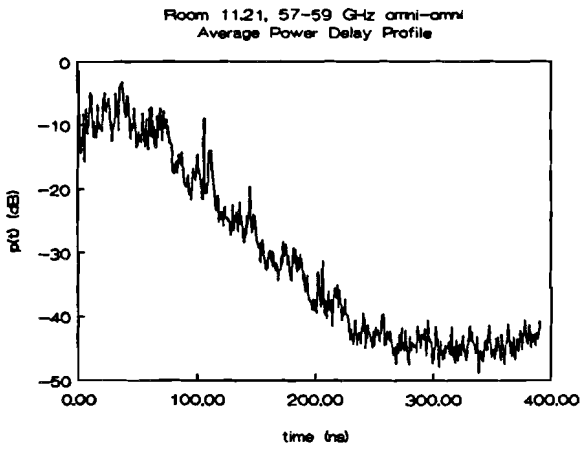

Figure K.3: Measurement

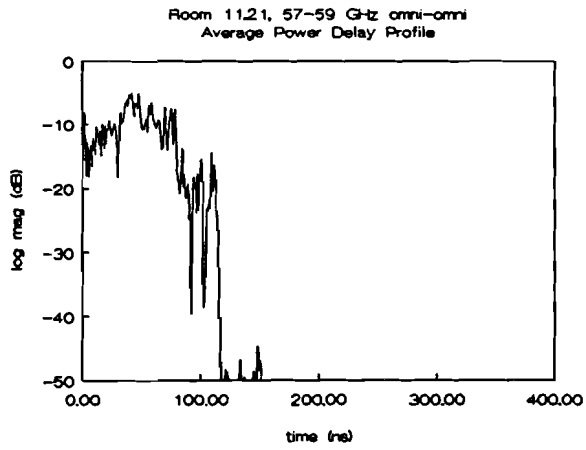

Figure K.4: Simulation

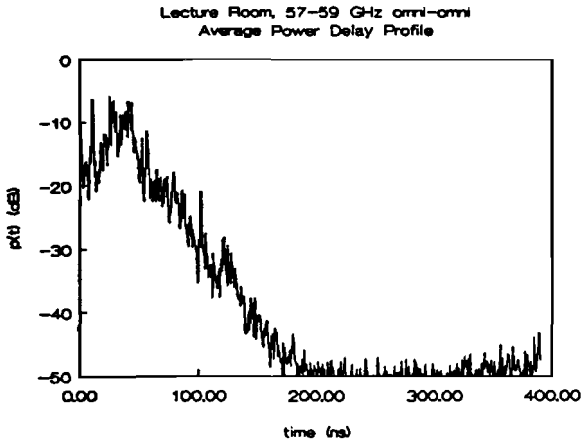

Figure K.5: Measurement

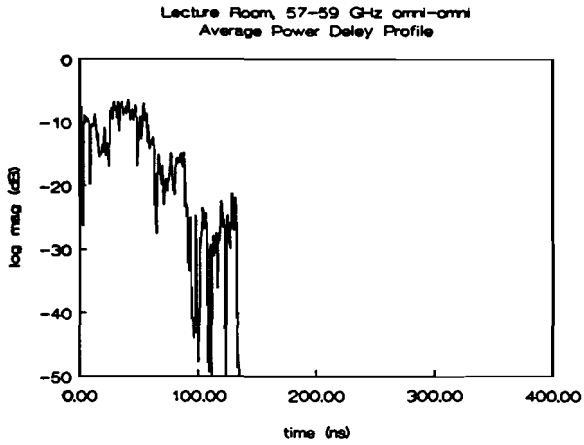

Figure K.6 : Simulation

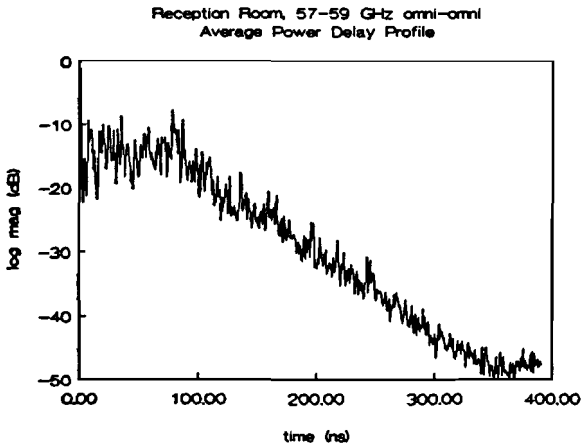

Figure K.7: Measurement

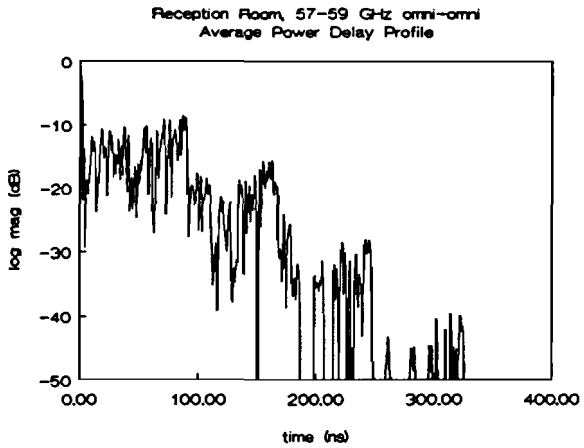

Figure K.8: Simulation

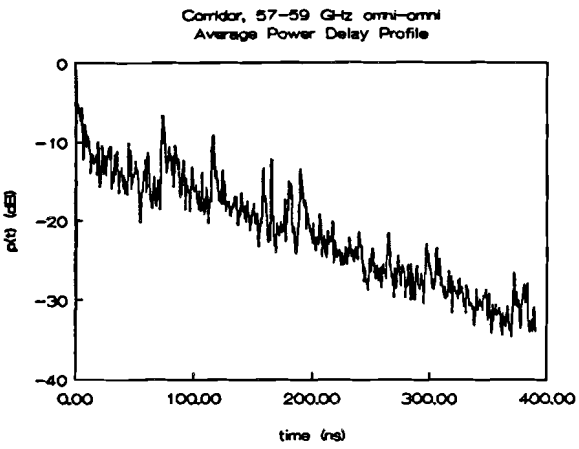

Figure K.9: Measurement

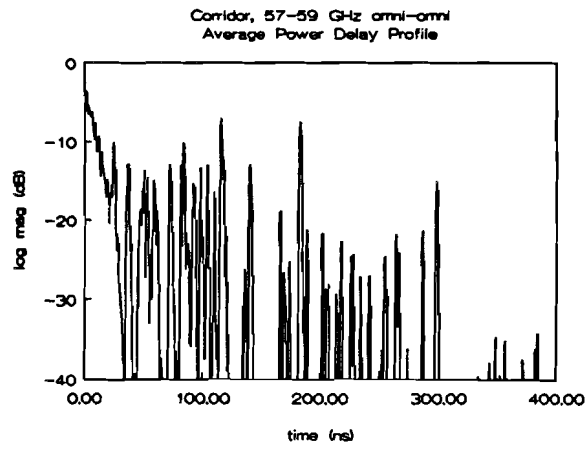

Figure K.10 : Simulation

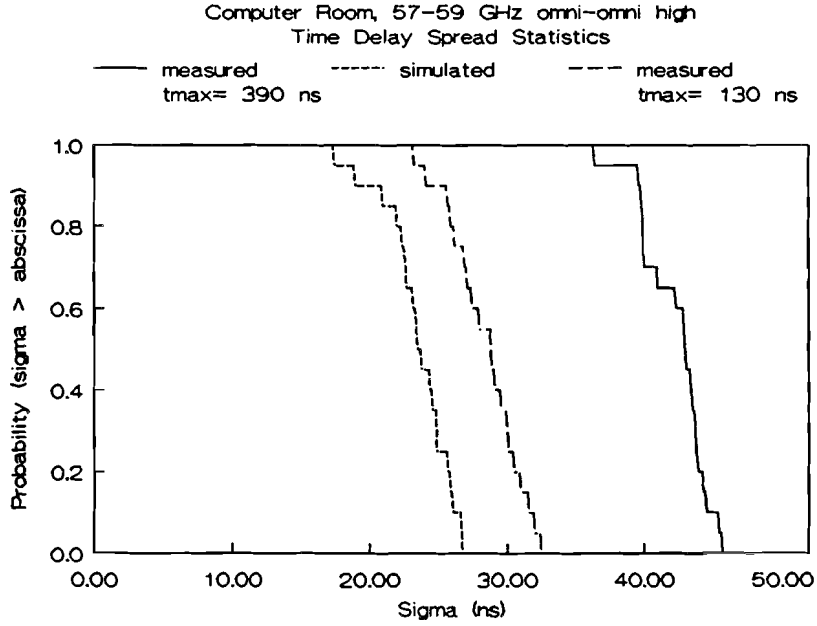

Figure K.11

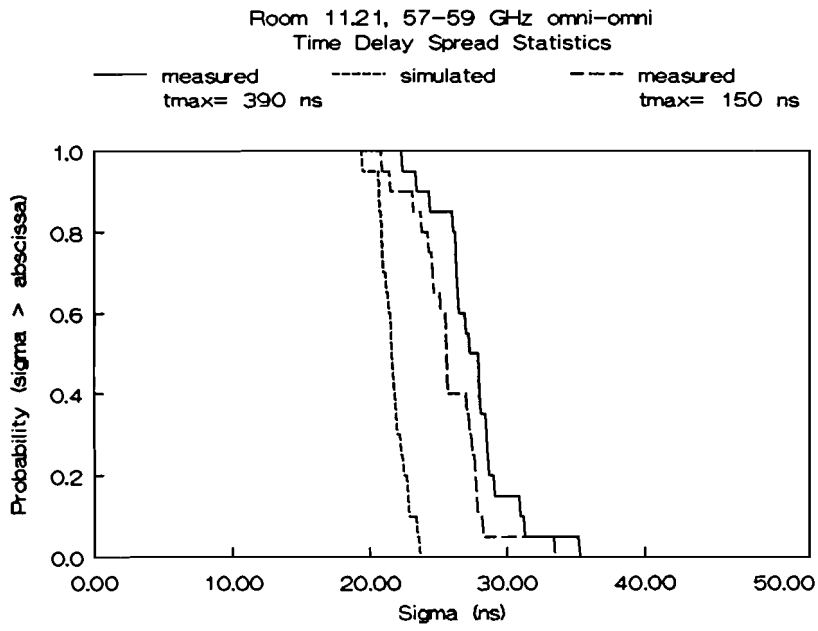

Figure K.12

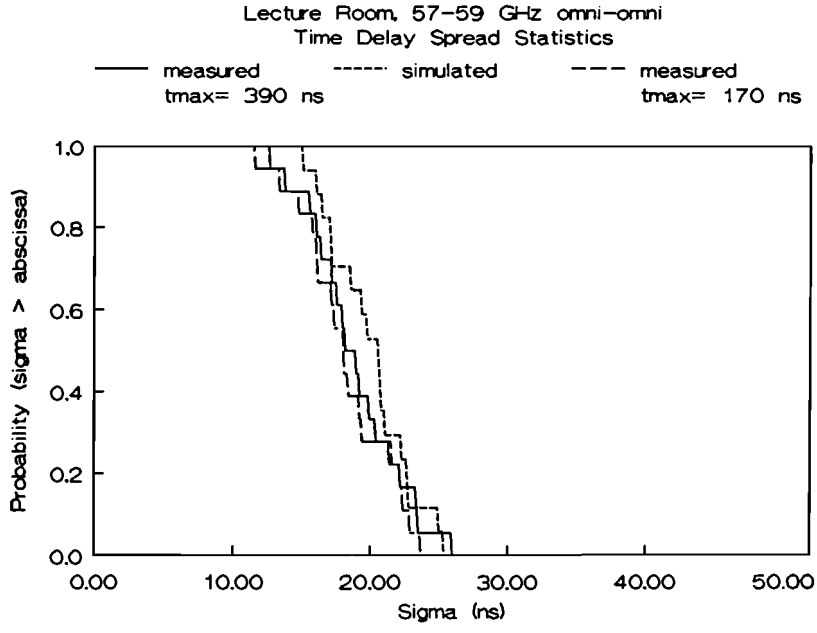

Figure K.13

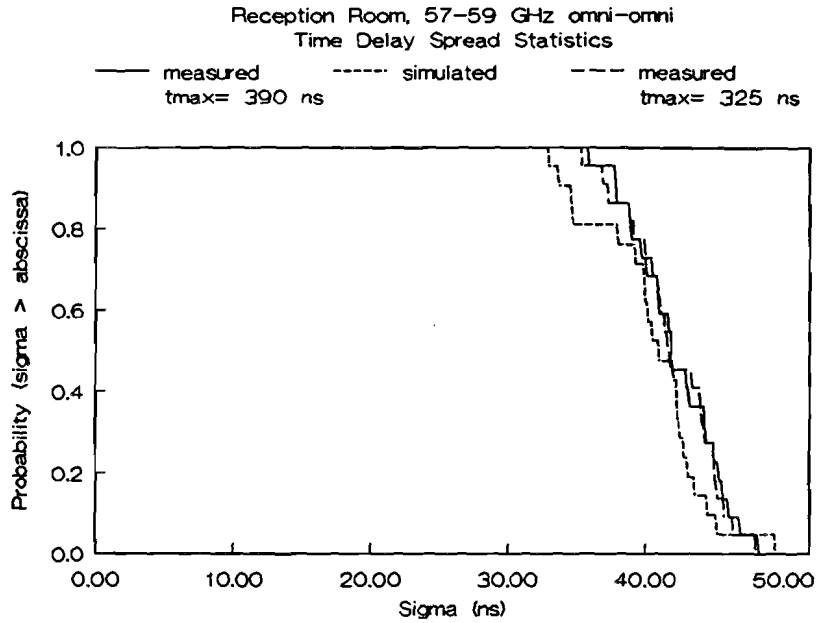

Figure K.14

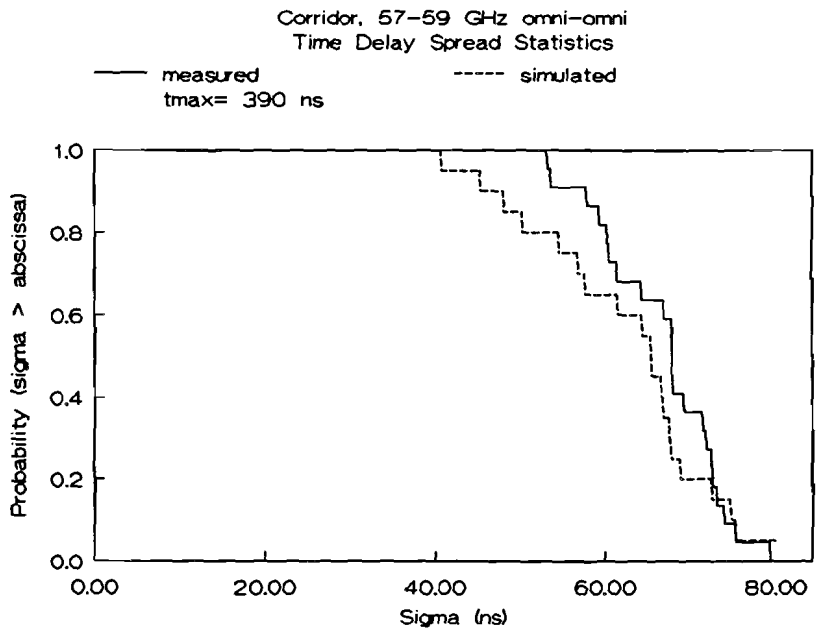

Figure K.15